

Ensemble Symmetry: Tower of States and Landscape of Information Dynamics

Olumakinde Ogunnaike,^{1,*} Rishi P. Lohar,^{2,†} and Jong Yeon Lee^{2,‡}

¹*Department of Physics, The University of California, Berkeley, CA 94618, USA*

²*Department of Physics and Institute of Condensed Matter Theory, The University of Illinois at Urbana-Champaign, Urbana, IL 61801, USA*

(Dated: February 27, 2026)

We study dynamical phases of monitored random circuits (MRCs) with a global symmetry G . In the absence of symmetry, such circuits exhibit a measurement-induced phase transition (MIPT) between area-law and volume-law entanglement in purified trajectories. Enforcing G introduces new MIPTs arising from two distinct forms of spontaneous symmetry breaking: (i) a charge-sharpening transition diagnosed by rapidly decaying charge variance and suppression of strong-to-weak spontaneous-symmetry-breaking in the steady state, and (ii) a charge-coherence transition, associated with the onset of long-lived coherence between charge sectors and glassy charge order in the steady state. We analyze these phases by mapping a G -symmetric n -replicated MRC into an effective Hamiltonian on a $2n$ -replicated Hilbert space with an enlarged, “ensemble” symmetry group \mathcal{G} . For continuous G , this finite-replica construction inherits an unphysical bias whose origin we explain before outlining how to restore the physical low-energy structure. In the resulting theory, Anderson tower-of-states gaps control the purification, charge-sharpening, and charge-decohering timescales, while the corresponding ensemble symmetry breaking determines the scaling of steady-state entanglement, charge variance, and “charge coherence.” Finally, we test these predictions in U(1)-symmetric circuits using matrix product state (MPS) variational analysis of the effective Hamiltonian and simulations of measurement dynamics.

CONTENTS

| | | | |
|---|----|---|----|
| I. Introduction | 2 | C. Order parameters in the reduced basis | 16 |
| A. Review: Monitored Random Circuits | 2 | D. Variational ansatz | 17 |
| B. Summary of Results | 4 | E. Variational phase diagram | 18 |
| C. Organization of the Paper | 6 | 1. Charge-dominated measurements | 18 |
| II. Ensemble evolution | 6 | 2. Phase-dominated measurements | 19 |
| A. Unitary dynamics | 6 | F. Charge-coherent simulation | 19 |
| B. Continuous measurements | 7 | VI. Discussion and Outlook | 20 |
| C. Ensemble evolution and Activity bias | 8 | Acknowledgments | 22 |
| III. Diagnostics of Dynamical Phases | 9 | References | 22 |
| A. n -th moment quantities | 9 | A. Decoherence effects | 24 |
| B. $n = 2$ ensemble symmetry group | 10 | B. Finite replica index, activity bias, and diffusive charges | 25 |
| IV. Relaxation and Fluctuation | 11 | C. Purification Timescale and the $\Theta(t)$ Function | 26 |
| A. Timescales and Tower of States | 11 | D. Charge Sharpening/Decohering Timescale | 27 |
| 1. Purification timescale | 11 | E. Steady-State Variance | 29 |
| 2. Charge-sharpening timescale | 12 | 1. Subsystem charge variance | 29 |
| 3. Charge-decoherence timescale | 12 | 2. Subsystem charge coherence | 30 |
| B. Fluctuations in steady states | 13 | F. n-copy Charges and Correlators | 31 |
| 1. Entanglement scaling | 13 | G. Entanglement Transition: Mean-Field and Replica Limit | 32 |
| 2. Charge Variance/Coherence scaling | 14 | H. Gutzwiller-Jastrow variational projection | 33 |
| 3. SW-SSB and glassy SSB correlators | 14 | I. Discrete G Example: \mathbb{Z}_2 Ensemble SSB | 33 |
| V. Example: U(1) Ensemble SSB | 15 | J. U(1) Ansatz Data | 35 |

* ogunnaike@berkeley.edu

† rishil2@illinois.edu

‡ jongyeon@illinois.edu

| | |
|----------------------------------|----|
| K. Explicit Phase Measurements | 36 |
| L. Measurement-Only Circuit Data | 37 |

I. INTRODUCTION

Entanglement dynamics in open quantum many-body systems emerge from the competition between unitary evolution, measurements and decoherence. The competition between unitaries and measurements can drive measurement-induced phase transitions (MIPTs) [1–10] between regimes in which frequent measurements purify an initially mixed state within $\mathcal{O}(1)$ time to an area-law-entangled trajectory and regimes in which dominant unitaries keep it volume-law entangled and effectively mixed for times exponential in system size before eventual purification. These transitions are now well established theoretically and have been observed experimentally [11, 12].

Global symmetries further enrich this picture. Local measurements of a conserved charge rapidly purify the corresponding charge distribution (“charge sharpening”) even when the state remains mixed and volume-law entangled [13–15]. Conversely, measurements insensitive to charge, preserve off-diagonal coherence between charge sectors that would otherwise rapidly dephase under arbitrarily weak decoherence. Describing these symmetry-resolved effects requires higher moments of the density matrix, i.e., an n -copy ensemble with an enlarged symmetry [16], and can produce spontaneous symmetry breaking (SSB) in the replicated Hilbert space that has no equilibrium analog in systems with the same microscopic symmetry.

Here we develop a framework that relates three ingredients: (i) SSB of the $2n$ -copy ensemble symmetry, (ii) steady-state correlation structure, and (iii) intrinsic time scales for purification, charge sharpening, and charge decoherence. We map a G -symmetric n -replicated monitored random circuit to an effective Hamiltonian on a $2n$ -replicated Hilbert space with an enlarged ensemble symmetry group G , and relate order in this replicated space to information-theoretic observables—purity, charge variance, and inter-sector coherence. The low-energy structure of the replicated model is expected to yield predictions for the time scales above as well as scaling of steady-state entanglement and charge diagnostics, including a “charge coherence,” that detects long-lived off-diagonal order between charge sectors.

A key subtlety for continuous G is that effective Hamiltonians with $n > 1$ suffer from an activity bias that reweights measurement histories with diffusing charges, obscuring the physically relevant low-energy structure. However, this bias can be removed by restricting to configurations close to the known steady state of physical charges, where they have fully relaxed to a uniform density. Within this constrained space, the expected SSB landscape of phases described in the low-energy theory is restored.

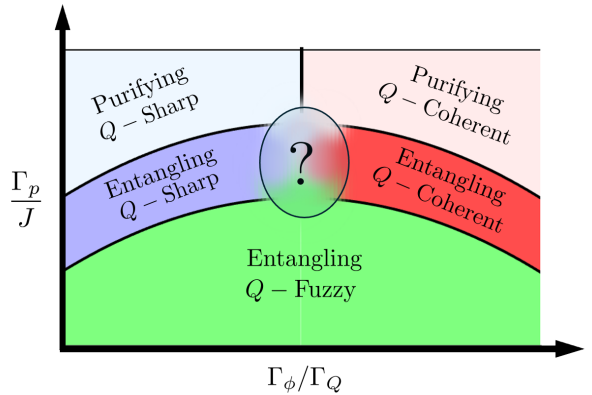


FIG. 1. **Schematic phase structure of G -symmetric MRC.** Phases are organized by the measurement strength relative to unitary dynamics (Γ_p/J) and by the relative rate of phase versus charge measurements (e.g., Γ_ϕ/Γ_Q). “Purifying” regimes purify typical mixed initial states on $\mathcal{O}(1)$ times, whereas “entangling” regimes purify only on times exponential in system size. Charge-related phases are distinguished by whether charge variance and charge coherence decay on logarithmic versus linear (in V) time scales, as summarized in Table I and discussed in the main text. The detailed structure near the central crossover region is left for future work.

The resulting picture yields a compact taxonomy of mixed-state phases of typical circuit evolutions: short- and long-range entangled phases with trivial, strong-to-weak SSB (SW-SSB) [17–23], as well as a glassy inter-replica charge order. For $U(1)$ -symmetric circuits, this glassy SSB yields a charge-coherent phase where distant spins retain random but well-defined relative phases, reflecting long-lived off-diagonal coherence stabilized by rapid “phase” measurements on neighboring sites. In symmetry-broken phases, purification, charge-sharpening, and charge-decohering time scales are set by Anderson tower-of-states (TOS) charge gaps [24–26], while the presence or absence of (quasi-)long-range order ([Q]LRO) in the inter-replica charge degrees of freedom controls the scaling of steady-state entanglement, charge variance, and charge coherence. Finally, SW-SSB and glassy SSB map naturally to Rényi-correlator diagnostics of diagonal and off-diagonal charge fluctuations.

A. Review: Monitored Random Circuits

Below, we review existing results on monitored circuits that can be described in our framework. In monitored quantum circuits, competition between unitary dynamics and local projective measurements generates distinct information-theoretic phases. A convenient route to see this involves averaging over circuit realizations and expressing disorder-averaged moments of the trajectory-conditioned density matrix as the partition function of an effective classical statistical-mechanics model. Below we briefly summarize this replica construction, first with-

out and then with global symmetries.

MIPTs. We consider ensembles of quantum *trajectories*: pure states conditioned on specific sequences of measurement outcomes and random unitaries, labeled by $\mathbf{i} := (\mathbf{m}, U)$. Entanglement transitions occur at the trajectory level but are invisible in the ensemble density matrix $\rho = \sum_{\mathbf{i}} p_{\mathbf{i}} \rho_{\mathbf{i}}$. To reveal them, one instead examines higher moments

$$\rho^{(n)} := \sum_{\mathbf{i}} p_{\mathbf{i}} \rho_{\mathbf{i}}^{\otimes n}, \quad (1)$$

which encode, for example, the trajectory-averaged Rényi entropies of a subregion A . The object $\rho^{(n)}$ lives in a doubled n -replica space $(\mathcal{H}_l \otimes \mathcal{H}_r)^{\otimes n}$ with enlarged symmetry $(\mathcal{S}_n \times \mathcal{S}_n) \rtimes \mathbb{Z}_2^{\mathbb{H}}$ [5–10], where \mathcal{S}_n permutes replicas on the ket (l) or bra (r) spaces, and $\mathbb{Z}_2^{\mathbb{H}}$ exchanges l and r by Hermitian conjugation. In the absence of physical symmetries, this replica symmetry controls the entanglement structure of typical trajectories: when \mathcal{S}_n is spontaneously broken, the typical trajectory is volume-law entangled, $S_A \sim |A|$, and purification of an initially mixed state takes a time t_{π} that is exponential in system size; when \mathcal{S}_n is unbroken, typical trajectories obey an area law, $S_A \sim |\partial A|$, and purification occurs in $\mathcal{O}(1)$ time.

Global Symmetry. When the physical Hilbert space carries an on-site symmetry group G , the ensemble symmetry is [16]

$$\mathcal{G}_n = [(G^{\otimes n} \rtimes \mathcal{S}_n)_l \times (G^{\otimes n} \rtimes \mathcal{S}_n)_r] \rtimes \mathbb{Z}_2^{\mathbb{H}}, \quad (2)$$

which we refer to as the “ n -ensemble G -symmetry,” or simply the *ensemble symmetry*. Here \mathcal{S}_n permutes the n replicas of bras or kets, $\mathbb{Z}_2^{\mathbb{H}}$ implements Hermitian conjugation by exchanging l and r with complex conjugation, and the semi-direct products encode the non-commutation of certain elements of G , \mathcal{S}_n , and $\mathbb{Z}_2^{\mathbb{H}}$.

We classify elements of \mathcal{G}_n into three types: (i) replica permutations \mathcal{S}_n ; (ii) permutation-invariant (or replica-average) transformations \bar{G} , corresponding to the same G actions on all replicas; and (iii) permutation-asymmetric (or inter-replica) transformations \tilde{G} , corresponding to replica-dependent G actions that mix charge and replica indices. Each class further decomposes under $\mathbb{Z}_2^{\mathbb{H}}$ into “diagonal” (+) sectors that are even and “off-diagonal” (−) sectors that are odd under $l \leftrightarrow r$, denoted \bar{G}_{\pm} and \tilde{G}_{\pm} . The SSB of appropriate subgroups of this ensemble symmetry organizes a landscape of dynamical phases.

\mathbb{Z}_2 -Symmetric Circuits. The landscape of ensemble SSB was first studied in Ref. [16] for discrete, \mathbb{Z}_2 -symmetric circuits with on-site Z and two-site XX unitaries and projective measurements. Here, five distinct phases were observed. The area-law (\mathcal{S}_n -symmetric) regime splits into a \mathbb{Z}_2 spin-glass phase, where XX measurements produce trajectories with spins polarized in random directions along X with definite, yet random Z -parity on each bond, and a symmetric phase, where Z

measurements produce trajectories with spins polarized in random directions along Z . These phases are distinguished by either the trajectory-averaged long-range Edwards–Anderson (EA) correlator $C_x = \text{Tr}[\rho X_0 X_x]^2$ or the parity variance $[\delta \Pi_z^2] = \text{Tr}[\rho \prod_x Z_x]$, both of which remain finite (spin glass) or vanish (symmetric). The volume-law regime (\mathcal{S}_n SSB) hosts an additional featureless phase, characterized by finite parity variance without long-range EA order.

Charge Sharpening. In a 1D $U(1)$ -symmetric monitored random circuit with local charge measurements, one finds three distinct dynamical phases separated by two critical measurement probabilities, $p_{\#}$ and p_{π} [13]. The second transition p_{π} denotes the previously mentioned MIPT between volume-law and area-law states. The first critical rate $p_{\#}$ marks the charge-sharpening transition within the volume-law phase, which is diagnosed by the relaxation of the charge variance

$$[\delta Q^2] \equiv \text{Tr}[\rho Q^2] - \text{Tr}[\rho Q]^2. \quad (3)$$

Starting from a state mixed across charge sectors, generic charge measurements drive $[\delta Q^2]$ to zero at long times in a process called charge sharpening. For low measurement probability $p < p_{\#}$ (“charge-fuzzy” phase), $[\delta Q^2]$ vanishes on a time scale linear in system size, $t_Q \sim L$; for $p > p_{\#}$ (“charge-sharp” phase), the timescale is logarithmic, $t_Q \sim \log L$.

The connection to “symmetry breaking” is best phrased in the replicated/statistical-mechanics description: Ref. [14] finds that the charge-fuzzy phase in 1D corresponds to quasi-long-range order for an inter-replica $U(1)$ symmetry [27], which is destroyed by a modified KT-like transition into the charge-sharp phase. It further emphasizes that a naive mean-field calculation at fixed replica number can yield unphysical phase-separated states at finite measurement rate, namely polarized configurations of the physical, replica-symmetric charge. In the correct replica limit ($n \rightarrow 1$), the replica-symmetric mean-field background is not affected by measurements. Accordingly, the sharpening transition arises from a non-analytic change in the inter-replica fluctuations about this uniform replica-symmetric background. Analogous results for fermionic systems have been obtained within a Keldysh formulation [15].

Learnability and SW-SSB. The charge-sharpening transition also admits a “learnability” viewpoint that was studied in decohered steady-state ensembles: in the sharp (fuzzy) phase, charge measurements identify the global charge on a timescale that is fast (slow) [28]. The relevant diagnostic is the long-distance fidelity correlator along typical trajectories,

$$\rho_x \equiv S_0^+ S_x^- \rho S_0^- S_x^+, \quad (4)$$

$$F(\rho, \rho_x) \equiv \left| \text{Tr}[\sqrt{\sqrt{\rho} \rho_x \sqrt{\rho}}] \right|^2, \quad (5)$$

where S_x^+ is a local operator carrying unit charge under G , and $x \rightarrow \infty$. This fidelity characterizes how difficult

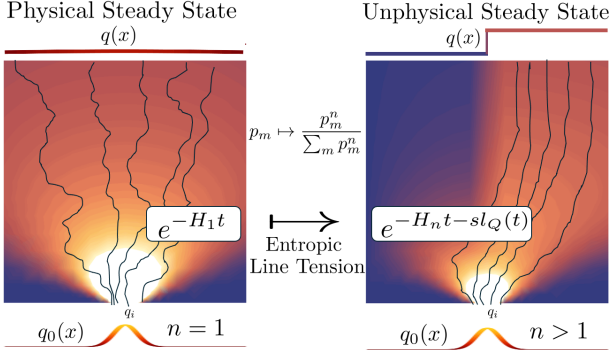


FIG. 2. Biased trajectories. Example physical-charge trajectories in the replica limit ($n \rightarrow 1$) and at finite replica index ($n > 1$). Under the physical Born rule ($n \rightarrow 1$), charges diffuse and relax to a steady state with uniform charge density. For $n > 1$, the warped Born weights $p_m \mapsto p_m^n / \sum_m p_m^n$ generate an effective line tension $e^{-s \ell_Q}$ that suppresses charge motion. This bias drives trajectories toward an unphysical, phase-separated steady state with polarized charge density.

it is to distinguish ρ from ρ_x , which is the same state with charge incoherently transported over a distance, x . Nonzero long-distance fidelity implies that one must keep track of many long-range charge correlations to distinguish states in different global charge sectors and acts as an indicator of SW-SSB [20]. In practice, we often use the Rényi-2 proxy [17],

$$\mathcal{C}^{(2)}(\rho, \rho_x) \equiv \text{Tr}[\rho \rho_x] / \text{Tr}[\rho^2], \quad (6)$$

which is easier to evaluate and coincides with the fidelity correlator for purified trajectories.

B. Summary of Results

Our work unites all of these results and proposes additional structure. We formulate a unifying principle for the phases of monitored random circuits by working with an effective Hamiltonian $\mathcal{H}^{(n)}$, obtained by applying the Choi isomorphism [29] to the generator of the higher-moment dynamics of the density matrix under G -symmetric random unitaries and measurements. Under this mapping, higher moments evolve in imaginary time with $\mathcal{H}^{(n)}$; absent unphysical biases, late-time behavior is therefore controlled by its low-energy spectrum, including finite-size splittings associated with SSB. A landscape of different symmetry breakings gives additional structure to this spectrum, generically producing multiple distinct phases (see Fig. 1). These phases are distinguished by the spontaneous breaking of replica permutations \mathcal{S}_n , diagonal replica-inter-replica \tilde{G}_+ , and off-diagonal inter-replica \tilde{G}_- ; their properties are collected in Table I.

Our central result is a correspondence between the SSB pattern of these phases in the enlarged Hilbert

space restricted to physically realistic late-time configurations (see Sec. II C) and information-theoretic observables: Rényi moments of the entanglement, charge variance, charge coherence, and Rényi correlators. Short-range order (SRO) in the ground state of the constrained replicated-space implies area-law scaling of these observables with system size, whereas [Q]LRO implies logarithmic- or volume-law scaling in the steady state. Two Rényi correlators—capturing inter-replica charge fluctuations—diagnose either SW-SSB or glassy SSB in the steady state of dynamics in the presence of decoherence. Inverse charge gaps set the relevant time scales for purification, charge sharpening, and charge decoherence [30]; in SSB phases $t_Q \sim \delta_Q^{-1}$, where δ_Q is the tower-of-states (TOS) gap. For a finite system of linear size L in D dimensions ($V = L^D$), TOS gaps are $\mathcal{O}(1)$ in symmetric phases but vanish as $V \rightarrow \infty$ in ordered phases with characteristic scaling [31, 32]. This correspondence allows us to identify the dynamical phases of symmetric monitored random circuits from the low-energy spectrum of $\mathcal{H}^{(n)}$ in a restricted Hilbert space.

For continuous G , this analysis is reliable only within the subspace of configurations with uniform physical charge density. This restriction is necessary due to an intrinsic activity bias in the replicated effective Hamiltonian: this effective Hamiltonian assigns trajectory weights p_m^n rather than p_m , suppressing trajectories with high charge fluctuations (diffusive) relative to those with low fluctuations (localized), and consequently reconfigures the steady state charge distribution. This is illustrated in Fig. 2. This bias explains the mysterious phase separation seen for $n > 1$ in Ref. [14]. Remarkably, as we show in Sec. V, we find that, within this constrained space, the qualitative SSB predictions expected of an unbiased model are restored. In contrast, as we discuss in Appendix I, there is no activity bias for discrete G , so that all low-energy states of $\mathcal{H}^{(n)}$ correspond to physically realistic late-time configurations and no explicit constraint is required. The following sections detail the corresponding signatures of ensemble SSB, focusing on the case of continuous G and assuming the aforementioned Hilbert space restriction. Table I summarizes these signatures.

Entanglement and replica-permutation SSB. Spontaneous breaking of replica-permutation symmetry \mathcal{S}_n drives the entanglement transition. In the broken phase, long-range order in the $\mathcal{H}^{(n)}$ ground state suppresses domain-wall excitations between different replica sectors: their overlap with the ground state decays as $e^{-|A|}$, where $|A|$ is the volume of a subregion A . In the symmetric phase, the ground state is short-range entangled; domain-wall excitations condense and domain wall expectations depend only on the boundary ∂A . These domain wall expectations coincide with the Rényi- n entanglement moments of the steady-state reduced density matrix on A , $\text{Tr}[\rho_A^n]$, along typical trajectories. Hence, they decay exponentially with $|A|$ in the broken phase (volume law) and with $|\partial A|$ in the symmetric phase (area

law).

The phases also differ in their purification time scales. The relevant scale is the “permutation gap,” δ_π , between the permutation-invariant ground state (unit purity) and the lowest permutation-dependent excitation: $\delta_\pi \sim e^{-V}$ in the broken phase and $\delta_\pi \sim \mathcal{O}(1)$ in the symmetric phase. Accordingly, the purification time $t_\pi \sim \delta_\pi^{-1}$ grows exponentially in the broken phase and remains $\mathcal{O}(1)$ in the symmetric phase.

Charge variance and diagonal SSB. Spontaneous breaking of the diagonal inter-replica symmetry \tilde{G}_+ controls the charge-sharpening transition. For $D = 1$, the charge measurement rate tunes between symmetric and QLRO phases. At the trajectory level, this order appears in the \tilde{G}_+ -charge variance of a subregion A , $[\delta\tilde{Q}_{+,A}^2]$, which we show in Sec. II C matches the trajectory-resolved physical charge variance, $[\delta Q_A^2]$ [14].

This QLRO regime corresponds to the “charge-fuzzy” phase reported in Refs. [13, 14]. Although explicitly demonstrated for U(1), similar physics holds for discrete G [16, 33]. In the SSB phase, classical charge information, encoded in the diagonal symmetry sectors, remains hidden for long times—exponential in system size for discrete symmetries and polynomial in system size for continuous ones [33, 34].

This order is rooted in ground-state inter-replica charge fluctuations and can be diagnosed by an Edwards–Anderson-type order parameter. When diagonal charge order is present, bras and kets exhibit paired, opposite fluctuations, yielding the Rényi-2 SW-SSB correlator

$$\mathcal{C}_x^{(+)} = \text{Tr}[S_0^+ S_x^- \rho S_0^- S_x^+] / \text{Tr}[\rho^2] + \text{h.c.}, \quad (7)$$

which signals SW-SSB in the steady state through long-range order, or QLRO in 1D through power-law scaling with exponent, η_+ . Conversely, exponentially decaying correlations diagnose short-range order in the symmetric phase.

Charge-sharpening time scales are set by the \tilde{G}_+ charge gap δ_Q . In the symmetric phase $\delta_Q \sim \mathcal{O}(1)$, but the time scale acquires a logarithmic factor from the degeneracy D_Q of \tilde{G}_+ excitations within a bandwidth of δ_Q (see Appendix D). In the SSB phase, $\delta_Q \sim V^{-1}$, but there are only a finite number of TOS excitations within this range, whereas in the symmetric phase, $\delta_Q \sim \mathcal{O}(1)$, and there are polynomially many excitations within the $\mathcal{O}(1)$ bandwidth. Accordingly, the charge sharpening time $t_Q \sim \delta_Q^{-1} \log D_Q$ grows with the system size in the broken phase and logarithmically in the symmetric phase.

Charge coherence and off-diagonal SSB. Spontaneous breaking of off-diagonal \tilde{G}_- symmetries drives a distinct transition. An initial state may have coherence among different charge sectors, but generic monitored dynamics can destroy this inter-sector coherence. In contrast, “phase” measurements can preserve these coherences, and the phase measurement rate tunes between symmetric and QLRO phases. Crucially, the

rate of coherence loss exhibits a sharp phase transition rather than varying smoothly with model parameters—a *charge-coherence* transition.

This transition corresponds to SSB of the off-diagonal inter-replica symmetry \tilde{G}_- . We quantify charge coherence by a measure on typical trajectories,

$$[\delta\Phi_Q^2] \equiv \text{Tr}(|[\rho, Q]|), \quad (8)$$

where we formally define $|[\rho, Q]| = \sqrt{[\rho, Q]^\dagger [\rho, Q]}$ with a power series expansion of the square root. In practice, we will focus on a Rényi moment of this quantity:

$$[\delta\Phi_Q^2]^{(2)} \equiv \text{Tr}([\rho, Q]^\dagger [\rho, Q]) / \text{Tr}[\rho^2], \quad (9)$$

which is identical to the \tilde{G}_- charge variances $[\delta\tilde{Q}_-^2]$ with two replicas. The product of commutators captures the sensitivity of ρ to symmetry rotations: for an infinitesimal $R(\delta\theta) = e^{iQ\delta\theta}$.

$$\text{Tr}[[\rho, Q]^\dagger [\rho, Q]] \delta\theta^2 \approx \text{Tr}[\rho^2] - \text{Tr}\left[R(\delta\theta)[\rho] R^\dagger(\delta\theta)[\rho]\right]. \quad (10)$$

This diagnoses coherence between global-charge sectors, vanishing whenever ρ is diagonal in the charge basis. This closely mirrors Rényi-2 versions of similar symmetry breaking diagnostics, such as entanglement asymmetry [35] and symmetric inseparability [36, 37]. Charge coherence can decay within a trajectory due to (i) charge sharpening or (ii) intrinsic decoherence. Charge measurements contribute to the former, while unitaries enhance the effect of the latter.

Off-diagonal charge order is diagnosed with a “glassy” SSB correlator,

$$\mathcal{C}_x^{(-)} = \text{Tr}[S_0^- S_x^+ \rho] \text{Tr}[S_0^+ S_x^- \rho] + \text{h.c.}, \quad (11)$$

whose associated ground-state charge fluctuations align between bras and kets in the steady state. This plays the role of an EA correlator calculated used to diagnose glassy phases, where the “disorder” potentials common across replicas are measurement outcomes. The coherent phase corresponds to the emergence of a steady state with frozen, random bond phases. $\mathcal{C}_x^{(+)}$ can also be used to diagnose short-range-order or QLRO with a distinct power-law exponent η_- in 1D. The \tilde{G}_- -symmetric phase is charge-incoherent (coherence lost quickly), whereas the SSB/QLRO phases are charge-coherent (coherence persists for extensive times). The corresponding charge-decoherence time t_Φ is set by the \tilde{Q}_- charge gap δ_Φ ; see Sec. IV A 3 for details.

As we explain below, the Rényi-2 SW-SSB correlator, charge coherence, and charge-decoherence timescales are only distinguishing features when the dynamics include averaging over certain unitaries before measurements, or equivalently, when one considers decoherence within trajectories. In the absence of such decoherence, unitary evolution leads to steady states of pure, volume-law

states with vanishing SW-SSB correlators in the fuzzy phase; and because unitaries do not cause decoherence within trajectories, the charge-sharpening and charge-decoherence times become identical, as do the subsystem charge variance and charge coherence. In this case, the charge-coherent phase can only be distinguished by the glassy SSB correlator, which is $C_x^{(-)} = |\langle S_0^+ S_x^- \rangle|^2$ for purified states.

C. Organization of the Paper

The rest of this paper is organized as follows. We first develop the framework for generic G -symmetric monitored random circuits and then apply it to unify previously disconnected results and predict new phases, providing numerical evidence where possible. In Sec. II, we construct the mapping between the evolution of higher moments of the density matrix, averaged over measurements and unitaries, and an imaginary-time Schrödinger dynamics in an enlarged Hilbert space governed by an effective Hamiltonian $\mathcal{H}^{(n)}$. In Sec. III, we define the higher-moment diagnostics of interest (Rényi entropies, charge variance, and charge coherence) and express them as correlation functions in the replicated Hilbert space. In Section IV, we apply this framework to explicitly demonstrate how the spectrum of the effective Hamiltonian predicts entanglement-, charge-sharpening-, and charge-cohering transitions. In Sec. V, we highlight the importance of our uniform physical charge constraint, constructing variational estimates of tower-of-states charge gaps and ground-state structure for a circuit model with global U(1) symmetry. We then present large-scale matrix-product-state simulations of discrete-time, measurement-only circuits that realize the predicted charge-coherent phase. We further use the framework to reproduce and reinterpret results for circuits with global \mathbb{Z}_2 symmetry, where no Hilbert space constraint is required (Appendix I). Finally, in Sec. VI, we provide a broader discussion and an outlook on open directions.

II. ENSEMBLE EVOLUTION

We study the evolution of ensembles of quantum states via higher moments of the density matrix. The n th moment of an ensemble $\mathcal{E} = \{(p_\psi, |\psi\rangle)\}$ of pure states is

$$\rho^{(n)} \equiv \sum_{\psi} p_\psi (|\psi\rangle\langle\psi|)^{\otimes n}. \quad (12)$$

To model monitored dynamics, we evolve $\rho^{(n)}$ under a quantum circuit composed of random unitary steps and measurements.

A. Unitary dynamics

To isolate the effect of unitary evolution, consider a Brownian random circuit with unitary

$$U_t \equiv \exp \left[-i dt \left(\sum_i h_{t,i} dB_{t,i} \right) \right], \quad (13)$$

where $dB_{t,i}$ are Brownian increments satisfying $\mathbb{E}[dB_{t,i}] = 0$ and $\mathbb{E}[dB_{t,i} dB_{t,j}] = \delta_{ij} dt$. Under this evolution, the n th moment updates as

$$\rho^{(n)}(t+dt) = \int dB p(dB) U_t^{\otimes n}(dB) \rho^{(n)}(t) [U_t^{\otimes n}(dB)]^\dagger. \quad (14)$$

In the continuous-time limit, the ensemble-averaged dynamics obey

$$\mathbb{E}[\partial_t \rho^{(n)}] = -\frac{1}{2} \sum_i \sum_{k,m} \left(h_i^{(k)} h_i^{(m)} \rho^{(n)} + \rho^{(n)} h_i^{(k)} h_i^{(m)} \right. \\ \left. - 2h_i^{(k)} \rho^{(n)} h_i^{(m)} \right), \quad (15)$$

where $h_i^{(m)} \equiv \mathbb{I}_1 \otimes \cdots \otimes \mathbb{I}_{m-1} \otimes h_i \otimes \cdots \otimes \mathbb{I}_n$ for $1 \leq m \leq n$.

We now vectorize $\rho^{(n)}$ via the Choi isomorphism [29],

$$\|\rho^{(n)}\rangle\rangle \equiv \sum_{\mathbf{i}^{(n)}} (\rho^{(n)} | \mathbf{i}^{(n)} \rangle) \otimes | \mathbf{i}^{(n)} \rangle, \quad (16)$$

where $\{|\mathbf{i}^{(n)}\rangle\} = \{|\mathbf{i}_1\rangle \otimes \cdots \otimes |\mathbf{i}_n\rangle\}$ forms an orthonormal basis for $\mathcal{H}^{\otimes n}$. In this way, the dynamics become an imaginary-time Schrödinger evolution generated by an effective Hamiltonian:

$$\mathcal{H}_{\mathcal{L}}^{(n)} \equiv \frac{1}{2} \sum_i \left(\sum_{k=1}^n [h_i^{(k)} \otimes \mathbb{I} - \mathbb{I} \otimes (h_i^{(k)})^T] \right)^2, \quad (17)$$

with $\partial_t \|\rho^{(n)}\rangle\rangle = -\mathcal{H}_{\mathcal{L}}^{(n)} \|\rho^{(n)}\rangle\rangle$. Here $(\cdot)^T$ denotes transpose in a fixed local basis, and the Choi representation realizes a $2n$ -replica description of the dynamics.

The steady states after infinitely long random-unitary evolution are unitary n -designs, labeled by permutations between system copies [7, 38]. In the presence of symmetry, these ground states of $\mathcal{H}_{\mathcal{L}}^{(n)}$ further decompose according to the commutant algebra [39]. Concretely, they are indexed by a permutation $\sigma \in \mathcal{S}_n$ and by the $2n$ left and right charge sectors $(q_l^{(1)}, q_l^{(2)}, \dots, q_l^{(n)}) = \mathbf{q}_l$, and similarly for \mathbf{q}_r [40]:

$$\|\sigma_{\mathbf{q}}\rangle\rangle = (P_{\mathbf{q}_l} \otimes P_{\mathbf{q}_r}) \sum_{\mathbf{i}^{(n)}} \bigotimes_{k=1}^n |\mathbf{i}_k\rangle \otimes |\mathbf{i}_{\sigma^{-1}(k)}\rangle, \quad (18)$$

where $\mathbf{q} = (\mathbf{q}_l, \mathbf{q}_r)$, \mathbf{i}_k denotes a basis configuration in replica k , $\mathbf{i}_{\sigma(k)}$ the corresponding configuration in replica $\sigma(k)$, and $P_{\mathbf{q}_l} = P_{q_l^{(1)}} \otimes \cdots \otimes P_{q_l^{(n)}}$ projects onto charge sectors $q_l^{(k)}$ in the left replica of each copy k . One may similarly define an effective Hamiltonian for the effects of decoherence, which explicitly breaks permutation symmetry so that only the identity permutation, $\|\mathbb{I}^{\otimes n}\rangle\rangle$, remains a ground state (see Appendix A).

| | Phase | Broken Symm. | $\text{Tr}[\rho_A^2]$ | $[\delta Q^2]_A$ | $[\delta \Phi_Q^2]_A$ | $\mathcal{C}_x^{(+)}$ | $\mathcal{C}_x^{(-)}$ | t_π^* | t_Q | t_Φ |
|-------|----------|--|--------------------------------|-------------------------|-------------------------|-----------------------|-----------------------|------------------|----------|----------|
| Mixed | Coherent | $\overline{G}_+, \tilde{G}_\pm, \mathcal{S}_2$ | | $ \partial A \log A $ | $ \partial A \log A $ | $x^{-\eta+}$ | $x^{-\eta-}$ | | V | V |
| | Fuzzy | $\overline{G}_+, \tilde{G}_+, \mathcal{S}_2$ | $e^{- A }$ | $ \partial A \log A $ | $ \partial A $ | $x^{-\eta+}$ | e^{-x} | e^V | V | $\log V$ |
| | Sharp | $\overline{G}_+, \mathcal{S}_2$ | | $ \partial A $ | $ \partial A $ | e^{-x} | e^{-x} | | $\log V$ | $\log V$ |
| Pure | Coherent | $\overline{G}_+, \tilde{G}_\pm$ | $e^{- \partial A + \log A }$ | $ \partial A \log A $ | $ \partial A \log A $ | $x^{-\eta+}$ | $x^{-\eta-}$ | $\mathcal{O}(1)$ | V | V |
| | Sharp | \overline{G}_+ | $e^{- \partial A }$ | $ \partial A $ | $ \partial A $ | e^{-x} | e^{-x} | | $\log V$ | $\log V$ |

TABLE I. **1D circuit phases and diagnostics.** Symmetry-breaking patterns and steady-state diagnostics for 1D monitored circuits. Rows distinguish *Mixed* trajectories (still highly mixed at $t \sim V = L^D$) from *Pure* trajectories (fully purified by $t \sim V$). Rows labeled *Coherent*, *Fuzzy*, and *Sharp* denote the three charge-related phases. The column “Broken Symm.” lists the spontaneously broken subgroups of the n -ensemble symmetry. The remaining columns summarize the scaling of the purity, subsystem charge variance, charge coherence, SW-SSB and SSB Rényi-2 correlators, and the characteristic timescales for purification, charge sharpening, and charge decoherence. Entries $e^{-|A|}$ and $e^{-|\partial A|}$ indicate volume- and area-law decay of $\text{Tr}[\rho_A^2]$; $\log |A|$ and ξ_\pm indicate logarithmic growth and $\mathcal{O}(1)$ saturation, respectively. Power-law scaling $\mathcal{C}_x^{(\pm)} \sim x^{-\eta\pm}$ signals 1D QLRO, whereas e^{-x} indicates exponential decay. In higher spatial dimensions $D > 1$, this algebraic order is replaced by true LRO with $\mathcal{C}_x^{(\pm)} \sim \text{Const.}$ (*) the purification time, t_π is only well-defined in the absence of intrinsic decoherence.

B. Continuous measurements

Measurements introduce dynamics distinct from unitary evolution. We consider projective measurements applied at rate Γ_p via the quantum channel

$$\rho_t \mapsto (1 - \Gamma_p \delta t) \rho_t + \Gamma_p \delta t \sum_{\mathbf{m}} \mathcal{P}_{i,\mathbf{m}} \rho_t \mathcal{P}_{i,\mathbf{m}}, \quad (19)$$

where $\mathcal{P}_{i,\mathbf{m}}$ projects onto local outcome \mathbf{m} in the measurement basis at site i . The corresponding evolution of the ensemble-averaged n th moment induces an additional contribution to the effective Hamiltonian,

$$\mathcal{H}_{\mathcal{M}}^{(n)} = \Gamma_p \sum_i \left[\mathbb{I} - \sum_{\mathbf{m}} (\mathcal{P}_{i,\mathbf{m}} \otimes \mathcal{P}_{i,\mathbf{m}})^{\otimes n} \right]. \quad (20)$$

Henceforth, when writing $\mathcal{H}_{\mathcal{M}}^{(n)}$ explicitly, we omit the additive constant shift. Although this term describes the linearized evolution of the n -copy ensemble $\|\rho^{(n)}\rangle\rangle$, it does not account for the Born weight of distinct measurement histories. As we explain in the next section, probabilistic weighting of different histories can be accomplished by a simple normalization, however this will produce a *warped* Born rule, effectively favoring some measurement trajectories over others. We consider two types of G -symmetric local measurements: *charge* and *phase*. If G is a continuous symmetry, then for $n > 1$, the competition between the term describing charge measurements and the unitary contribution introduces qualitatively incorrect results due to the different dynamics predicted for the warped and unwarped Born weights.

For charge measurements, the ground-state structure of $\mathcal{H}_{\mathcal{M}}^{(n)}$ is simple: the Hamiltonian locks the configurations of all $2n$ local copies in the charge basis. Within each charge sector, the ground-state manifold consists of

$2n$ -fold tensor products of identical local charge configurations,

$$\|\Omega_{\mathbf{i}}\rangle\rangle = \sum_{\mathbf{i}} \left(|\mathbf{i}\rangle \otimes |\mathbf{i}\rangle \right)^{\otimes n}, \quad (21)$$

where \mathbf{i} labels configurations in the local charge basis.

For phase measurements, the explicit form in the charge basis changes, but the term still induces replica locking. We define phase measurements by alternately projecting onto eigenstates of the two-site hopping operator $h_{ij} = S_i^+ S_j^- + \text{h.c.}$ and current operator, $J_{ij} = i(S_i^+ S_j^- - \text{h.c.})$ for $|i-j| = 1$, where S_i^\pm are local ladder operators. These symmetric measurements probe a kinetic contribution to the conserved charge, i.e., (the cosine and sine of) the relative phase between neighboring sites. Interestingly, such measurements of kinetic contributions have already been performed experimentally in many-body dynamical settings [41].

A combined effective Hamiltonian can be parameterized by the overall measurement rate Γ_p and a fraction of phase (versus charge) measurements $r \in [0, 1]$,

$$\mathcal{H}^{(n)} = \mathcal{H}_{\mathcal{L}}^{(n)} + \Gamma_p \left[(1 - r) \mathcal{H}_{\mathcal{M}_Q}^{(n)} + r \mathcal{H}_{\mathcal{M}_\phi}^{(n)} \right], \quad (22)$$

where $\mathcal{H}_{\mathcal{M}_Q}^{(n)}$ and $\mathcal{H}_{\mathcal{M}_\phi}^{(n)}$ are the charge and phase measurement contributions respectively. The combined dynamics are summarized in Fig. 3. $H_{\mathcal{L}}^{(n)}$ couples pairs of replicas, while $H_{\mathcal{M}}^{(n)}$ favors configurations where all $2n$ replicas coincide. Increasing the fraction of *charge* measurements suppresses inter-replica charge fluctuations, whereas increasing the fraction of *phase* measurements stabilizes inter-replica charge fluctuations.

When G is discrete, the competition between these three terms realizes all ensemble SSB phases (See Appendix I). The story is different when G is continuous:

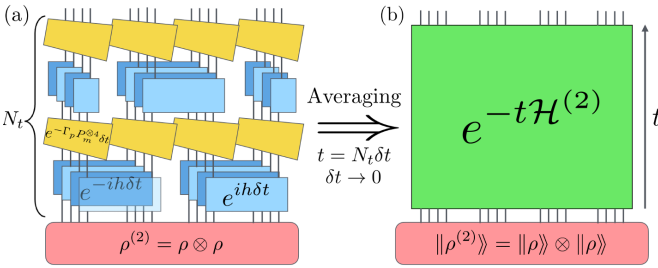


FIG. 3. Brownian circuit and effective Hamiltonian. Mapping (a) random operator dynamics with weak projective measurements to (b) imaginary-time evolution under an effective Hamiltonian $\mathcal{H}^{(2)}$ on the replicated Hilbert space. Left: an operator $\rho^{(2)} = \rho^{\otimes 2}$ evolves via a local Hamiltonian $H_{t,\mathcal{L}} \equiv \sum_i h_i dB_{i,t}$ with Brownian variables $dB_{i,t}$ shared for overlapping (dark/light) blocks and otherwise drawn independently from a Gaussian distribution, and is then acted on by weak measurements corresponding to a local term $H_{t,\mathcal{M}} \equiv -\Gamma_p \sum_{m,i} P_{m,i}^{\otimes 4}$. Right: averaging over the randomness and taking $\delta t \rightarrow 0$ produces imaginary-time Schrödinger evolution in the replicated space.

in this case $\mathcal{H}_{\mathcal{L}}^{(n)}$ hosts gapless charge excitations which are free to propagate through the system via local terms acting on 2 system copies at a time. $\mathcal{H}_{\mathcal{M}_Q}^{(n)}$, on the other hand, acts simultaneously on all $2n$ -copies, favors charge localization across replicas. Importantly, for $n = 1$, the terms are on equal footing, acting on the same 2 copies. However, for any $n > 1$, any 2-copy charge transport will frustrate the $2n$ -copy terms in $\mathcal{H}_{\mathcal{M}_Q}^{(n)}$, resulting in a finite energy penalty. The low-energy spectrum is therefore highly distorted for any finite Γ_p , rapidly eliminating charge transport and resulting in unphysical, phase-separated ground state configurations. In the next section, we provide an entropic argument in terms of measurement histories explaining the origin of this distortion for diffusive systems.

C. Ensemble evolution and Activity bias

The statistical properties of a monitored circuit are captured by appropriately weighting its quantum trajectories. A quantum trajectory consists of a collection of local G -symmetric random unitaries $\mathcal{U}_t = \prod_{\langle ij \rangle} U_{ij,t}$ and bond or site-resolved measurement outcomes $\mathbf{m}_t = \{m_{i,t}\}_t$ at each time step. We take measurements to occur independently at each bond or site and time step with probability $p = \Gamma_p \delta t$. Conditioning on these measurement outcomes yields a projection at time t ,

$$\mathcal{M}_t \equiv \prod_{m \in \mathbf{m}_t} P_m, \quad (23)$$

acting only on sites where a measurement occurs. Let $\mathbf{m} = \{m_{i,t}\}$ denote the full measurement history. Evo-

lution up to time T produces the unnormalized density matrix

$$\tilde{\rho}_{\mathbf{m}} = \mathcal{K} \rho_0 \mathcal{K}^\dagger, \quad \mathcal{K} \equiv \prod_{t=1}^T \mathcal{M}_t \mathcal{U}_t, \quad (24)$$

with Born probability $p_{\mathbf{m}} = \text{Tr}[\tilde{\rho}_{\mathbf{m}}]$ and normalized trajectory state $\rho_{\mathbf{m}} = \tilde{\rho}_{\mathbf{m}} / p_{\mathbf{m}}$.

Information-theoretic phases are distinguished by nonlinear functionals of the trajectory states $\rho_{\mathbf{m}}$, but they can be probed via observables that are linear in the n -copy trajectory ensemble

$$\rho^{(n)} \equiv \sum_{\mathbf{m}} \tilde{\rho}_{\mathbf{m}}^{\otimes n}. \quad (25)$$

For an operator $O^{(n)}$ acting on the n -replica Hilbert space, we define the trajectory- and circuit-averaged expectation value, normalized by the trace of the ensemble,

$$\overline{O^{(n)}} \equiv \frac{\overline{\text{Tr}[O^{(n)} \rho^{(n)}]}}{\overline{\text{Tr}[\rho^{(n)}]}} = \overline{\mathbb{E}_{\mathbf{m}}^{(n)} [\text{Tr}(O^{(n)} \rho_{\mathbf{m}}^{\otimes n})]}, \quad (26)$$

where $\overline{\cdot}$ denotes an average over circuit realizations and

$$\mathbb{E}_{\mathbf{m}}^{(n)} [\cdot] \equiv \sum_{\mathbf{m}} p_{\mathbf{m}}^{(n)} [\cdot], \quad p_{\mathbf{m}}^{(n)} \equiv \frac{p_{\mathbf{m}}^n}{\sum_{\mathbf{m}'} p_{\mathbf{m}'}^n} \quad (27)$$

is the average over measurement histories with a warped Born rule. Relative to the physical probabilities $p_{\mathbf{m}}$, trajectories are reweighted by a factor $p_{\mathbf{m}}^{n-1}$.

Of particular importance, our effective Hamiltonian $\mathcal{H}^{(n)}$, which governs the ensemble evolution will be affected by this bias. Because of this, one must be careful when analyzing the low-energy physics of $\mathcal{H}^{(n)}$. The ground states of each component exactly match the descriptions above, but issues arise when these terms compete. Combining $\mathcal{H}_{\mathcal{L}}^{(n)}$ and $\mathcal{H}_{\mathcal{M}_Q}^{(n)}$ at $r = 0$ yields a frustration-free Hamiltonian whose ground states are extremal charge product states in the replicated Hilbert space, e.g. $\bigotimes_i |\uparrow\rangle_i^{\otimes n}$ or $\bigotimes_i |\downarrow\rangle_i^{\otimes n}$ which exhibit no non-trivial dynamics.

Even if we fix a non-extremal total charge Q , the lowest-energy state in that sector is phase-separated: the charge profile contains a single domain wall (with open boundary conditions) with $\mathcal{O}(1)$ energy cost. Such states correspond to highly unphysical late-time charge configurations in which the physical charge is maximally polarized on either side of the domain wall (see Fig. 2). Further, within the fixed- Q sector, there is a finite gap to any state with additional domain-walls. Under the effective imaginary-time evolution generated by $\mathcal{H}^{(n)}$, these single domain-wall states are therefore reached on $\mathcal{O}(1)$ timescales.

This pathology arises from two ingredients: (i) the warped Born rule at finite replica index, $p_{\mathbf{m}} \mapsto p_{\mathbf{m}}^{(n)} \equiv \frac{p_{\mathbf{m}}^n}{\sum_{\mathbf{m}'} p_{\mathbf{m}'}^n}$, and (ii) diffusive dynamics of the conserved

(physical or replica-averaged) charge. The effect can be understood in terms of simple random-walk dynamics. At each timestep, a charge moves left or right with probability $p/2$ and remains at its site with probability $(1-p)$. Under the warped distribution $p_{\mathbf{m}}^{(n)}$, the relative probability of taking one step versus staying still is reduced for small p : $\frac{p}{1-p} \mapsto \frac{1}{2} \frac{p^2}{(1-p)^2}$. More generally, trajectories in which the charge takes an additional l steps relative to another are suppressed compared to the unwarped Born weight by an effective line tension or “activity bias” (See Appendix B),

$$e^{-s_{\text{eff}} l}, \quad s_{\text{eff}} \sim (n-1) \log \left(\frac{1-p}{p/2} \right), \quad (28)$$

so that highly active, strongly diffusive trajectories are probabilistically disfavored. As a result, the dynamics rapidly amplify trajectories that minimize diffusion and collapse onto domain-wall-like charge profiles. This behavior mirrors activity-biased diffusive systems [42, 43], in which the only visible transition occurs at a scale set by the diffusive timescale, $\Gamma_p^c \sim L^{-2}$ (See Appendix B).

To recover physical predictions, one must explicitly account for the activity bias at finite replica index. One strategy is to analyze inter-replica fluctuations around the known, *physical* charge trajectories obtained in the replica limit $n \rightarrow 1$. This is the approach of Ref. [14], which develops a field theory for replica-average and inter-replica modes around a mean-field ground state with a uniform charge density in the $n = 1$ theory. In that framework, transitions associated with inter-replica modes correspond to singular rearrangements of their structure around this uniform background at finite n . If, instead, one attempts to find the mean-field configuration directly at finite replica index, the same activity bias discussed above drives the solution toward unphysical domain-wall states [14].

Rather than constructing a replicated field theory, we build a variational description that imposes the same mean-field uniformity constraint on the replica-average charge. Concretely, we restrict to states with a uniform physical charge density so that all configurations carry the same activity weight under the warped distribution, and the bias associated with diffusive rearrangements is removed. Much as in Ref. [14], ensemble SSB transitions then manifest as rearrangements of the *inter-replica* structure within this uniform-charge sector. In Appendix G, we show that even a minimal variational ansatz reproduces the entanglement transition both for $n > 1$ and in the replica limit.

In what follows, we will implicitly consider evolution via our effective Hamiltonian to occur within the constrained space fixing uniform physical charge density. If this constraint is not applied, the ensemble SSB structure will no longer manifest in the low-energy theory.

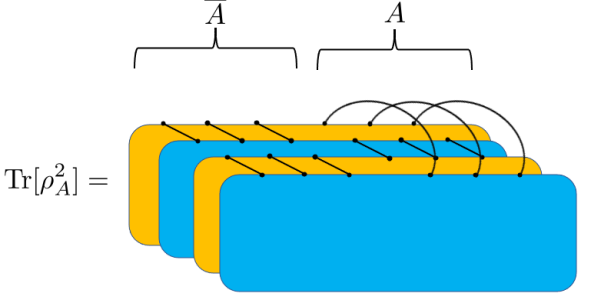


FIG. 4. Diagrammatic representation of the purity calculation from Eq. (31)

III. DIAGNOSTICS OF DYNAMICAL PHASES

A. n -th moment quantities

These ensemble SSB patterns are made particularly clear in the Choi representation. For a given replica index n , the operator expectation value in Eq.(26) can be written as an inner product with a reference state:

$$\overline{O^{(n)}}(t) = \frac{\langle\langle \mathbb{I}^{\otimes n} | O_r^{(n)} | \rho^{(n)}(t) \rangle\rangle}{\langle\langle \mathbb{I}^{\otimes n} | \rho^{(n)}(t) \rangle\rangle}, \quad (29)$$

where $O_r^{(n)} = (\mathbb{I} \otimes O)^{\otimes n}$ acts on bras in each copy, and operators acting on kets take the form $O_l^{(n)} = (O \otimes \mathbb{I})^{\otimes n}$. We will work primarily with this vectorized notation, as it provides a natural setting for the effective Hamiltonians introduced in Eq. (22).

We now define average Rényi- n entropies using the (right) cyclic permutation operator on region A ,

$$\mathcal{T}_A^{r,(n)} = \sum_{\{\alpha_i\}} \bigotimes_{i=1}^n (\mathbb{I} \otimes |\alpha_{i+1}\rangle \langle \alpha_i|), \quad (30)$$

where $|\alpha_i\rangle$ denotes a configuration on region A in replica i , and $i+1$ is understood modulo n . Thus $\mathcal{T}_A^{r,(n)}$ cyclically permutes the bra indices in A with the permutation $(1\ 2\ \dots\ n)$. Applying this permutation yields

$$\overline{[\text{Tr} \rho_A^n]} = \overline{\mathbb{E}_{\mathbf{m}}^{(n)} [\text{Tr} [\rho_{\mathbf{m},A}^n]]} = \frac{\langle\langle \mathbb{I}^{\otimes n} | \mathcal{T}_A^{r,(n)} | \rho^{(n)} \rangle\rangle}{\langle\langle \mathbb{I}^{\otimes n} | \rho^{(n)} \rangle\rangle}. \quad (31)$$

Fig. 4 shows a diagrammatic representation for $n = 2$. We then define the averaged Rényi- n entanglement entropy

$$S_A^{(n)} \equiv \frac{1}{1-n} \log \left(\overline{[\text{Tr} \rho_A^n]} \right), \quad (32)$$

which recovers the von Neumann entanglement entropy in the limit $S_A = \lim_{n \rightarrow 1} S_A^{(n)}$. In the Choi picture, the Rényi entanglement can be understood as a boundary

permutation “magnetization” at the final time slice of the evolution of $|\rho^{(n)}(t)\rangle\rangle$. In the SSB phase, this permutation magnetization penetrates into the bulk of the evolution, indicative of long-lived entangling dynamics; in the symmetric phase, it is confined near the boundary, signaling a purifying phase.

We can similarly examine the correlation structure of charged degrees of freedom. Introducing a symmetry G with conserved charge Q , we define the trajectory-averaged charge variance and n 'th moment of charge coherence of a subregion A as

$$\overline{[\delta Q_A^2]} \equiv \overline{\mathbb{E}_{\mathbf{m}}^{(n)} [\text{Tr}[\rho_{\mathbf{m}} Q_A^2] - \text{Tr}[\rho_{\mathbf{m}} Q_A]^2]}, \quad (33)$$

$$\overline{[\delta \Phi_{Q_A}^2]}^{(n)} \equiv \frac{\overline{\mathbb{E}_{\mathbf{m}}^{(n)} [\text{Tr} [|\text{ad}_{\rho_{\mathbf{m}}}^n(Q_A)|]]}}{\overline{\mathbb{E}_{\mathbf{m}}^{(n)} [\text{Tr}[\rho_{\mathbf{m}}^n]]}}, \quad (34)$$

where $\text{ad}_x(y) \equiv [x, y]$ is the adjoint action, $|\text{ad}_{\rho_{\mathbf{m}}}^n(Q_A)| \equiv |\text{ad}_{\rho_{\mathbf{m}}}^{n/2}(Q_A)|^\dagger \text{ad}_{\rho_{\mathbf{m}}}^{n/2}(Q_A)$ and Q_A is the total charge in region A . Taking the replica limit, we obtain the von-Neumann quantity, $\text{Tr} [|\langle \rho_{\mathbf{m}}, Q_A \rangle|]$, with $|\langle \rho, Q_A \rangle| \equiv \sqrt{[\rho, Q_A]^\dagger [\rho, Q_A]}$ (See Appendix F). This charge coherence can be interpreted as a kind of susceptibility of Q_A to rotation by the density matrix, ρ . In particular, the charge coherence will vanish whenever ρ is diagonal in the charge basis within a region A ($[\rho, Q_A] = 0$). As a consequence, if the charge variance of a region vanishes, the charge coherence must vanish as well.

In the Choi representation, these objects are implemented as matrix elements between appropriately chosen configurations of ensemble charges and the vectorized ensemble $\|\rho^{(n)}(t)\rangle\rangle$. In what follows, we focus on observables that can be defined with two or fewer replicas ($n \leq 2$), such as purity, charge variance, and charge coherence. Generalizations to higher moments or other permutation structures (e.g., Rényi negativities or higher moments of the charge distribution) should be straightforward within the same framework.

B. $n = 2$ ensemble symmetry group

Before defining the relevant measures of ensemble symmetry breaking, we briefly review the symmetry transformations and corresponding charges acting on the enlarged Hilbert space $(\mathcal{H}_l \otimes \mathcal{H}_r)^{\otimes n}$. For $n = 2$, the ensemble symmetry group is

$$\mathcal{G} = [(G^{\otimes 2} \rtimes \mathcal{S}_2)_l \times (G^{\otimes 2} \rtimes \mathcal{S}_2)_r] \rtimes \mathbb{Z}_2^{\mathbb{H}}. \quad (35)$$

Physically, we are interested in states that transform under replica permutations \mathcal{S}_2 , replica-average transformations, \overline{G} , and inter-replica \tilde{G} , respectively. Replica-average and inter-replica transformations encode ensemble-averaged and trajectory-resolved properties, while the Hermiticity symmetry $\mathbb{Z}_2^{\mathbb{H}}$ (bra-ket exchange) distinguishes diagonal and off-diagonal SSB[44].

We characterize these transformations by their associated symmetry charges. For continuous G , the corresponding charges are the infinitesimal generators of these transformations. For discrete symmetries, it is convenient to introduce “charges” of the form $\mathbb{I} - U_g$, where U_g is a representation of $g \in \mathcal{G}$;

The discrete \mathcal{S}_2 permutation (diagonal replica) transformations give rise to the “charge”

$$Q_\sigma = \frac{1}{2} \left(\mathbb{I}^{\otimes 4} - \frac{1}{2} (\mathcal{T}^{r,(2)} + \mathcal{T}^{l,(2)}) \right), \quad (36)$$

where Q_σ distinguishes \mathcal{S}_2 sectors, acting as a projector to the \mathcal{S}_2 -odd sector for physical $\mathbb{Z}_2^{\mathbb{H}}$ -even configurations.

The replica-average G transformations \overline{G}_\pm are generated by the charges

$$\overline{Q}_\pm = \frac{1}{2} \sum_{n=1}^2 (Q_{nl} \pm Q_{nr}), \quad (37)$$

where n labels the replica, and r (l) denotes action on bras (kets). \overline{Q}_+ is the replica-average diagonal charge and governs the spread of physical charge throughout the system. \overline{Q}_- is the replica-average off-diagonal charge and controls the ability of the ensemble-averaged state to maintain charge coherence.

Similarly, for the inter-replica G transformations \tilde{G}_\pm :

$$\tilde{Q}_\pm = \frac{1}{2} \sum_{n=1}^2 (-1)^{n-1} (Q_{nl} \pm Q_{nr}), \quad (38)$$

which define inter-replica diagonal and off-diagonal charges, respectively. \tilde{Q}_+ controls trajectory-resolved charge variance, while \tilde{Q}_- controls trajectory-resolved charge coherence.

SSB of the diagonal replica-permutation symmetry can be diagnosed by a “replica magnetization”

$$o_\sigma = \frac{1}{2} \sum_i (Q_{1l,i} Q_{1r,i} - Q_{2l,i} Q_{2r,i}), \quad (39)$$

which anticommutes with Q_σ and can be used to distinguish the two permutation sectors.

For the continuous charges, it is convenient to use order parameters that probe collective diagonal and collective inter-replica charge fluctuations rather than constructing a separate order parameter for each ensemble charge. Assuming the circuit acts on qudits of dimension $d = 2S+1$, we can write order parameters for these ensemble charges in terms of local spin- S operators in the spherical basis. We define

$$o_+ = \sum_j \sum_{n=1}^2 (S_{nl,j}^+ S_{nr,j}^+ + S_{nl,j}^- S_{nr,j}^-), \quad (40)$$

$$\tilde{o} = \sum_j \sum_{a=\{l,r\}} (S_{1a,j}^+ S_{2a,j}^- + S_{1a,j}^- S_{2a,j}^+). \quad (41)$$

Here o_+ simultaneously raises or lowers the charge on paired left and right states at each site j , while \tilde{o} raises the charge on the left in one replica and lowers it on the right for the other. Consequently, o_+ diagnoses SW-SSB (diagonal SSB), whereas \tilde{o} detects inter-replica symmetry breaking (inter-replica SSB or glassy order) of the ensemble $\rho^{(2)}$ [45].

We thus have two complementary approaches to diagnose SSB for a generic ensemble charge Q_G : (i) via the ensemble charge variance $\langle\langle(\delta Q_G)^2\rangle\rangle$, and (ii) via the variances of the order parameters, $\langle\langle(\delta o_+)^2\rangle\rangle$ and $\langle\langle(\delta \tilde{o})^2\rangle\rangle$. In SSB phases, a finite $\langle\langle(\delta o_+)^2\rangle\rangle$ signals long-range order in diagonal charge fluctuations, while a finite $\langle\langle(\delta \tilde{o})^2\rangle\rangle$ signals long-range order in inter-replica off-diagonal *and* diagonal charge fluctuations. In the presence of gapless TOS excitations, $\langle\langle(\delta Q_G)^2(t)\rangle\rangle$ remains finite at fixed late times in the thermodynamic limit ($V \rightarrow \infty$), but vanishes for a finite system as $t \rightarrow \infty$.

Finally, note that if both \mathcal{S}_2 and \tilde{G}_+ are spontaneously broken, there will be effective TOS excitations for \tilde{Q}_- charge sectors. This is because the two inter-replica charges are related by permutation symmetry:

$$\mathcal{T}^{r,(2)} \tilde{Q}_+ (\mathcal{T}^{r,(2)})^\dagger = \tilde{Q}_-. \quad (42)$$

However, this does not imply true \tilde{G}_- breaking. To distinguish these cases, we also consider the effect of infinitesimal charge decoherence—a \mathcal{S}_2 -breaking perturbation that respects \tilde{G}_- and gaps out the low-energy \tilde{Q}_- modes in the sharp and fuzzy phases.

IV. RELAXATION AND FLUCTUATION

In this section, we show how ensemble-charge variances fix universal timescales for purification, charge sharpening, and charge decoherence. Late-time circuit behavior follows from the presence or absence of SSB of the ensemble symmetry, diagnosed by TOS charge gaps in the spectrum of the effective Hamiltonian, though only when constrained to states with no physical charge diffusion. If this constraint is not applied, the purification, charge sharpening, and charge decoherence times will be predicted to be finite or $\log L$. We support the legitimacy of this constraint in Sec. V by explicitly constructing a variational ansatz for U(1)-symmetric evolution of the $n = 2$ ensemble, whose low-energy structure numerically corroborates the predictions from ensemble SSB considerations below.

A. Timescales and Tower of States

Instead of calculating variances with expectation values in the replicated Hilbert space, to draw a clean connection with circuit diagnostics, we define matrix elements between fixed boundary conditions and the imaginary-time evolution of the two-copy ensemble,

$\|\rho^{(2)}\rangle\rangle$. We employ boundary states of (i) the identity permutation $\|B\rangle\rangle = \|\mathbb{I}^{\otimes 2}\rangle\rangle$ and (ii) swap $\|B\rangle\rangle = \|SW\rangle\rangle$. These are ground states of the random-unitary contribution in Eq.(17), which are “polarized” in that they are nearly orthogonal and show \mathcal{S}_2 magnetization: $\langle\langle B|(\delta o_\sigma)^2|B\rangle\rangle \sim V^2$ for the replica magnetization, o_σ in Eq.(39).

To complete the matrix element, we need one of the global ensemble charges $Q_G \in \{Q_\sigma, \bar{Q}_\pm, \tilde{Q}_\pm\}$ defined in Sec. II C. Further, we must use the boundary state spanning multiple sectors of the appropriate Q_G . This defines the *charge-variance element*

$$[\delta Q_G^2]_B := \frac{\langle\langle B|Q_G^2|\rho^{(2)}(t)\rangle\rangle}{\langle\langle B|\rho^{(2)}(t)\rangle\rangle} - \left(\frac{\langle\langle B|Q_G|\rho^{(2)}(t)\rangle\rangle}{\langle\langle B|\rho^{(2)}(t)\rangle\rangle} \right)^2, \quad (43)$$

where the identity (swap) boundary state has the appropriate structure for \tilde{Q}_+ (\tilde{Q}_-) charge fluctuations (See Appendix D). Note that the second term vanishes for all G -charges except \bar{Q}_+ .

This form isolates the late-time impact of charge excitations. Assuming a unique symmetry-singlet ground state of $\mathcal{H}^{(2)}$, the state $\|\rho^{(2)}(t)\rangle\rangle$ relaxes into the $Q_G = 0$ sector, so $[\delta Q_G^2] \rightarrow 0$ at long times. This comes from the fact that nondegenerate ground states transform trivially under all symmetries and thus lie in the singlet sector. As a consequence, we immediately conclude that as $t \rightarrow \infty$ each trajectory $\rho_m(t)$ becomes a pure state in a definite charge sector, implying $[\delta Q_\sigma^2]_{\text{id}} = [\delta \tilde{Q}_+^2]_{\text{id}} = [\delta \tilde{Q}_-^2]_{\text{sw}} = 0$. The associated decay times are set by the Q_G -charge gaps. As shown in Fig. 5, each ensemble charge admits a simple diagrammatic evaluation of its variance element. More quantitatively, at late times, the decay of these variance elements follows a form

$$[\delta Q_G(t)]_B \underset{t \rightarrow \infty}{\approx} \frac{e^{-t\delta}}{1 + C_G e^{-t\Delta}}, \quad (44)$$

where δ is the gap between the ensemble symmetry sectors; Δ is another excitation gap, and C_G is a coefficient related to the degeneracy of excited states within a bandwidth, δ . For \mathcal{S}_2 , Δ is the excitation gap within the the \mathcal{S}_2 -even sector and, for the other symmetries, $\Delta = \delta$. The denominator is effectively constant on time scales $\sim \delta^{-1}$, which prolongs the relaxation time by a factor of $\log C_G$ if the gaps are identical. Thus the relevant relaxation time scales are

$$t_G \sim \begin{cases} \delta_0^{-1} & (\mathcal{G} = \mathcal{S}_2) \\ \delta_G^{-1} \log C_G & (\text{else}). \end{cases} \quad (45)$$

1. Purification timescale

From the circuit representation shown in Fig. 5, the Q_σ variance element with identity-permutation boundary

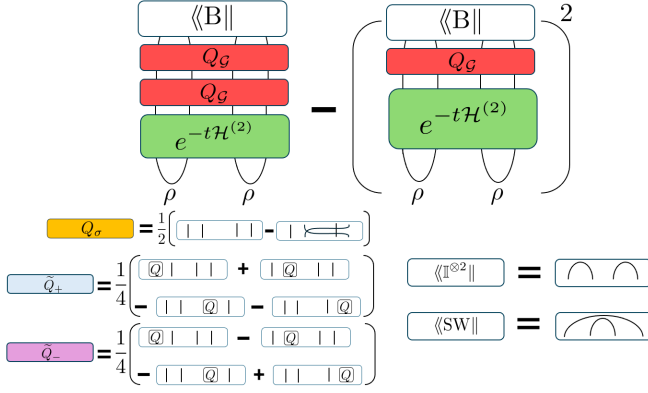


FIG. 5. **Charge variance element** $[\delta Q_G^2]_B$. Diagrammatic representation of the (unnormalized) charge variance overlap for the ensemble replica charge Q_G , with boundary states $\langle\langle B \rangle\rangle$

conditions is

$$\begin{aligned} [\delta Q_\sigma^2(t)]_{\text{id}} &= \frac{1}{4} - \frac{1}{4} \left(\overline{\mathbb{E}_m^{(2)} [\text{Tr}(\rho_m^2(t))]} \right)^2 \quad (46) \\ &\underset{t \rightarrow \infty}{\approx} \frac{e^{-t\delta_0}}{1 + C_\pi e^{-t\Delta^+}} \end{aligned}$$

so that $[\delta Q_\sigma^2] = 0$ once the trajectory-averaged purity saturates to 1. Here, δ_0 is the gap between the S_2 even and odd sectors, Δ^+ is the excitation gap within the S_2 even sector, and C_π is a coefficient related to the degeneracy of excited states in this sector (see Appendix C).

At low measurement rates, the unitary contribution dominates and the two replica magnetizations are nearly degenerate ground states, leading to symmetry breaking in the thermodynamic limit and an exponentially small TOS gap $\delta_0 \sim e^{-V}$. Accordingly, $t_\pi \sim \delta_0^{-1} \sim e^V$. By contrast, the measurement term is gapped to local S_2 -sector excitations, so at high measurement rates, $t_\pi \sim \delta_0^{-1} \sim \mathcal{O}(1)$.

This transition can also be characterized at fixed times t with $\mathcal{O}(1) \ll t \ll e^V$. For instance, taking $t \sim V$,

$$\overline{[\text{Tr} \rho^2(t)]} \underset{t \sim V}{\approx} \begin{cases} \mathcal{O}(e^{-V}) & (\Gamma_p \ll 1) \\ 1 & (\Gamma_p \gg 1) \end{cases} \quad (47)$$

Thus, at low measurement rates the purity of an initially maximally mixed state remains small, whereas at high rates the purity will have saturated.

2. Charge-sharpening timescale

We analyze the charge-sharpening transition via the long-time behavior of the \tilde{Q}_+ charge variance element.

Using Fig. 5, we see that

$$\begin{aligned} [\delta \tilde{Q}_+^2(t)]_{\text{id}} &= \frac{1}{2} \overline{\mathbb{E}_m^{(2)} [\text{Tr}(\rho_m(t)Q^2) - \text{Tr}(\rho_m(t)Q)^2]} \\ &\underset{t \rightarrow \infty}{\approx} \frac{C_Q e^{-\delta_Q t}}{1 + C_Q e^{-\delta_Q t}}, \end{aligned} \quad (48)$$

where δ_Q is the minimum \tilde{Q}_+ gap, and C_Q encodes relative degeneracies of excited and ground states (see Appendix D). Because the exponents in the numerator and denominator are the same, $[\delta \tilde{Q}_+^2]_{\text{id}}$ remains approximately constant up to

$$t_Q \sim \frac{1}{\delta_Q} \log C_Q. \quad (49)$$

In the SSB phase, the TOS yields $\delta_Q \sim V^{-1}$, and TOS excitations are not highly degenerate within a band of order δ_Q , so $C_Q = \mathcal{O}(1)$ and $t_Q \sim V$. In the symmetric phase, δ_Q is finite but there are polynomially many states within the $\mathcal{O}(1)$ bandwidth so that $C_Q \sim V^a$ and $t_Q \sim \log V$ (see Appendix D).

As in the purification analysis, a transition can be seen at finite times $t \sim V$:

$$[\delta \tilde{Q}_+^2(t)]_{\text{id}} \underset{t \sim V}{\approx} \begin{cases} 0 & (\Gamma_p \gg 1, r \sim 0) \\ \mathcal{O}(1) & (\text{else}). \end{cases} \quad (50)$$

3. Charge-decoherence timescale

Finally, we address the charge coherence transition via \tilde{Q}_- order. Using Fig. 5, we see that the inter-replica off-diagonal variance element reads

$$\begin{aligned} [\delta \tilde{Q}_-^2(t)]_{\text{sw}} &= \frac{1}{2} \frac{\overline{\mathbb{E}_m^{(2)} [\text{Tr}([\rho_m(t), Q]^\dagger [\rho_m(t), Q])]}}{\overline{\mathbb{E}_m^{(2)} [\text{Tr}(\rho_m^2(t))]}} \quad (51) \\ &\underset{t \rightarrow \infty}{\approx} \frac{C_\Phi e^{-\delta_\Phi t}}{1 + C_\Phi e^{-\delta_\Phi t}}, \end{aligned}$$

which is the 2nd moment of the trajectory-resolved charge coherence. The decoherence time is set by the off-diagonal charge gap δ_Φ and relative degeneracy C_Φ :

$$t_\Phi \sim \frac{1}{\delta_\Phi} \log C_\Phi. \quad (52)$$

An additional finite-time transition also appears at $t \sim L$:

$$\overline{[\delta \Phi_Q^2(t)]} \underset{t \sim V}{\approx} \begin{cases} \mathcal{O}(1) & (\Gamma_p \gg 1, r \sim 1) \\ 0 & (\text{else}). \end{cases} \quad (53)$$

For continuous symmetries, these finite-time transitions occur within times $\log V \lesssim t \lesssim V$ due to the sharpening and decohering timescales. This analysis yields an effective time versus measurement rate phase diagrams for purification, charge sharpening, and charge decoherence. As an example, the phases for dominant charge-and phase-measurement circuits in 1D with continuous G are shown in Fig. 6.

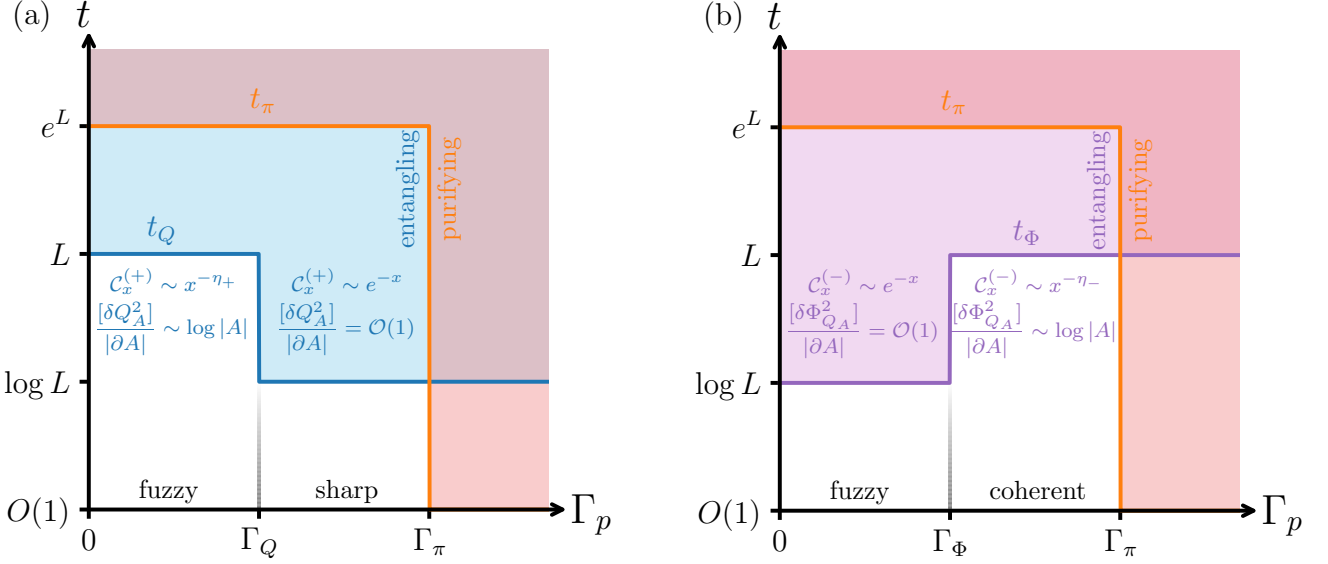


FIG. 6. 1D Dynamical phases. Time versus measurement-rate phase diagram of a U(1)-symmetric monitored 1D circuit. The shaded regions indicate where, as a function of L , the charge variances $[\delta Q_\sigma^2]$, $[\delta \tilde{Q}_+^2]_{\text{id}}$, and $[\delta \tilde{Q}_-^2]_{\text{sw}}$ vanish (orange, blue, and purple respectively). For finite L , the system always purifies at sufficiently long times. **(a)** Charge measurements only ($r = 0$): charge sharpening occurs above a critical measurement rate Γ_Q , above which the total charge can be inferred rapidly. **(b)** Phase measurements only ($r = 1$): a charge-coherent phase emerges above Γ_Φ , in which inter-replica charge coherence is maintained for times extensive in L even in the presence of decoherence.

B. Fluctuations in steady states

We now review the consequences of (Q)LRO for ensemble charges in the steady state. We will employ the variance elements as defined in Eq. (43) to consider the subsystem variance of ensemble charge quantities at long times. Specifically, we examine these quantities in a sub-region A and take $\|\rho^{(2)}\rangle\rangle \equiv \lim_{t \rightarrow \infty} \|\rho^{(2)}(t)\rangle\rangle$. We find that the scaling of the subsystem variance $[\delta Q_{\mathcal{G},A}^2]$ distinguishes phases via the presence (or absence) of charge condensation and long-range correlation functions.

1. Entanglement scaling

For \mathcal{S}_2 , the permutation charge variance over a region A , corresponds to matrix element involving a \mathcal{S}_2 domain wall:

$$\begin{aligned} [\delta Q_{\sigma,A}^2]_{\text{id}} &= \frac{1}{4} \left(1 - \left[\prod_{j \in A} \mathcal{T}_j^r \right]_{\text{id}}^2 \right) \\ &= \frac{1}{4} - \frac{1}{4} \left([\text{Tr } \rho_A^2] \right)^2 \end{aligned} \quad (54)$$

where \mathcal{T}_j^r is the local action of the \mathcal{S}_2 symmetry (see Eq. (30)). Acting with $\prod_{j \in A} \mathcal{T}_j^r$ creates a domain wall

of replica ‘‘spin flips’’ on A :

$$\prod_{j \in A} \mathcal{T}_j^r \|\mathbb{I}^{\otimes 2}\rangle\rangle = \|\text{SW}_A \otimes \mathbb{I}_{\tilde{A}}^{\otimes 2}\rangle\rangle. \quad (55)$$

Since the fundamental excitation here is a domain wall, not a charge, the condensation behavior will be flipped in the SSB and symmetric phases.

In the \mathcal{S}_2 -symmetric (area-law) phase, these domain walls condense, so the purity is boundary-controlled,

$$[\overline{\text{Tr } \rho_A^2}] \sim e^{-|\partial A|}, \quad (56)$$

up to nonuniversal $O(1)$ factors [16].

When an inter-replica symmetry \tilde{G} is broken, \tilde{Q} -charges also condense. Under the SWAP action on A , the two inter-replica charges on A are exchanged, $\tilde{Q}_{+,A} \leftrightarrow \tilde{Q}_{-,A}$, so only configurations with identical charges on A ($\tilde{Q}_{+,A} = \tilde{Q}_{-,A}$) remain in the total zero-charge sector ($\tilde{Q}_+ = \tilde{Q}_- = 0$) in the ground state $\|\rho^{(2)}\rangle\rangle$. Consequently, the purity acquires an additional combinatorial weight proportional to these configurations. In the zero charge sector, this yields

$$[\overline{\text{Tr } \rho_A^2}] \sim \frac{e^{-|\partial A|}}{|A|^{1/2}} \sim e^{-|\partial A| + \log |A|}, \quad (57)$$

again up to nonuniversal $O(1)$ prefactors.

If $\|\rho^{(2)}\rangle\langle\cdot\|$ lies in the \mathcal{S}_2 -symmetry-broken (volume-law) phase, it is a superposition of permutation-polarized states with opposite orientations, $\|\rho^{(2)}\rangle\langle\cdot\| = \|\Omega_{\text{id}}\rangle\langle\cdot\| + \|\Omega_{\text{sw}}\rangle\langle\cdot\|$, whose overlap obeys $\langle\langle\Omega_{\text{id}}|\Omega_{\text{sw}}\rangle\rangle \sim e^{-V}$ and vanishes only approximately with large system volume. The overlap of a permutation-polarized ground state with a domain wall on A then decays exponentially in $|A|$. More concretely,

$$\overline{[\text{Tr } \rho_A^2]} \sim \begin{cases} W^{-|\bar{A}|} w^{|\bar{A}|} + w^{|A|} W^{-|A|}, & (\Gamma_p \ll 1), \\ e^{-|\partial A|}, & (\Gamma_p \gg 1, r \sim 0), \\ e^{-|\partial A| + \log |A|}, & (\Gamma_p \gg 1, r \sim 1), \end{cases} \quad (58)$$

where \bar{A} has size $V - |A|$, $1 \ll |A| \ll V$, and the positive constants W, w encode polarized volume-law overlaps via $\langle\langle \mathbb{I}^{\otimes 2} \|\Omega_{\text{id}}\rangle\rangle = \langle\langle \text{SW} \|\Omega_{\text{sw}}\rangle\rangle = W^V$ and $\langle\langle \mathbb{I}^{\otimes 2} \|\Omega_{\text{sw}}\rangle\rangle = \langle\langle \text{SW} \|\Omega_{\text{id}}\rangle\rangle = w^V$.

2. Charge Variance/Coherence scaling

For the inter-replica charges, the charge variance element will correspond to the trajectory-resolved subsystem charge variance, $[\delta Q^2]_A$ or subsystem charge coherence, $[\delta \Phi_Q^2]_A^{(2)}$. These can be calculated by summing over the appropriate two-point charge correlators:

$$[\delta \tilde{Q}_{\pm, A}^2]_{\text{B}} = \sum_{ij} [c_{zz}^{(\pm)}(|i - j|)]_{\text{B}} \quad (59)$$

$$\sim \begin{cases} |\partial A|, & \text{symmetric phase,} \\ |\partial A| \log |A|, & \text{1D QLRO, SSB,} \end{cases}$$

where $[\dots]_{\text{B}}$ denotes the steady-state matrix element, $\langle\langle \text{B} \| \dots \| \rho_\infty \rangle\rangle / \langle\langle \text{B} \| \rho_\infty \rangle\rangle$, for boundary state $\| \text{B} \rangle\rangle$, and the id(swap) state is used for $\tilde{Q}_+(\tilde{Q}_-)$ -charges. This follows from the scaling of the correlators (see Appendix E):

$$[c_{zz}^{(\pm)}(x)]_{\text{B}} \sim \begin{cases} e^{-x/\xi_\pm}, & \text{symmetric phase,} \\ (x/a)^{-(D+1)}, & \text{1D QLRO, SSB,} \end{cases} \quad (60)$$

where $\xi_\pm \ll |A|^{1/d} \ll L/2$ is a finite correlation length, and the power of the algebraic decay for the 1D QLRO/SSB regime in dimension D arises from the presence of linearly dispersing goldstone modes.

As explained before, the scalings for $[\delta Q^2]_A$ and $[\delta \Phi_Q^2]_A^{(2)}$ will differ only when there is decoherence within individual trajectories, i.e., when \mathcal{S}_2 is explicitly broken

3. SW-SSB and glassy SSB correlators

We can additionally diagnose (off-)diagonal charge order via the ground-state variance of the order parameters o_+ and \tilde{o} . These can be calculated with two-point

charge-fluctuation correlators $\mathcal{C}_{ij}^{(\pm)}$:

$$[(\delta o_+)^2]_{\text{B}} = [(\delta \tilde{o})^2]_{\text{B}} = \sum_{i,j} [\mathcal{C}_{ij}^{(+)}]_{\text{B}}, \quad (61)$$

$$[(\delta \tilde{o})^2]_{\text{B}} = [(\delta \tilde{o})^2]_{\text{B}} = \sum_{i,j} [\mathcal{C}_{ij}^{(-)}]_{\text{B}}. \quad (62)$$

$\mathcal{C}_{ij}^{(\pm)}$ diagnose the presence of diagonal (+) and off-diagonal (-) charge fluctuations between sites i and j . Explicitly,

$$\mathcal{C}_{ij}^{(+)} \equiv S_{1l,i}^+ S_{1l,j}^- S_{1r,i}^+ S_{1r,j}^- + \text{h.c.} + (1 \leftrightarrow 2), \quad (63)$$

$$\mathcal{C}_{ij}^{(-)} \equiv S_{1l,i}^+ S_{1l,j}^- S_{2l,i}^- S_{2l,j}^+ + \text{h.c.} + (l \leftrightarrow r).$$

Here, $\mathcal{C}_{ij}^{(+)}$ shows (Q)LRO only with simultaneous \bar{Q}_+ and \tilde{Q}_+ fluctuations; $\mathcal{C}_{ij}^{(-)}$ shows (Q)LRO only with simultaneous \tilde{Q}_+ and \tilde{Q}_- fluctuations. Charge order within trajectories can be diagnosed with the two resulting EA-type correlators coming from these fluctuations:

$$[\mathcal{C}^{(+)}(x)]_{\text{sw}} = \frac{\mathbb{E}_{\mathbf{m}}^{(2)} [\text{Tr}(S_0^+ S_x^- \rho_{\mathbf{m}} S_0^- S_x^+ \rho_{\mathbf{m}})]}{\mathbb{E}_{\mathbf{m}}^{(2)} [\text{Tr}(\rho_{\mathbf{m}}^2)]}, \quad (64)$$

$$[\mathcal{C}^{(-)}(x)]_{\text{id}} = \frac{\mathbb{E}_{\mathbf{m}}^{(2)} [\text{Tr}(S_0^+ S_x^- \rho_{\mathbf{m}})^2]}{\mathbb{E}_{\mathbf{m}}^{(2)} [\langle\langle S_0^+ S_x^- \rangle\rangle_{\mathbf{m}}^2]},$$

where $|\text{Tr}(S_0^+ S_x^- \rho)|^2 \equiv \text{Tr}(S_0^+ S_x^- \rho) \text{Tr}(S_0^- S_x^+ \rho)$. In the absence of any \mathcal{S}_2 -breaking decoherence, these two correlators coincide in the purified steady state expression

$$\frac{\mathbb{E}_{\mathbf{m}}^{(2)} [\langle\langle S_0^+ S_x^- \rangle\rangle_{\mathbf{m}}^2]}{\mathbb{E}_{\mathbf{m}}^{(2)} [\langle\langle S_0^+ S_x^- \rangle\rangle_{\mathbf{m}}^2]}, \quad (65)$$

which is only sensitive to charge-coherent, glassy order.

The choice of boundary state is important here. Even though $\mathcal{C}^{(+)}(x)$ detects diagonal fluctuations, the polarization of the $\| \text{SW} \rangle\rangle$ boundary state implies that $[\mathcal{C}^{(+)}(x)]_{\text{sw}}$ is nonzero only when both inter-replica symmetries are broken. With a perturbative \mathcal{S}_2 -breaking decoherence term, however, $[\mathcal{C}^{(+)}(x)]_{\text{sw}}$ can remain finite while $[\mathcal{C}^{(-)}(x)]_{\text{id}}$ vanishes, signalling purely diagonal, charge-fuzzy order (see Appendix A).

When decoherence is present, the Rényi-2 correlator $[\mathcal{C}^{(+)}(x)]_{\text{sw}}$ diagnoses SW-SSB in typical trajectories $\rho_{\mathbf{m}}$, while $[\mathcal{C}^{(-)}(x)]_{\text{id}}$ diagnoses a glassy SSB order. These correlators exhibit the universal scaling

$$[\mathcal{C}^{(\pm)}(x)]_{\text{B}} \sim \begin{cases} e^{-x/\xi_\pm}, & \text{symmetric phase,} \\ (x/a)^{-\eta_\pm}, & \text{1D QLRO,} \\ \text{const.}, & \text{SSB phase,} \end{cases} \quad (66)$$

where the exponents $\eta_\pm \geq 0$ are for diagonal and off-diagonal order respectively, a is a UV cutoff of similar order to the lattice spacing, and $\xi_\pm \ll L$ are finite correlation lengths.

| Quantity | Circuit representation* | Choi representation |
|-------------------|--|--|
| Purity | $\text{Tr}[\rho_{\mathbf{m},A}^2(t)]$ | $\langle\langle \mathbb{I}^{\otimes 2} \ Q_{\sigma,A} \ \rho^{(2)}(t) \rangle\rangle$ |
| Charge variance | $\text{Tr}[\rho_{\mathbf{m}}(t)Q_A^2] - \text{Tr}[\rho_{\mathbf{m}}(t)Q_A]^2$ | $\langle\langle \mathbb{I}^{\otimes 2} \ \tilde{Q}_{+,A}^2 \ \rho^{(2)}(t) \rangle\rangle$ |
| Charge coherence | $\text{Tr}([\rho_{\mathbf{m}}(t), Q_A]^\dagger [\rho_{\mathbf{m}}(t), Q_A]) / \text{Tr}[\rho_{\mathbf{m}}^2(t)]$ | $\langle\langle \text{SW} \ \tilde{Q}_{-,A}^2 \ \rho^{(2)}(t) \rangle\rangle$ |
| SW-SSB correlator | $\text{Tr}(S_i^+ S_j^- \rho_{\mathbf{m}} S_i^- S_j^+ \rho_{\mathbf{m}}) / \text{Tr}[\rho_{\mathbf{m}}^2]$ | $\langle\langle \text{SW} \ C_{ij}^{(+)} \ \rho^{(2)} \rangle\rangle$ |
| SSB correlator | $\text{Tr}[\rho_{\mathbf{m}} S_i^+ S_j^-] \text{Tr}[\rho_{\mathbf{m}} S_i^- S_j^+]$ | $\langle\langle \mathbb{I}^{\otimes 2} \ C_{ij}^{(-)} \ \rho^{(2)} \rangle\rangle$ |

TABLE II. **Symmetry-breaking measures.** Typical-trajectory orders can be characterized either directly in the circuit representation or via matrix elements in the Choi representation. Each diagnostic exhibits universal scaling in subsystem size $|A|$ or decay time t_G , controlled by ensemble SSB. The finite-time ensemble is denoted $\|\rho^{(2)}(t)\rangle\rangle$, while the steady-state ensemble is $\|\rho^{(2)}\rangle\rangle$. Both should be considered within the constrained Hilbert space with uniform physical charge density. (*) These quantities should be interpreted as being averaged over circuit realizations as in III. Overall normalizations in the Choi matrix elements are omitted for compactness.

V. EXAMPLE: U(1) ENSEMBLE SSB

In this section, we illustrate the landscape of ensemble symmetry breaking for $G = \text{U}(1)$ in a 1D spin- $\frac{1}{2}$ chain. In what follows, we construct an effective Hamiltonian with two replicas ($n = 2$), and examine the low energy theory with our variational constraint. Afterwards, we simulate phase measurement dynamics to demonstrate the existence of the charge coherent regime. In Appendix I, we demonstrate all different ensemble SSB phases for a discrete \mathbb{Z}_2 -symmetric theory where no uniform charge constraint is required and the spectrum of the effective Hamiltonian can be evaluated directly.

For two replicas, the effective Hamiltonian splits into

$$\mathcal{H}^{(2)} = \mathcal{H}_{\mathcal{L}}^{(2)} + \Gamma_p((1-r)\mathcal{H}_{\mathcal{M}_Q}^{(2)} + r\mathcal{H}_{\mathcal{M}_\phi}^{(2)}), \quad (67)$$

representing symmetric random unitaries, charge measurements, and phase measurements, respectively. Here Γ_p is the measurement strength, and $r \in [0, 1]$ is the fraction of phase measurements. For the random unitary contribution, we take symmetric, two-site terms $h_{i,1} = \sigma_i^z \sigma_{i+1}^z$ and $h_{i,2} = \sigma_i^+ \sigma_{i+1}^- + \text{h.c.}$ as in Eq. (17). Charge measurements are implemented via Eq. (20) using onsite projectors

$$\mathcal{P}_{\pm,i}^Q = (\mathbb{I} \pm \sigma_i^z)/2. \quad (68)$$

Phase measurements project two sites onto a basis that cannot identify the total charge. Specifically, we project onto the eigenstates of the current operator $J_{i,i+1} = i(S_i^+ S_{i+1}^- - \text{h.c.})$; these are represented as

$$\begin{aligned} P_0^\phi &= \frac{1}{2}(\mathbb{I} + \sigma_i^z \sigma_{i+1}^z), \\ P_{\pm 1}^\phi &= \frac{1}{4}(\mathbb{I} - \sigma_i^z \sigma_{i+1}^z \mp (\sigma_i^x \sigma_{i+1}^x + \sigma_i^y \sigma_{i+1}^y)). \end{aligned} \quad (69)$$

Here, the outcome 0 corresponds to the absence of the current, while ± 1 to the presence of the currents with

opposite chirality. Hopping measurements will have the same eigenstates, but exchange ± 1 eigenvalues.

A. Reduced local basis

We can simplify our analysis by considering the dynamics in a subspace of fixed off-diagonal replica-average charge \bar{Q}_- . This is a natural constraint due to the existence of generic random unitary contributions of the form

$$\mathcal{H}_{\mathcal{L},z}^{(2)} = \sum_i \bar{Q}_{-,i}^2 \quad (70)$$

This kind of term will cause all sectors with finite \bar{Q}_- to decay in $\mathcal{O}(1)$ time. At the level of the random unitary circuit, this corresponds to on-site σ_i^z Brownian random rotations, which respects $\text{U}(1)$ symmetry. Such rotations rapidly dephase the off-diagonal charge sectors of the *averaged* ensemble. In contrast, there are no such terms in our effective Hamiltonian that cause the generic suppression of the other ensemble charges.

Thus, at late times, the dynamics are generically projected to the subspace with $\bar{Q}_- = 0$. This reduces the local Hilbert space dimension from $d = 16$ to $d = 6$, where it can be factorized further as a tensor product of effective spin-1 and spin- $\frac{1}{2}$ states. Explicitly we take $m \in \{-1, 0, 1\}$ and $s \in \{\uparrow, \downarrow\}$ so that

$$\begin{aligned} |1, \uparrow\rangle &= |1\rangle\langle 1| \otimes |0\rangle\langle 0|, \\ |1, \downarrow\rangle &= |0\rangle\langle 0| \otimes |1\rangle\langle 1|, \\ |0, \uparrow\rangle &= |1\rangle\langle 1| \otimes |1\rangle\langle 1|, \\ |0, \downarrow\rangle &= |0\rangle\langle 0| \otimes |0\rangle\langle 0|, \\ |-1, \uparrow\rangle &= |1\rangle\langle 0| \otimes |0\rangle\langle 1|, \\ |-1, \downarrow\rangle &= |0\rangle\langle 1| \otimes |1\rangle\langle 0|. \end{aligned} \quad (71)$$

Accordingly, the global ensemble symmetry-group is reduced to $(U(1)^{\otimes 3} \rtimes \mathcal{S}_2) \rtimes \mathbb{Z}_2^{\mathbb{H}}$ with three U(1) ensemble charges $(\bar{Q}_+, \tilde{Q}_+, \tilde{Q}_-)$ acting in the spin- $\frac{1}{2}$ sector, while the discrete symmetries act as

$$\begin{aligned}\mathcal{S}_2^r : |m, s\rangle &\mapsto |-m, s\rangle, \\ \mathbb{Z}_2^{\mathbb{H}} : |m, s\rangle &\mapsto |m, -s\rangle.\end{aligned}\quad (72)$$

Thus \mathcal{S}_2^r (right-copy permutation) flips the spin-1 label, whereas $\mathbb{Z}_2^{\mathbb{H}}$ (Hermiticity combined with a left-copy per-

mutation) flips the spin- $\frac{1}{2}$ label. Reduced-basis expressions for the ensemble charges are listed in Table III. Ising order in the spin-1 sector diagnoses \mathcal{S}_2 breaking, which, when combined with order in the spin- $\frac{1}{2}$ sector, diagnoses QLRO of the corresponding U(1) ensemble charges.

B. Hamiltonian terms and ground states

In the reduced basis, the random unitary contribution can be expressed in terms of spin-1 and spin- $\frac{1}{2}$ spin operators S_i^α and σ_i^α respectively as

$$\begin{aligned}H_{\mathcal{L}} = \sum_x 12 P_{x,x+1}^V \otimes (\sigma_x^\mu \cdot \sigma_{x+1}^\mu - 2 \sigma_x^z \sigma_{x+1}^z) - 4 \left(\text{SWAP}_{x,x+1} - \frac{1}{2} ((S_x^+)^2 (S_{x+1}^-)^2 + \text{h.c.}) \right) \otimes (\sigma_x^\mu \cdot \sigma_{x+1}^\mu) \\ + J_z (P_x^1 P_{x+1}^{-1} + P_x^{-1} P_{x+1}^1) \otimes \mathbb{I},\end{aligned}\quad (73)$$

where $J_z > 0$ is the strength of the Ising-like interaction from $h_{i,1}$, P_x^m is an onsite projector onto the spin-1 $|m\rangle$ states with $m \in \{1, 0, -1\}$, P_x^V projects nearest-neighbor spin-1 sectors to $|V\rangle = \frac{1}{\sqrt{3}}(|1, 1\rangle - |0, 0\rangle + |-1, -1\rangle)$, $\text{SWAP}_{x,x+1}$ exchanges spin-1 states at x and $x+1$, and $\sigma_x^\mu \cdot \sigma_{x+1}^\mu \equiv \mathbb{I} + \sum_{r=x,y,z} \sigma_x^r \sigma_{x+1}^r$. The $H_{\mathcal{L}}$ ground-state manifold is generated by the two permutation-polarized states obtained from the maximally mixed configuration. In the reduced basis,

$$\| \text{id} \rangle\rangle = \bigotimes_{i=1}^L (|1\rangle_i + |0\rangle_i) \otimes |+\rangle_i, \quad (74)$$

$$\| \text{sw} \rangle\rangle = \bigotimes_{i=1}^L (|-1\rangle_i + |0\rangle_i) \otimes |+\rangle_i, \quad (75)$$

with $|+\rangle \equiv (|\uparrow\rangle + |\downarrow\rangle)/\sqrt{2}$. These are magnetized in the spin-1 sector and polarized in the spin- $\frac{1}{2}$ sector, exhibiting order for \mathcal{S}_2 and \tilde{G}_\pm .

In the reduced basis, charge measurements act only on the spin-1 sector:

$$H_{\mathcal{M}_Q} = \sum_x (S_x^z)^2 \otimes \mathbb{I}_2. \quad (76)$$

This results in a ground-state manifold that excludes all $|\pm 1\rangle$ configurations, e.g. $\| \Omega_{\mathcal{M}_Q} \rangle\rangle = \bigotimes_{i=1}^L \sum_{m_i \in \{\uparrow, \downarrow\}} |0, m_i\rangle_i$, which has no magnetization in the spin-1 sector, and only displays \bar{G}_+ order. Likewise, the phase measurement contribution is

$$\begin{aligned}H_{\mathcal{M}_\phi} = \frac{1}{2} \sum_{i,m} P_i^m P_{i+1}^m \otimes (\mathbb{I}_4 + \sigma_i^z \sigma_{i+1}^z) \\ + \frac{3}{16} \sum_i P_i^{ss} \otimes (\sigma_i^\mu \sigma_{i+1}^\mu - 2 \sigma_i^z \sigma_{i+1}^z),\end{aligned}\quad (77)$$

where $P_i^{ss} = |ss\rangle\langle ss|$ projects onto matching nearest-neighbor spin-1 sectors with $|ss\rangle = |1, 1\rangle + |0, 0\rangle + |-1, -1\rangle$. A representative antiferromagnetic ground state is

$$\| \Omega_{\mathcal{M}_\phi} \rangle\rangle = \bigotimes_{i=1}^L (|1\rangle_i \otimes (\sigma_i^x) |\uparrow\rangle_i + (-1)^i |-1\rangle_i \otimes (\sigma_i^x) |\downarrow\rangle_i), \quad (78)$$

with symmetry-related partners obtained by $\prod_i \mathcal{T}^r$ (exchanging $|1\rangle \leftrightarrow |-1\rangle$) or $\prod_i (\mathbb{I} \otimes \sigma^x)_i$ (flipping $|\uparrow\rangle \leftrightarrow |\downarrow\rangle$). These states show order for \bar{G}_+ , \mathcal{S}_2 , and $\mathbb{Z}_2^{\mathbb{H}}$, while preserving the \tilde{G}_\pm symmetries. As we discuss at the end of this section, this suggests that there is a regime where phase measurements may actually destroy \tilde{G}_\pm order. In combination with $H_{\mathcal{L}}$ and $H_{\mathcal{M}_Q}$ these phase measurements generate the charge-fuzzy and charge-coherent phases discussed below.

To illustrate the true SSB characteristic of these phases, we also consider a perturbative decoherence interaction, which breaks \mathcal{S}_2 but preserves the U(1) symmetries. This will act as an identity permutaton magnetization, suppressing all $\| \text{sw} \rangle\rangle$ polarizations with $|-1\rangle$ states (See Appendix A). In the fuzzy phase, the remaining polarization in the ground state will resemble, $\| \text{id} \rangle\rangle$, and with no $|-1\rangle$ states, it will only show \tilde{Q}_+ order; while the remaining polarization in the coherent phase ground state, will include both $|\pm 1\rangle$ states, and be capable of showing order for both \tilde{Q}_\pm .

C. Order parameters in the reduced basis

To diagnose ordering, we define the order parameters from Sec. III in our reduced basis using site-resolved operators acting on the spin-1 and spin- $\frac{1}{2}$ sectors.

| \tilde{Q}_+ | \tilde{Q}_- | \overline{Q}_+ | \overline{Q}_- | Q_σ | $Q_{\mathbb{H}}$ |
|-----------------------------------|--------------------------------------|-----------------------------------|------------------|---|---|
| $\sum_i (P^1 \otimes \sigma^z)_i$ | $\sum_i (P^{-1} \otimes \sigma^z)_i$ | $\sum_i (P^0 \otimes \sigma^z)_i$ | 0 | $\frac{1}{2}(\mathbb{I} - \prod_i \mathcal{T}_i)$ | $\frac{1}{2}(\mathbb{I} - \prod_i (\mathbb{I}_3 \otimes \sigma^x)_i)$ |

TABLE III. **Reduced-basis charges.** Representation of ensemble symmetry charges in the basis obtained after fixing $\overline{Q}_- = 0$. The local Hilbert space factorizes into a spin-1 and a spin-1/2 sector. The three remaining U(1) charges live in different components of the spin-1 space; \mathcal{S}_2 acts as spin flips in the spin-1 sector, while $\mathbb{Z}_2^{\mathbb{H}}$ (Hermiticity plus left permutations) acts as spin flips in the spin-1/2 sector.

Permutation order is probed by the replica magnetization from Eq. (39), which becomes

$$M_z \equiv \frac{1}{L} \sum_i S_i^z \otimes \mathbb{I}. \quad (79)$$

Diagonal (charge-fuzzy) order involving $\overline{Q}_+ + \tilde{Q}_+$ is captured by the SW-SSB Rényi-2 correlator defined in Eq. (63). In this basis $\mathcal{C}_{ij}^{(+)} = O_i^{(+)}(O_j^{(+)})^\dagger$ where

$$O_i^{(+)} = \frac{1}{2}(S_i^x + \{S_i^x, S_i^z\}) \otimes \sigma_i^+ + \text{h.c.} \quad (80)$$

Here the spin-1 factor locally exchanges $|0\rangle \leftrightarrow |1\rangle$, indicating the $\overline{Q}_+ \leftrightarrow \tilde{Q}_+$ exchange.

Similarly, full inter-replica (charge-coherent) order involving $\tilde{Q}_+ + \tilde{Q}_-$ is captured by the related glassy SSB correlator, $\mathcal{C}_{ij}^{(-)} = O_i^{(-)}(O_j^{(-)})^\dagger$ where

$$O_i^{(-)} = \frac{1}{2}((S_i^+)^2 + (S_i^-)^2) \otimes \sigma_i^+ + \text{h.c.} \quad (81)$$

whose spin-1 factor exchanges $|1\rangle \leftrightarrow |-1\rangle$, indicating the $\tilde{Q}_+ \leftrightarrow \tilde{Q}_-$ exchange. We can also define the charge cor-

relators for \tilde{Q}_\pm :

$$c_{zz,ij}^{(\pm)} = P_i^{\pm 1} P_j^{\pm 1} \otimes \sigma_i^z \sigma_j^z. \quad (82)$$

These operators distinguish the ensemble SSB phases via the scaling of $[M_z^2]_{\text{id}}$, which signals the entanglement transition, and $[\mathcal{C}^{(\pm)}(x)]_B$ and $[c_{zz}^{(\pm)}(x)]_B$, which signal the charge sharpening (+) and charge coherence (-) transitions

D. Variational ansatz

Guided by the ground state structures discussed above, we construct a variational ansatz in the reduced basis and numerically optimize over its parameters using matrix-product-state (MPS) techniques [46]. We begin with a symmetric mean-field (MF) description of the spin-1 sector that is related to \mathcal{S}_2 , ensuring that it can interpolate between ground state configurations above. Additionally, we impose the required uniform physical charge constraint by taking the spin- $\frac{1}{2}$ degrees of freedom to be uniformly polarized. The MF state reads

$$\begin{aligned} \|\rho_{\text{MF}}^{\otimes 2}(\alpha, \beta)\rangle\rangle &= \bigotimes_{i=1}^L \left(\cos \alpha |0\rangle_i |\theta_0, \phi_0\rangle_i + \sin \alpha \cos \beta |1\rangle_i |\theta_1, \phi_1\rangle_i + (-1)^i \sin \alpha \sin \beta |-1\rangle_i |\theta_{-1}, \phi_{-1}\rangle_i \right) \\ &+ \bigotimes_{i=1}^L \left(\cos \alpha |0\rangle_i |\theta_0, \phi_0\rangle_i + \sin \alpha \cos \beta |-1\rangle_i |\theta_1, \phi_1\rangle_i + (-1)^i \sin \alpha \sin \beta |1\rangle_i |\theta_{-1}, \phi_{-1}\rangle_i \right), \end{aligned} \quad (83)$$

with $|\theta, \phi\rangle = \cos(\theta/2)|\uparrow\rangle + \sin(\theta/2)e^{i\phi}|\downarrow\rangle$. This state is the symmetric sum of two Ising polarizations. It is \mathcal{S}_2 -symmetric for $\alpha = 0$ or $\beta = \pi/4$; otherwise \mathcal{S}_2 is spontaneously broken and there will be an exponentially small gap to the \mathcal{S}_2 -odd superposition of the two polarizations.

Inter-replica charge ordering depends on the spin- $\frac{1}{2}$ space. Roughly, fixed phases $\phi_{\pm 1,i} \approx \text{const}$ signal broken $\tilde{G}(1)_\pm$, and $\beta > 0$ ensures simultaneous \tilde{Q}_\pm order as sensed by $\mathcal{C}_{ij}^{(-)}$. To capture the short-range disordered configurations and QLRO configurations, we augment the ansatz with a Gutzwiller-Jastrow term that penalizes like-signed neighboring inter-replica charges and can

generate long-range correlations for inter-replica charges in 1D (See Appendix H):

$$P_{GW,i}(g(r)) = \prod_{r=1}^{L-i} \left[\mathbb{I} - \tanh(g(r))(S_i^z S_{i+r}^z)^2 \otimes \sigma_i^z \sigma_{i+r}^z \right],$$

where we have short- and long-range contributions

$$g(r) = \begin{cases} g_1, & r = 1, \\ g_r/r^2, & r \geq 2. \end{cases}$$

For $g_1 > g_r \approx 0$, typical inter-replica charge configurations alternate sign, suppressing \tilde{Q} order; for $g_r \gtrsim g_1 > 0$,

long-range algebraic \tilde{Q} correlations emerge. The full Gutzwiller-weighted ansatz and its variational energy are

$$\begin{aligned} \|\rho_{\text{GW}}^{\otimes 2}(\alpha, \beta, g(r))\| &= \prod_i P_{\text{GW},i}(g(r)) \|\rho_{\text{MF}}^{\otimes 2}(\alpha, \beta)\|, \\ E(\alpha, \beta, g(r)) &= \frac{\langle\langle \rho_{\text{GW}}^{\otimes 2} | \mathcal{H}^{(2)} | \rho_{\text{GW}}^{\otimes 2} \rangle\rangle}{\langle\langle \rho_{\text{GW}}^{\otimes 2} | \rho_{\text{GW}}^{\otimes 2} \rangle\rangle}. \end{aligned} \quad (84)$$

We variationally minimize E at fixed (Γ_p, r) subject to a fixed uniform physical charge (see Appendix G and H). Although this variational ansatz describes the structure within different phases effectively, it will be ill-suited to identifying the exact location of transitions or their critical properties. Thus, we only focus on the structure within each of the unique phases.

E. Variational phase diagram

The variational energy $E(\alpha, \beta, g_r)$ can be unwieldy to handle analytically, however, numerical minimization reveals sharp changes in the optimal parameters (α, β, g_r) that delineate the phases summarized in Fig. 7. Because the reduced basis used here is defined by rapid z rotations, the effective dynamics cannot purify to states with well-defined local currents. Therefore, our ansatz does not realize a *purifying* charge-coherent phase; instead, it captures the other four phases distinguished by ensemble symmetry breaking and entanglement structure shown in Fig. 7.

1. Charge-dominated measurements

When charge measurements dominate ($r \sim 0$), we recover the standard charge-sharpening hierarchy. At low measurement rate, the system is in the volume-law, charge-fuzzy phase. Here \mathcal{S}_2 is broken (with finite α and $[M_z^2]_{\text{id}} > 0$), producing Ising order in the spin-1 sector, and \tilde{G}_+ is broken (with $g_r \gtrsim g_1$), so the Gutzwiller projector generates long-range correlations of inter-replica charges. In this regime,

$$[\mathcal{C}^\pm(x)]_{\text{B}} \sim (x/a)^{-\eta_\pm}, \quad [c_{zz}^{(\pm)}(x)]_{\text{B}} \sim (x/a)^{-2}, \quad (85)$$

signaling QLRO. The \mathcal{S}_2 even and odd superpositions of the two Ising polarizations are split by an exponentially small tower-of-states (TOS) gap, $\delta_0 \sim e^{-L}$, leading to an exponentially large purification time, $t_\pi \sim e^L$.

The pattern of inter-replica order requires some care. One of the variational polarizations in this phase carries apparent \tilde{Q}_- order, but as discussed in the ground-state analysis, a weak dephasing that polarizes into the $|1\rangle$ sector removes this. In the physically relevant polarized sector, only $[\mathcal{C}^{(+)}(x)]_{\text{id}}$ remains long-ranged. The lowest \tilde{Q}_+ excitations display a TOS gap $\delta_Q \sim 1/L$, leading to an extensive charge sharpening time, $t_Q \sim L$. Similarly, excitations to finite \tilde{Q}_- in the polarized sector are gapped

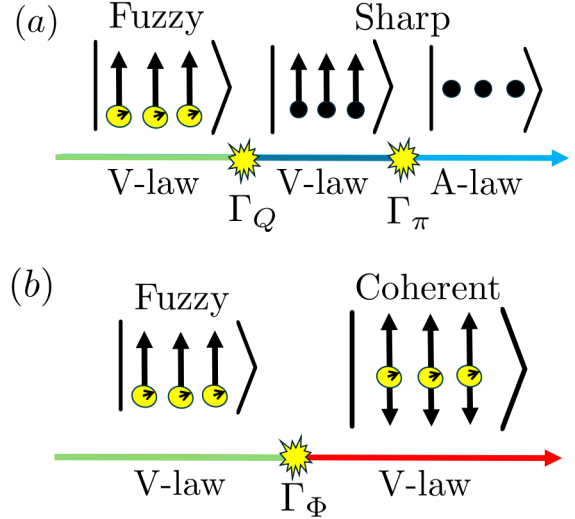


FIG. 7. Variational phase transitions. Schematic ensemble-SSB phase diagram and transitions visible using the variational ansatz. (a) When charge measurements dominate, $r \sim 0$, increasing the measurement rate drives a sequence volume-law charge-fuzzy (green) \rightarrow volume-law charge-sharp (blue) \rightarrow area-law charge-sharp (light blue). (b) When phase measurements dominate, $r \sim 1$, increasing the measurement rate drives a transition from the volume-law charge-fuzzy phase (green) to a volume-law charge-coherent phase (red). The volume-law fuzzy phase breaks \mathcal{S}_2 and \tilde{G}_+ (finite α and $g_r > g_1$). The volume-law sharp phase restores \tilde{G}_+ (with $g_1 > g_r \approx 0$). The area-law sharp phase further restores \mathcal{S}_2 (vanishing α). The volume-law coherent phase additionally breaks \tilde{G}_- (finite β), corresponding to unequal polarizations coupled to the rotors.

by $\delta_\Phi \sim \Gamma_p$, and the degeneracy within an $\mathcal{O}(\delta_Q)$ window grows as $\mathcal{O}(L)$, giving $t_\Phi \sim \log L$.

Increasing the measurement rate drives a charge-sharpening transition into the volume-law, charge-sharp phase. In this regime \mathcal{S}_2 remains broken (with finite α and Ising order), but \tilde{G}_+ is restored, reflected in $g_1 \gtrsim g_r \approx 0$ and exponentially decaying inter-replica correlations:

$$[\mathcal{C}^\pm(x)]_{\text{B}} \sim e^{-x/\xi_\pm}, \quad [c_{zz}^{(\pm)}(x)]_{\text{B}} \sim e^{-x/\xi_\pm}. \quad (86)$$

The TOS splitting between \mathcal{S}_2 sectors remains $\delta_0 \sim e^{-L}$, so $t_\pi \sim e^L$ persists. Charge excitations to $\tilde{Q}_\pm = \pm 2$ are gapped by $\delta_Q \sim \delta_\Phi \sim \Gamma_p$, and the number of quasi-degenerate low-lying states remains polynomial in L , giving charge-sharpening and decoherence times that grow logarithmically, $t_Q \sim t_\Phi \sim \log L$.

Upon further increasing the measurement rate, the system undergoes an entanglement transition into the area-law, charge-sharp phase. Here, \mathcal{S}_2 is restored ($\alpha = 0$), the spin-1 sector carries no weight on $|\pm 1\rangle$, and there is no \tilde{Q}_\pm order:

$$[\mathcal{C}^\pm(x)]_{\text{B}} = 0, \quad [c_{zz}^{(\pm)}(x)]_{\text{B}} = 0. \quad (87)$$

The lowest inter-replica excitation now necessarily creates a pair of opposite \tilde{Q}_\pm charges, so that $\delta_0 \sim \delta_Q \sim \delta_\Phi \sim \Gamma_p$, and the characteristic timescales are $t_\pi \sim \mathcal{O}(1)$ and $t_Q \sim t_\Phi \sim \log L$.

2. Phase-dominated measurements

When phase measurements dominate ($r \sim 1$), the phase structure shows qualitative changes. At low measurement rates the system again resides in the volume-law, charge-fuzzy phase with the same symmetry-breaking pattern as above.

At sufficiently large measurement rate, the system enters a volume-law, charge-coherent regime. Here \tilde{G}_- is broken (with finite β), and the spin-1 sector forms Ising order built from superpositions of both $|1\rangle$ and $| -1\rangle$ in each polarization. QLRO is enforced by $g_r \gtrsim g_1$, yielding simultaneous \tilde{Q}_\pm order:

$$[\mathcal{C}^\pm(x)]_B \sim (x/a)^{-\eta_\pm}, \quad [c_{zz}^{(\pm)}(x)]_B \sim (x/a)^{-2}. \quad (88)$$

The \mathcal{S}_2 TOS splitting remains $\delta_0 \sim e^{-L}$ and the lowest \tilde{Q}_\pm excitations display a TOS gap $\delta_Q \sim \delta_\Phi \sim 1/L$, leading to extensive charge sharpening and charge decohering times, $t_Q \sim t_\Phi \sim L$.

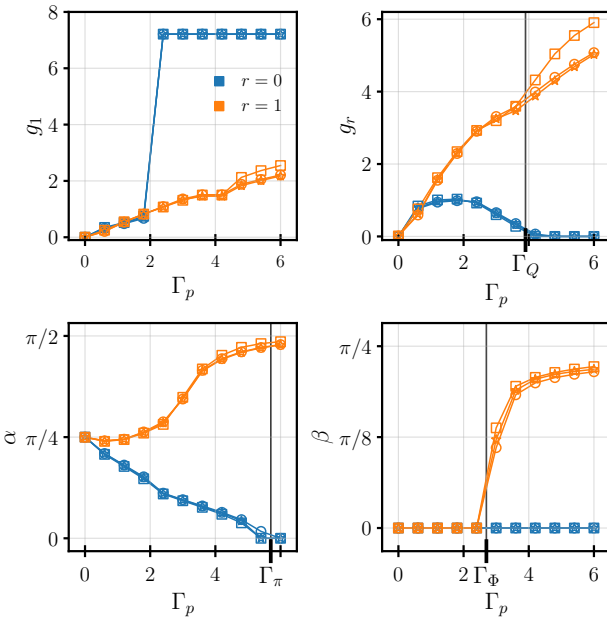


FIG. 8. U(1) ansatz parameters. Optimized ansatz parameters g_1 , g_r , α , and β from Eq. (84) for charge-only measurements ($r = 0$, blue) and phase-only measurements ($r = 1$, orange), for system sizes $L = 8, 10, 12$ (squares, stars, and circles, respectively). The weak L -dependence suggests that the variational phase structure is robust in the thermodynamic limit. Estimated critical values of Γ_p for the charge-sharpening, charge-coherent, and purification transitions are indicated on the x -axis: $\{\Gamma_Q, \Gamma_\Phi, \Gamma_\pi\} \approx \{3.9, 2.7, 5.7\}$.

Figure 8 shows the optimized parameters (α, β, g_1, g_r) versus Γ_p at $r = 0$ (charge-only) and $r = 1$ (phase-only); these are approximately L -independent (see Appendix J). The associated decay of $\mathcal{C}^{(\pm)}(x)$ and $c_{zz}^{(\pm)}(x)$ correlators across phases is illustrated in Fig. 9.

F. Charge-coherent simulation

Finally, we corroborate the existence and properties of the remaining charge-coherent, purifying phase using phase-measurement-only dynamics of MPS states. There are two main challenges to realizing charge coherence in this setting. First, measurements of the hopping operator $h_{ij} = S_i^+ S_j^- + S_i^- S_j^+$ on adjacent bonds do not commute, so overlapping measurements inject additional noise into any prospective steady state. Second, for finite on-site spin S there is no exact local phase state $|\phi\rangle$ and hence no perfectly well-defined bond phase, so that the bond “phase” is encoded in the noncommuting pair

$$\begin{aligned} h_{ij} &= S_i^+ S_j^- + S_i^- S_j^+, \\ J_{ij} &= i(S_i^+ S_j^- - S_i^- S_j^+), \end{aligned} \quad (89)$$

which characterize the real and imaginary parts of a complex bond phase. Alternating measurements of these bond operators, or more generally, quadratures, $h_{ij}(\phi) = S_i^+ S_j^- e^{-i\phi} + S_i^- S_j^+ e^{i\phi}$, effectively locks the relative phase on bonds. The commutators of $h_{ij}(\phi)$ on neighboring bonds, and of different quadratures $h_{ij}(\phi_1)$ and $h_{ij}(\phi_2)$ on the same bond quantify the amount of noise introduced by these measurements and are suppressed as S increases or $\Delta\phi = \phi_1 - \phi_2$ decreases. Because of this, as $S \rightarrow \infty$ and ϕ becomes a continuous parameter, these measurements act like mutually commuting projectors, and induce a steady state of random, well-defined phase configurations on each bond.

For finite S , we mitigate these issues by defining a single measure of the *relative* phase via a discrete Fourier transform simultaneously taken over all charge sectors. This yields a set of non-orthogonal POVMs $P(\phi)$ for N_ϕ evenly spaced values of the azimuthal phase (see Appendix K). We apply these as Krauss operators on bonds (i, j) in a brickwork pattern to evolve an initial product state,

$$|\psi_m(T)\rangle = \prod_{n=0}^{N-1} \prod_{\langle ij \rangle} P(\phi_{ij}(n\Delta t)) |\psi_0\rangle, \quad (90)$$

with $T = N\Delta t$. Each $P(\phi_{ij})$ collapses the bond (i, j) toward a state with approximate relative phase ϕ_{ij} at time $t = n\Delta t$. In the $S, N_\phi \rightarrow \infty$ limit these POVMs become orthogonal projectors onto phase eigenstates, so that the circuit would rapidly collapse an initial product state into a “phase glass” of randomly arranged, but locally well-defined, bond phases. In one dimension this state exhibits power-law Edwards–Anderson correlations

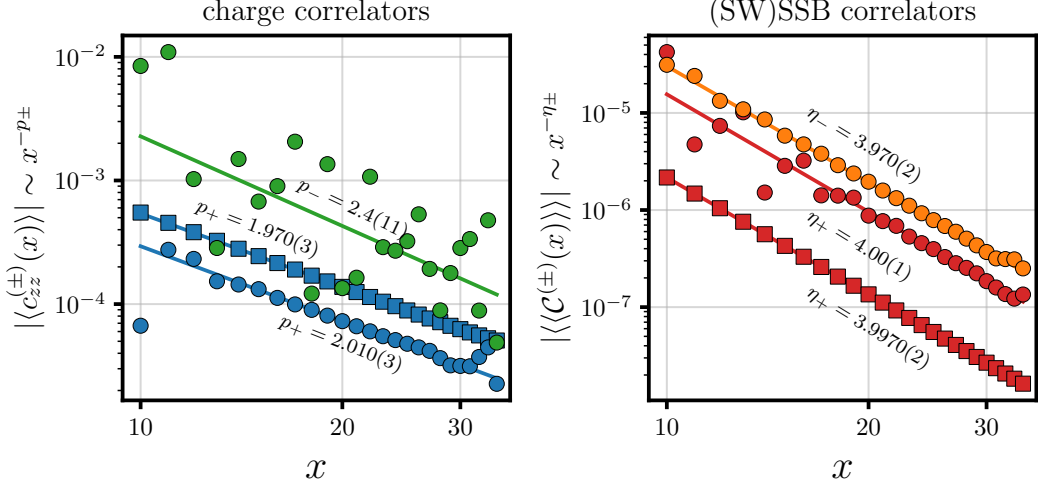


FIG. 9. U(1) (off-)diagonal charge fluctuations for phase measurements ($r = 1$). Charge (left) and SW-SSB/SSB (right) correlation functions in the charge-coherent (circles) and charge-fuzzy (squares) phases. In the coherent phase ($\Gamma_p = 4.8$), both $\langle\langle c_{zz}^{(\pm)}(x) \rangle\rangle = \langle\tilde{q}_\pm(i)\tilde{q}_\pm(i+x) \rangle$ and Rényi-2 correlators $\langle\langle C^{(\pm)}(x) \rangle\rangle$ decay as power laws, whereas in the fuzzy phase ($\Gamma_p = 1.2$) only $\langle\langle c_{zz}^{(+)}(x) \rangle\rangle$ (blue) and $\langle\langle C^{(+)}(x) \rangle\rangle$ (red) retain power-law behavior. Solid lines denote linear fits to the correlators on log-log scales, from which the exponents p_\pm and η_\pm are extracted. For additional details on the behavior of these exponents, see Appendix J.

inherited from the glassy SSB correlator (see Eq. (65)),

$$[\mathcal{C}^{(-)}(x)]_{\text{sw}} = \mathbb{E}_{\mathbf{m}} \left[|\langle S_0^+ S_x^- \rangle_{\mathbf{m}}|^2 \right] \sim x^{-\eta_-}, \quad (91)$$

as predicted by the effective Hamiltonian analysis above. Our numerical results for finite S are summarized in Figs. 10 and 11.

For $S = \frac{1}{2}$, when measurements are restricted to h_i alone, it is impossible to support true U(1) order, and all correlations are short-ranged, consistent with strong quantum fluctuations generated by the noncommutativity of phase measurements. Using the POVMs defined above with $N_\phi = 10$, even at $S = \frac{1}{2}$, we observe signatures of a charge-coherent regime: an initial Néel state evolves into one with power-law EA correlations, $\mathcal{C}^{(-)}(x) \sim x^{-\eta_-}$, and logarithmically scaling entanglement entropy at late times, indicating QLRO and qualitatively agreeing with the analysis above. Additional numerical details and finite-size scaling are presented in Appendix L.

VI. DISCUSSION AND OUTLOOK

In this work we investigated measurement-induced phases and transitions in G -symmetric monitored quantum circuits and showed that late-time and steady-state properties are organized by spontaneous symmetry breaking (SSB) of the n -ensemble symmetry group $\mathcal{G}^{(n)}$. At finite replica index n , the relevant subgroups are replica permutations \mathcal{S}_n , permutation-invariant transformations \bar{G} , and permutation-asymmetric (inter-replica)

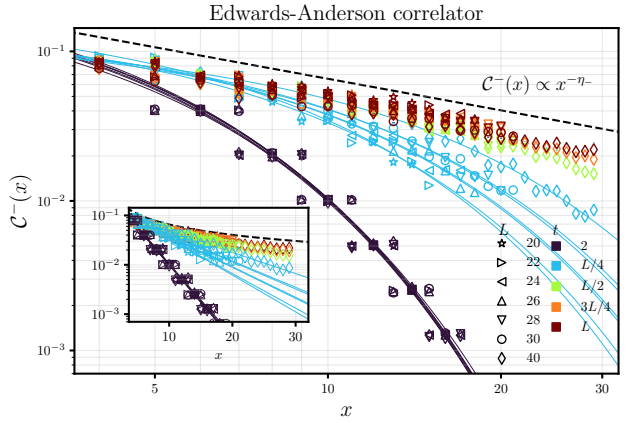


FIG. 10. Scaling of Edwards–Anderson correlator. Scaling of the SSB correlator, which takes the form of an EA correlator, $C_x^{(\pm)} = \sum_{\mathbf{m}} p_{\mathbf{m}} |\langle S_0^+ S_x^- \rangle_{\mathbf{m}}|^2$, in the measurement-only circuit for local spin $S = \frac{1}{2}$ and $N_\phi = 10$ sampled phase angles for the POVMs described in Appendix K. Starting from an initial Néel state, the correlator exhibits an apparent crossover from exponential to power-law decay as a function of circuit depth t/L . The black dashed line illustrates a power-law fit (e.g., at $t = L$) with exponent $\eta_- = 0.70(2)$. The inset shows the same data on a semi-log plot, highlighting finite correlation-length behavior at $O(1)$ times.

transformations \tilde{G} , with the latter two each splitting according to the action of Hermitian conjugation, $\mathbb{Z}_2^{\mathbb{H}}$, into diagonal and off-diagonal components, G_\pm and \tilde{G}_\pm . In this language, the entanglement, charge-sharpening, and

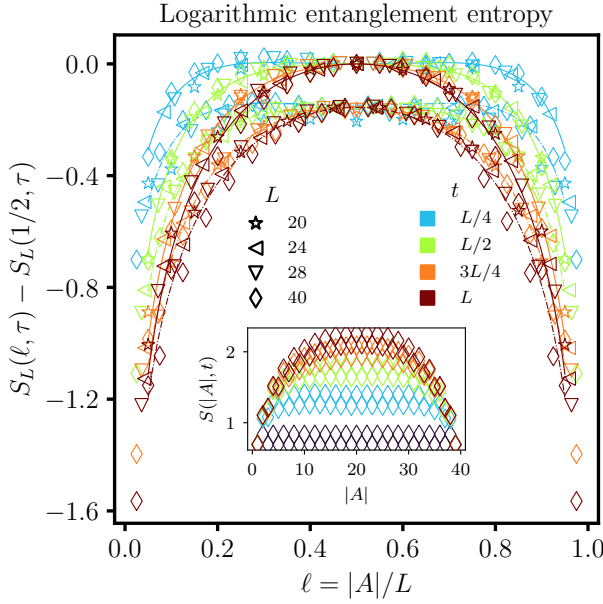


FIG. 11. Entanglement-entropy profiles. Scaling of the subsystem entanglement entropy (EE) at times $t = L/4, L/2, 3L/4, L$ (blue, green, orange, maroon) in the measurement-only circuit for local spin $S = \frac{1}{2}$ and $N_\phi = 10$ sampled phase angles, using the phase POVMs of Appendix K. (*Main panel*): Evolving an initial Néel product state, $S_L(\ell, \tau)$ develops universal logarithmic scaling, signaled by collapse of the data for each $\tau = t/L$ onto the L -independent quantity $S_L(\ell, \tau) - S_L(1/2, \tau)$ with $\ell = |A|/L$. Due to the initial state, the EE oscillates between even and odd subsystem sizes; we capture the logarithmic behavior by fitting the even and odd branches separately to a log-sine profile typical of CFTs with open boundaries (solid and dash-dotted lines, respectively). (*Inset*): Time evolution of the EE profile for $L = 40$, illustrating a crossover from area-law to logarithmic subsystem EE.

charge-coherence transitions are controlled by SSB of \mathcal{S}_n , $\tilde{\mathcal{G}}_+$, and $\tilde{\mathcal{G}}_-$, respectively.

In finite systems with Abelian G , charge measurements ultimately purify each trajectory and sharpen into a single charge sector. Nonetheless, n -ensemble order leaves universal signatures in steady-state scaling laws and correlators. Area-law entanglement corresponds to unbroken \mathcal{S}_n , whereas volume-law entanglement corresponds to broken \mathcal{S}_n . Area-law subsystem charge-variance and short-range diagonal charge fluctuations indicate unbroken $\tilde{\mathcal{G}}_+$, while logarithmic subsystem charge variance and algebraic or non-decaying diagonal charge correlations signal broken $\tilde{\mathcal{G}}_+$. Similarly, short-range off-diagonal charge correlations indicate unbroken $\tilde{\mathcal{G}}_-$, whereas algebraic or non-decaying behavior indicates broken $\tilde{\mathcal{G}}_-$.

A central ingredient in our analysis is an *activity bias* in the effective Hamiltonian for $n > 1$ ensembles with continuous G . Although related effects had been observed previously, we showed that this bias arises naturally from

the warped Born rule $p_{\mathbf{m}} \mapsto p_{\mathbf{m}}^{(n)} \propto \frac{p_{\mathbf{m}}^n}{\sum_{\mathbf{m}} p_{\mathbf{m}}^n}$ for systems with diffusing charges. Due to the presence of these charges, the warping generates an effective line tension that suppresses trajectories with large charge displacement and drives the effective dynamics towards phase-separated charge configurations. We showed that the qualitative physics expected from an unbiased effective Hamiltonian is recovered by constraining $\mathcal{H}^{(n)}$ to a sector with uniform physical charge density, in which this activity bias is absent.

Within this constrained sector, each phase is associated with a universal decay timescale for a corresponding information-theoretic quantity, set by an appropriate ensemble charge gap. These gaps exhibit an Anderson tower-of-states (TOS) scaling that depend only on whether the relevant symmetry is continuous or discrete and whether it is broken or not. The purification time is governed by the splitting between \mathcal{S}_n sectors and scales as either $\mathcal{O}(1)$ or e^V for systems of volume V . The charge-sharpening time is controlled by splittings between diagonal, permutation-asymmetric ($\tilde{\mathcal{G}}_+$) sectors, while the charge-decoherence time is controlled by splittings between off-diagonal ($\tilde{\mathcal{G}}_-$) sectors. For these continuous G , these gaps scale as either $\mathcal{O}(1)$ or V^{-1} , leading to charge-related timescales of order V in SSB phases, while a polynomial degeneracy of low-lying modes in the symmetric phases yields a logarithmic ($\log V$) relaxation timescale.

We provided concrete evidence for this phase structure in U(1)-symmetric circuits, combining a variational analysis of the constrained effective Hamiltonian with exact numerics for a one-dimensional, phase-measurement-only qubit circuit. A key result is the identification of a U(1) *charge-coherent* phase, in which noncommuting phase measurements generate a non-equilibrium steady state with long-range spin-spin correlations and logarithmic scaling of the entanglement entropy, consistent with QLRO. We further extended the framework to \mathbb{Z}_2 -symmetric circuits, where the variational constraint is unnecessary, as detailed in the Appendix I, and reproduced the ensemble-SSB structure seen in earlier studies [16, 34, 47, 48].

Our effective Hamiltonian description does not address the intrinsic uncertainty of any finite-spin representation of relative bond phases. Additionally, it causes warping in the quantum fluctuations generated by the noncommutativity of phase measurements. Specifically, the $n > 1$ effective Hamiltonian is only sensitive to the non-commutativity of $2n$ -products of measurements, rather than those of single copies. Both the intrinsic phase uncertainty and the non-commutativity of measurements can destabilize charge coherence in parts of the phase diagram. In forthcoming work, we analyze when the charge-coherent phase is stable against such fluctuations and how they modify the associated critical behavior.

Several questions remain open. Most notably, the phase structure for the intermediate regime where all three interactions are in competition. Additionally, while

there have been studies on charge sharpening criticality [49], the nature of the transitions into the charge-coherent phase and their critical properties merit further study; the full phase diagram may contain multiple multicritical points of different orders. For U(1) monitored random circuits (MRCs) in $D \geq 2$, our results suggest an interesting, finite-time transitions at a critical time t_c , when long-range charge correlations emerge between initially uncorrelated points. Related finite-time phenomena have already been discussed in MRCs for diagonal charge degrees of freedom [14, 50] and for complexity and entanglement [51, 52]. Stabilizing long-range off-diagonal charge correlations in such settings suggests a route to robust quantum memories in spin-glass-like configurations as proposed in Ref. [53], and connects naturally to the quantum, classical, and lost-memory phases associated with trivial, weak, and strong \mathbb{Z}_2 SSB in Ref. [54]. Our framework also points to a broader connection between ensemble symmetry breaking and learnability transitions, extending the picture developed for charge sharpening [28, 33].

Methodologically, our finite- n variational framework for continuous symmetries provides a practical tool for analyzing symmetric monitored circuits. Future work includes a more rigorous justification of the mean-field uniform-charge constraint, the construction of microscopic models that realize all ensemble-SSB phases with a controlled replica limit, and effective field theory descriptions that classify the associated transitions and critical properties. Such developments may also clarify how to incorporate the noncommutativity of phase measurements

in a controlled way.

Beyond Abelian groups, we expect the framework to extend to non-Abelian symmetries and kinetically constrained dynamics. In particular, “spin sharpening” has already been explored for non-Abelian symmetries [55, 56]; it would be interesting to study local “spin-current” measurements and their ensemble SSB structure in such systems. Another direction is to incorporate measurement-based feedback, characteristic of adaptive circuits with absorbing states. While discrete-symmetry cases are comparatively well understood [57–59], achieving similarly robust behavior with continuous symmetries remains an open challenge [60].

Notes added: We draw attention for the work on monitored symmetric circuits using holographic approach [33].

ACKNOWLEDGMENTS

The authors thank Akash Vijay, Romain Vasseur, Ehud Altman, Ethan Lake, Pablo Sala, Max McGinley, Sam Garratt, Zack Weinstein, Zijian Wang, and Ruihua Fan for insightful discussions. O.O is supported by the UC President’s Postdoctoral Fellowship. R.P.L. acknowledges support by the Department of Defense (DoD) through the National Defense Science and Engineering Graduate (NDSEG) Fellowship Program. J.Y.L acknowledges support by the faculty startup grant at the University of Illinois, Urbana-Champaign, and the IBM-Illinois Discovery Accelerator Institute.

-
- [1] Y. Li, X. Chen, and M. P. A. Fisher, Quantum zeno effect and the many-body entanglement transition, *Phys. Rev. B* **98**, 205136 (2018).
 - [2] B. Skinner, J. Ruhman, and A. Nahum, Measurement-induced phase transitions in the dynamics of entanglement, *Phys. Rev. X* **9**, 031009 (2019).
 - [3] A. Chan, R. M. Nandkishore, M. Pretko, and G. Smith, Unitary-projective entanglement dynamics, *Phys. Rev. B* **99**, 224307 (2019).
 - [4] M. P. Fisher, V. Khemani, A. Nahum, and S. Vijay, Random quantum circuits, *Annual Review of Condensed Matter Physics* **14**, null (2023).
 - [5] R. Vasseur, A. C. Potter, Y.-Z. You, and A. W. W. Ludwig, Entanglement transitions from holographic random tensor networks, *Phys. Rev. B* **100**, 134203 (2019).
 - [6] A. Nahum, S. Vijay, and J. Haah, Operator spreading in random unitary circuits, *Phys. Rev. X* **8**, 021014 (2018).
 - [7] T. Zhou and A. Nahum, Emergent statistical mechanics of entanglement in random unitary circuits, *Phys. Rev. B* **99**, 174205 (2019).
 - [8] Y. Bao, S. Choi, and E. Altman, Theory of the phase transition in random unitary circuits with measurements, *Phys. Rev. B* **101**, 104301 (2020).
 - [9] C.-M. Jian, Y.-Z. You, R. Vasseur, and A. W. W. Ludwig, Measurement-induced criticality in random quantum circuits, *Phys. Rev. B* **101**, 104302 (2020).
 - [10] A. Nahum, S. Roy, B. Skinner, and J. Ruhman, Measurement and entanglement phase transitions in all-to-all quantum circuits, on quantum trees, and in landau-ginsburg theory, *PRX Quantum* **2**, 010352 (2021).
 - [11] J. M. Koh, S.-N. Sun, M. Motta, and A. J. Minnich, Measurement-induced entanglement phase transition on a superconducting quantum processor with mid-circuit readout, *Nature Physics* **19**, 1314 (2023).
 - [12] C. Noel, P. Niroula, D. Zhu, A. Risinger, L. Egan, D. Biswas, M. Cetina, A. V. Gorshkov, M. J. Gullans, D. Huse, and C. Monroe, Measurement-induced quantum phases realized in a trapped-ion quantum computer, *Nature Physics* **18**, 760 (2022).
 - [13] U. Agrawal, A. Zabalo, K. Chen, J. H. Wilson, A. C. Potter, J. Pixley, S. Gopalakrishnan, and R. Vasseur, Entanglement and Charge-Sharpening Transitions in U(1) Symmetric Monitored Quantum Circuits, *Physical Review X* **12**, 041002 (2022), publisher: American Physical Society.
 - [14] F. Barratt, U. Agrawal, S. Gopalakrishnan, D. A. Huse, R. Vasseur, and A. C. Potter, Field Theory of Charge Sharpening in Symmetric Monitored Quantum Circuits, *Physical Review Letters* **129**, 120604 (2022), publisher: American Physical Society.
 - [15] H. Guo, M. S. Foster, C.-M. Jian, and A. W. W. Ludwig, Field theory of monitored, interacting fermion dynamics

- with charge conservation (2024), arXiv:2410.07317 [cond-mat.stat-mech].
- [16] Y. Bao, S. Choi, and E. Altman, Symmetry enriched phases of quantum circuits, *Annals of Physics* **435**, 168618 (2021).
- [17] J. Y. Lee, C.-M. Jian, and C. Xu, Quantum criticality under decoherence or weak measurement, *PRX Quantum* **4**, 030317 (2023).
- [18] O. Ogunnaike, J. Feldmeier, and J. Y. Lee, Unifying Emergent Hydrodynamics and Lindbladian Low-Energy Spectra across Symmetries, Constraints, and Long-Range Interactions, *Physical Review Letters* **131**, 220403 (2023), publisher: American Physical Society.
- [19] P. Sala, S. Gopalakrishnan, M. Oshikawa, and Y. You, Spontaneous strong symmetry breaking in open systems: Purification perspective, *Phys. Rev. B* **110**, 155150 (2024).
- [20] L. A. Lessa, R. Ma, J.-H. Zhang, Z. Bi, M. Cheng, and C. Wang, Strong-to-weak spontaneous symmetry breaking in mixed quantum states (2024), arXiv:2405.03639 [quant-ph].
- [21] D. Gu, Z. Wang, and Z. Wang, Spontaneous symmetry breaking in open quantum systems: strong, weak, and strong-to-weak (2024), arXiv:2406.19381 [quant-ph].
- [22] J. Kim, E. Altman, and J. Y. Lee, Error threshold of syk codes from strong-to-weak parity symmetry breaking (2024), arXiv:2410.24225 [quant-ph].
- [23] N. Ziereis, S. Moudgalya, and M. Knap, Strong-to-weak symmetry breaking phases in steady states of quantum operations (2025), arXiv:2509.09669 [cond-mat.stat-mech].
- [24] P. W. Anderson, An approximate quantum theory of the antiferromagnetic ground state, *Phys. Rev.* **86**, 694 (1952).
- [25] G. Misguich and P. Sindzingre, Detecting spontaneous symmetry breaking in finite-size spectra of frustrated quantum antiferromagnets, *Journal of Physics: Condensed Matter* **19**, 145202 (2007).
- [26] H. Tasaki, Long-range order, “tower” of states, and symmetry breaking in lattice quantum systems, *Journal of Statistical Physics* **174**, 735 (2019).
- [27] In higher dimensions this becomes true long-range order (SSB); in 1+1D it is only quasi-long-range.
- [28] H. Singh, R. Vasseur, A. C. Potter, and S. Gopalakrishnan, Mixed-state learnability transitions in monitored noisy quantum dynamics (2025), arXiv:2503.10308 [quant-ph].
- [29] M.-D. Choi, Completely positive linear maps on complex matrices, *Linear Algebra and its Applications* **10**, 285 (1975).
- [30] For 1D circuits, the relative degeneracy of ground and excited states contributes to the charge sharpening and decoherence time scales. See Sec. IV A for details.
- [31] H. Tasaki, Long-Range Order, “Tower” of States, and Symmetry Breaking in Lattice Quantum Systems, *Journal of Statistical Physics* **174**, 735 (2019).
- [32] A. Wietek, M. Schuler, and A. M. Läuchli, Studying continuous symmetry breaking using energy level spectroscopy (2017), arXiv:1704.08622 [cond-mat.str-el].
- [33] A. Vijay and J. Y. Lee, Holographically emergent gauge theory in symmetric quantum circuits (2025), arXiv:2511.21685 [quant-ph].
- [34] Y. Li and M. P. A. Fisher, Decodable hybrid dynamics of open quantum systems with F_2 symmetry, *Phys. Rev. B* **108**, 214302 (2023).
- [35] F. Ares, S. Murciano, and P. Calabrese, Entanglement asymmetry as a probe of symmetry breaking, *Nature Communications* **14**, 2036 (2023).
- [36] Z. Ma, C. Han, Y. Meir, and E. Sela, Symmetric inseparability and number entanglement in charge-conserving mixed states, *Phys. Rev. A* **105**, 042416 (2022).
- [37] Y. Chen and H. W. Lin, Signatures of global symmetry violation in relative entropies and replica wormholes, *Journal of High Energy Physics* **2021**, 10.1007/jhep03(2021)040 (2021).
- [38] P. Hayden, S. Nezami, X.-L. Qi, N. Thomas, M. Walter, and Z. Yang, Holographic duality from random tensor networks, *Journal of High Energy Physics* **2016**, 1 (2016).
- [39] S. Moudgalya and O. I. Motrunich, Symmetries as Ground States of Local Superoperators (2023), arXiv:2309.15167 [cond-mat, physics:hep-th, physics:math-ph, physics:quant-ph].
- [40] S. N. Hearth, M. O. Flynn, A. Chandran, and C. R. Laumann, Unitary k-designs from random number-conserving quantum circuits (2023), arXiv:2306.01035 [cond-mat.stat-mech].
- [41] A. Impertro, S. Karch, J. F. Wienand, S. Huh, C. Schweizer, I. Bloch, and M. Aidelsburger, Local readout and control of current and kinetic energy operators in optical lattices, *Phys. Rev. Lett.* **133**, 063401 (2024).
- [42] R. L. Jack, I. R. Thompson, and P. Sollich, Hyperuniformity and phase separation in biased ensembles of trajectories for diffusive systems, *Phys. Rev. Lett.* **114**, 060601 (2015).
- [43] V. Lecomte, J. P. Garrahan, and F. van Wijland, Inactive dynamical phase of a symmetric exclusion process on a ring, *Journal of Physics A: Mathematical and Theoretical* **45**, 175001 (2012).
- [44] Note that the convention used is for transformations that are even or odd under the transpose action $r \leftrightarrow l$. These sectors have opposite parity for $\mathbb{Z}_2^{\mathbb{H}}$. Due to the complex conjugation involved in $\mathbb{Z}_2^{\mathbb{H}}$, the generators, Q_+ , of “diagonal” symmetries with representation $U_+ = e^{i\theta_+ Q_+}$, are actually odd under $\mathbb{Z}_2^{\mathbb{H}}$.
- [45] For U(1) symmetries, one can define paired order parameters $o_+^{(1,2)}$ and $\tilde{o}^{(1,2)}$ that are two-replica analogues of the nematic order parameters in Ref. [61]; their commutators generate replica-average and inter-replica charges, e.g., $[o_+^{(1)}, o_+^{(2)}] \propto i(\bar{Q}_+ + \hat{Q}_+)$ and $[\tilde{o}^{(1)}, \tilde{o}_+^{(2)}] \propto i(\hat{Q}_+ + \tilde{Q}_-)$.
- [46] J. Hauschild, J. Unfried, S. Anand, B. Andrews, M. Bintz, U. Borla, S. Divic, M. Drescher, J. Geiger, M. Hefel, K. Hémery, W. Kadow, J. Kemp, N. Kirchner, V. S. Liu, G. Möller, D. Parker, M. Rader, A. Romen, S. Scalet, L. Schoonderwoerd, M. Schulz, T. Soejima, P. Thoma, Y. Wu, P. Zechmann, L. Zweng, R. S. K. Mong, M. P. Zaletel, and F. Pollmann, Tensor network Python (TeNPy) version 1, *SciPost Phys. Codebases* , 41 (2024).
- [47] A. Lavasani, Y. Alavirad, and M. Barkeshli, Measurement-induced topological entanglement transitions in symmetric random quantum circuits, *Nature Physics* **17**, 342 (2021).
- [48] S. Sang and T. H. Hsieh, Measurement-protected quantum phases, *Phys. Rev. Res.* **3**, 023200 (2021).
- [49] A. Chakraborty, K. Chen, A. Zabalo, J. H. Wilson, and J. H. Pixley, Charge and entanglement critical-

- ity in a u(1)-symmetric hybrid circuit of qubits (2023), arXiv:2307.13038 [cond-mat.dis-nn].
- [50] J. Hauser, K. Su, H. Ha, J. Lloyd, T. G. Kiely, R. Vasseur, S. Gopalakrishnan, C. Xu, and M. P. A. Fisher, Strong-to-weak symmetry breaking in open quantum systems: From discrete particles to continuum hydrodynamics (2026), arXiv:2602.16045 [quant-ph].
- [51] J. C. Napp, R. L. La Placa, A. M. Dalzell, F. G. S. L. Brandão, and A. W. Harrow, Efficient classical simulation of random shallow 2d quantum circuits, *Phys. Rev. X* **12**, 021021 (2022).
- [52] Y. Bao, M. Block, and E. Altman, Finite-time teleportation phase transition in random quantum circuits, *Phys. Rev. Lett.* **132**, 030401 (2024).
- [53] B. Placke, T. Rakovszky, N. P. Breuckmann, and V. Khemani, Topological quantum spin glass order and its realization in qldpc codes (2024), arXiv:2412.13248 [quant-ph].
- [54] M. Pütz, S. J. Garratt, H. Nishimori, S. Trebst, and G.-Y. Zhu, Learning transitions in classical ising models and deformed toric codes (2025), arXiv:2504.12385 [cond-mat.stat-mech].
- [55] S. Majid, U. Agrawal, S. Gopalakrishnan, A. C. Potter, R. Vasseur, and N. Y. Halpern, Critical phase and spin sharpening in SU(2)-symmetric monitored quantum circuits, *Physical Review B* **108**, 054307 (2023), publisher: American Physical Society.
- [56] X. Feng, N. Fishchenko, S. Gopalakrishnan, and M. Ippoliti, Charge and spin sharpening transitions on dynamical quantum trees, *Quantum* **9**, 1692 (2025).
- [57] M. N. Ivaki, T. Ojanen, and A. G. Moghaddam, Noise resilience in adaptive and symmetric monitored quantum circuits, *npj Quantum Information* **11**, 111 (2025).
- [58] H. Ha, D. A. Huse, and R. Samajdar, Absorbing state transitions with discrete symmetries (2025), arXiv:2502.08702 [cond-mat.stat-mech].
- [59] Z. Li and Z.-X. Luo, Exact, Average, and Broken Symmetries in a Simple Adaptive Monitored Circuit, *Quantum* **9**, 1771 (2025), arXiv:2312.17309 [quant-ph].
- [60] J. Hauser, Y. Li, S. Vijay, and M. P. A. Fisher, Continuous symmetry breaking in adaptive quantum dynamics, *Phys. Rev. B* **109**, 214305 (2024).
- [61] H. Watanabe, H. Katsura, and J. Y. Lee, Critical spontaneous breaking of u(1) symmetry at zero temperature in one dimension, *Physical Review Letters* **133**, 10.1103/physrevlett.133.176001 (2024).
- [62] S. Aaronson, Is quantum mechanics an island in theory-space? (2004), arXiv:quant-ph/0401062 [quant-ph].
- [63] V. Khemani, A. Vishwanath, and D. A. Huse, Operator spreading and the emergence of dissipative hydrodynamics under unitary evolution with conservation laws, *Phys. Rev. X* **8**, 031057 (2018).
- [64] S. Leontica and M. McGinley, Purification dynamics in a continuous-time hybrid quantum circuit model, *Physical Review B* **108**, 174308 (2023), publisher: American Physical Society.
- [65] S. Gopalakrishnan, E. McCulloch, and R. Vasseur, Monitored fluctuating hydrodynamics (2025), arXiv:2504.02734 [cond-mat.stat-mech].
- [66] Z. Weinstein, Efficient detection of strong-to-weak spontaneous symmetry breaking via the rényi-1 correlator, *Physical Review Letters* **134**, 10.1103/physrevlett.134.150405 (2025).
- [67] J. Fröhlich and T. Spencer, The phase transition in the one-dimensional Ising Model with $1/r^2$ interaction energy, *Communications in Mathematical Physics* **84**, 87 (1982).
- [68] J. Bhattacharjee, S. Chakravarty, J. L. Richardson, and D. J. Scalapino, Some properties of a one-dimensional ising chain with an inverse-square interaction, *Phys. Rev. B* **24**, 3862 (1981).
- [69] J. V. José, L. P. Kadanoff, S. Kirkpatrick, and D. R. Nelson, Renormalization, vortices, and symmetry-breaking perturbations in the two-dimensional planar model, *Phys. Rev. B* **16**, 1217 (1977).
- [70] D. Benedetti, E. Lauria, D. Mazáč, and P. van Vliet, One-dimensional ising model with $1/r^{1.99}$ interaction, *Phys. Rev. Lett.* **134**, 201602 (2025).

Appendix A: Decoherence effects

In this section, we incorporate decoherence into our effective Hamiltonian in close analogy to the Brownian Hamiltonian description of unitary evolution. The key difference is that decoherence emerges from unitaries acting *within* a single replica at a time, rather than diagonally across all replicas.

Let $\rho_t^{(n)} \equiv \rho_t^{\otimes n}$ denote the n -copy density matrix at time t . A short-time update generated by replica-local Brownian unitaries can be written as

$$\rho_{t+\delta t}^{(n)} = \int dB p(dB) \sum_{k=1}^n U_t^{(k)}(dB) \rho_t^{(n)} U_t^{(k)\dagger}(dB), \quad (\text{A1})$$

where $U_t^{(k)}(dB) \equiv e^{-ih^{(k)}(dB)}$ acts nontrivially only on replica k (and as the identity on all other replicas), and $p(dB)$ is the Brownian measure. Averaging over the noise and expanding to second order in dB produces an effective n -copy decoherence Hamiltonian

$$\mathcal{H}_{\mathcal{D}}^{(n)} \equiv \frac{\gamma_{\mathcal{D}}}{2} \sum_i \sum_{k=1}^n \left([h_i^{(k)} \otimes \mathbb{I} - \mathbb{I} \otimes (h_i^{(k)})^T] \right)^2. \quad (\text{A2})$$

Compared to the unitary Brownian term, the only structural difference is that the sum over replicas $\sum_{k=1}^n$ appears *outside* the square, rather than inside. As a result, $\mathcal{H}_{\mathcal{D}}^{(n)}$ explicitly breaks replica permutation symmetry \mathcal{S}_n : it energetically selects the permutation that matches the left and right indices within each *individual* copy. The unique permutation-polarized ground state (within a fixed physical-charge sector) is therefore $|\mathbb{I}^{\otimes n}\rangle$, corresponding to the identity permutation on each replica.

Any finite decoherence rate $\gamma_{\mathcal{D}} > 0$ thus acts as a symmetry-breaking field for \mathcal{S}_n . In particular, it prevents volume-law phases from reaching a permutation-symmetric, highly purified steady state. Instead, volume-law states select the identity polarization for the ground state, and acquire exponentially small steady-state purities $\text{Tr}[\rho_{\infty}^2] \sim e^{-cL}$, where c is a constant related to the ratio of a weak $\gamma_{\mathcal{D}}$ to other energy scales. In contrast, area-law states remain perturbatively close to \mathcal{S}_n .

symmetric configurations, so that the purity will remain finite: $\overline{\text{Tr}[\rho_\infty^2]} \sim \mathcal{O}(1)$.

Strongly symmetric dephasing. A noteworthy special case is *strictly* Q -conserving local dephasing, for example

$$h_i = S_i^z \quad \text{with} \quad Q = \sum_i S_i^z. \quad (\text{A3})$$

In this case, $\mathcal{H}_D^{(n)}$ commutes with all inter-replica charges (e.g., \tilde{Q}_\pm and \overline{Q}_\pm) and therefore does not induce symmetry breaking in the charge degrees of freedom. Concretely, the charge-sharp, charge-fuzzy, and charge-coherent phases described in the main text are all robust to weak Q -conserving dephasing. The robustness of phases related inter-replica symmetries, \tilde{G} , to such forms of decoherence has been emphasized in several works [28, 34].

This distinction is especially important for the charge-coherence variance $[\delta\Phi_Q^2]_{\text{sw}}$ and the SW-SSB correlator $[\mathcal{C}_x^{(+)}]_{\text{sw}}$, where decoherence allows mixed-state order to persist at late times. Recall that (for $n = 2$) the normalized charge-coherence measure can be written as

$$[\delta\Phi_Q^2]_{\text{sw}} \propto \frac{\langle\langle \text{SW} \| \tilde{Q}_-^2 \| \rho^{(k)} \rangle\rangle}{\langle\langle \text{SW} \| \rho^{(k)} \rangle\rangle}. \quad (\text{A4})$$

In the charge-fuzzy phase, the numerator $\langle\langle \text{SW} \| \tilde{Q}_-^2 \| \rho^{(k)} \rangle\rangle$ vanishes at late times because the ground state will be polarized towards the identity-permutation, which will require a finite energy to introduce any \tilde{Q}_- charge. The numerator only becomes finite in the charge-coherent phase, when both inter-replica charges are present in the identity-permutation.

Similarly, the SW-SSB correlator $[\mathcal{C}_x^{(+)}]_{\text{sw}}$ mixes the diagonal charges and, in the absence of decoherence, has a numerator of the form

$$\langle\langle \text{SW} \| \prod_{k=1}^n (S_{0,kL}^+ S_{x,kL}^-) (S_{0,kR}^+ S_{x,kR}^-) \| \rho^{(n)} \rangle\rangle \propto e^{-L} \quad (\text{A5})$$

in the charge-fuzzy phase, since only the identity polarization survives the exchange of \tilde{Q}_\pm charges with $\langle\langle \text{SW} \rangle\rangle$, but the overlap of these two opposite polarizations scales with e^{-L} . In contrast, the denominator is the SW overlap $\langle\langle \text{SW} \| \rho^{(n)} \rangle\rangle$, which remains $\mathcal{O}(1)$ because of the SW-polarization present in $\| \rho^{(n)} \rangle\rangle$. Consequently, $[\mathcal{C}_x^{(+)}]_{\text{sw}} \propto e^{-L}$ without decoherence.

When symmetric decoherence is present, only the identity polarization exists in $\| \rho^{(n)} \rangle\rangle$, and the purity that appears in the SW normalization acquires the same exponential suppression. More precisely,

$$\langle\langle \text{SW} \| \rho^{(n)} \rangle\rangle = \overline{\mathbb{E}_{\mathbf{m}}^{(n)} [\text{Tr}[\rho_{\mathbf{m}}^k]]} \sim e^{-L} \quad (\text{A6})$$

in both the charge-fuzzy and charge-coherent phases. In this case, both the numerator and denominator in

$[\mathcal{C}_x^{(+)}]_{\text{sw}}$ scale with e^{-L} , so the ratio becomes $\mathcal{O}(1)$ and the SW-SSB correlator remains finite in phases with diagonal charge order. Charge conserving decoherence thus modifies the normalization in such a way that mixed-state SW-SSB order can survive at late times while still preserving the underlying inter-replica charge symmetries.

Appendix B: Finite replica index, activity bias, and diffusive charges

In the main text we noted that the *warped Born rule* induced at finite replica index n ,

$$\mathbf{p}_{\mathbf{m}} \mapsto p_{\mathbf{m}}^{(n)} \equiv \frac{p_{\mathbf{m}}^n}{\sum_{\mathbf{m}'} p_{\mathbf{m}'}^n}, \quad (\text{B1})$$

can substantially alter the dynamics and information content of post-measurement ensembles [62]. For systems with continuous G , the unwarped probabilities $p_{\mathbf{m}}$ are finely tuned to yield diffusive charge transport; the warped distribution $p_{\mathbf{m}}^{(n)}$ upsets this balance, favoring low-activity, “phase-separated” configurations [42, 43]. Here we make these effects explicit in a simple classical toy model.

Activity bias from warping. Consider a classical diffusing charge modeled as a symmetric random walk. At each of t time steps, the particle moves with total probability p (split equally left/right) and remains at its current position with probability $1 - p$. We denote a left move by -1 , a right move by $+1$, and no move by 0 , and label a trajectory by a length- t string

$$\boldsymbol{\ell} := (\ell_1, \dots, \ell_t), \quad \ell_j \in \{-1, 0, +1\}. \quad (\text{B2})$$

The *activity* $a_{\boldsymbol{\ell}}$ of a trajectory is the number of nonzero steps, i.e., the number of times the particle moves. The probability of a given trajectory $\boldsymbol{\ell}$ with activity $a_{\boldsymbol{\ell}}$ is

$$p_{\boldsymbol{\ell}} = (1 - p)^{t - a_{\boldsymbol{\ell}}} \left(\frac{p}{2}\right)^{a_{\boldsymbol{\ell}}}. \quad (\text{B3})$$

Now consider two trajectories $\boldsymbol{\ell}$ and \mathbf{m} with activities $a_{\boldsymbol{\ell}}$ and $a_{\mathbf{m}}$. Under warping at replica index n , each microscopic trajectory is reweighted by $p_{\boldsymbol{\ell}}^n$, so their relative weight becomes

$$\frac{p_{\boldsymbol{\ell}}^{(n)}}{p_{\mathbf{m}}^{(n)}} = \left(\frac{p/2}{1 - p}\right)^{n(a_{\boldsymbol{\ell}} - a_{\mathbf{m}})}. \quad (\text{B4})$$

Next, we sum over trajectories with the same activity. For fixed activity, a , there are 2^a choices of directions for the nonzero steps and $\binom{t}{a}$ ways to choose their positions, so the total warped probability of having activity a is $P^{(n)}(a) = 2^a \binom{t}{a} p_{\boldsymbol{\ell}}^{(n)}$. The ratio of probabilities of having activity a and b is therefore

$$R_{a,b}^{(n)} = 2^{a-b} \frac{\binom{t}{a}}{\binom{t}{b}} \left(\frac{p/2}{1 - p}\right)^{n(a-b)}. \quad (\text{B5})$$

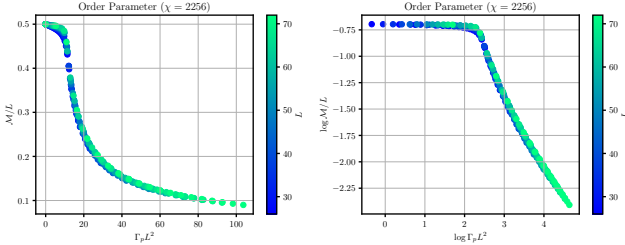


FIG. 12. Ground-state magnetization $\langle\langle m_z^2 \rangle\rangle$ of H_{eff} versus $\Gamma_p L^2$ for the U(1)-symmetric system, showing collapse consistent with the scaling $\Gamma_p^c \sim L^{-2}$.

To isolate the effect of warping, we compare this to the unwarped ($n = 1$) case:

$$\frac{R_{a,b}^{(n)}}{R_{a,b}^{(1)}} = \left(\frac{p/2}{1-p} \right)^{(n-1)(a-b)} = e^{-s_{\text{eff}}(a-b)} \quad (\text{B6})$$

where $s_{\text{eff}} = (n-1) \log \left(\frac{1-p}{p/2} \right)$ is an effective tension for activity or spacetime distance covered. For $p < 2/3$ (in particular for Haar-random circuits with $p = 1/2$ [63]), we have $(p/2)/(1-p) < 1$, so any $n > 1$ trajectories with *lower* activity ($a < b$) are exponentially *amplified* relative to the $n = 1$ (unwarped) ensemble. Thus, finite- n warping induces a strong bias against highly active trajectories.

In monitored circuits, charge measurements fix the endpoints of charge worldlines and allow this bias to manifest as an effective line tension between measurement events. Each charge measurement pins the position of the charge within a time window of typical length Γ_p^{-1} . Within such a window, charges move along trajectories with activity $l \lesssim \Gamma_p^{-1}$, and the trajectory weights are suppressed according to this activity. This suppression acts like an effective Boltzmann factor $e^{-s_{\text{eff}}l}$ that vanishes in the replica limit $n \rightarrow 1$. The warped ensemble can therefore be viewed as an *activity-biased* ensemble in the sense of the s -ensemble formalism for dynamical phase transitions in diffusive systems [42, 43].

Finite-size scaling consequence. Activity-biased diffusive systems exhibit a transition between hyperuniform and phase-separated dynamical phases at a critical bias $s_c \sim L^{-2}$ [42]. Translating to our setting, where s_{eff} is generated by the replica warping and the microscopic measurement rate Γ_p , yields a finite-size crossover scale

$$\Gamma_p^c \sim L^{-2}. \quad (\text{B7})$$

This is precisely what we observe in the U(1)-symmetric effective model: the ground-state magnetization collapses when plotted as a function of $\Gamma_p L^2$ (Fig. 12), indicating that the relevant control parameter is $\Gamma_p L^2$ rather than Γ_p alone. Physically, the diffusive timescale scales as L^2 , so $\Gamma_p \ll L^{-2}$ implies that charges have time to fully spread between successive measurements. In this

regime the effective activity tension acts only as a weak perturbation on the nearly uniform charge profile, while for $\Gamma_p \gtrsim L^{-2}$ it becomes strong enough to favor phase-separated, low-activity configurations.

Appendix C: Purification Timescale and the $\Theta(t)$ Function

We begin with the permutation variance $[\delta Q_\sigma^2]$, following a route parallel to Ref. [64]. From the circuit representation shown in the main text, the variance element with identity-permutation boundary conditions is

$$[\delta Q_\sigma^2(t)]_{\text{id}} = \frac{1}{4} - \frac{1}{4} \overline{\left(\mathbb{E}_{\mathbf{m}}^{(2)} [\text{Tr}(\rho_{\mathbf{m}}^2(t))] \right)^2}. \quad (\text{C1})$$

Although the analysis holds for generic initial states, it will be convenient to start from $\|\rho^{(2)}(0)\rangle = \|\mathbb{I}^{\otimes 2}\rangle$. Then, the purity can be written as

$$\overline{[\text{Tr} \rho_A^2]} = \frac{\langle\langle \mathbb{I}^{\otimes 2} | \prod_j \mathcal{T}_j^r | \rho^{(2)}(t) \rangle\rangle}{\langle\langle \mathbb{I}^{\otimes 2} | \rho^{(2)}(t) \rangle\rangle} = \frac{1 - \Theta(t)}{1 + \Theta(t)}, \quad (\text{C2})$$

where we introduce the S_2 -symmetric/antisymmetric combinations $\|\pm\rangle = (\|\mathbb{I}^{\otimes 2}\rangle \pm \|\text{SW}\rangle)/\sqrt{2}$ to define

$$\Theta(t) = \frac{\langle\langle -|e^{-t\mathcal{H}^{(2)}}|-\rangle\rangle}{\langle\langle +|e^{-t\mathcal{H}^{(2)}}|+\rangle\rangle}. \quad (\text{C3})$$

The purification timescale follows from the decay of $\Theta(t)$. At late times, this simplifies to the form

$$\Theta(t) \underset{t \rightarrow \infty}{\approx} \frac{e^{-t\delta_0}}{1 + C_\pi e^{-t\Delta^+}}, \quad (\text{C4})$$

From which we see the relevant time scale is $t_\pi \sim \delta_0^{-1}$, which sets the purification time

We can similarly express the decay of the permutation variance in terms of $\Theta(t)$. If we explicitly expand its definition as a function of $\Theta(t)$, it becomes

$$[\delta Q_\sigma^2]_{\text{id}} = \frac{1}{4} \left(1 - \left(\frac{1 - \Theta(t)}{1 + \Theta(t)} \right)^2 \right) = \frac{\Theta(t)}{(1 + \Theta(t))^2}. \quad (\text{C5})$$

Since we have defined the initial state such that $\Theta(0) = 1$, $[\delta Q_\sigma^2(t)]_{\text{id}}$ will scale the same as $\Theta(t)$. Below, we make this scaling form explicit.

Spectral decomposition in the S_2 sectors. Let $\{\|\Omega_a^\pm\rangle\}$ denote the ground states in the even (+) and odd (-) S_2 sectors of $\mathcal{H}^{(2)}$, and $\{\|\psi_b^\pm\rangle\}$ the corresponding first excited states (with possible degeneracies indexed by a, b). For large t ,

$$\begin{aligned} e^{-t\mathcal{H}^{(2)}} |\pm\rangle &\underset{t \rightarrow \infty}{\approx} \sum_a c_{0,a}^\pm e^{-\epsilon_0^\pm t} |\Omega_a^\pm\rangle \\ &+ \sum_b c_{1,b}^\pm e^{-(\epsilon_0^\pm + \Delta^\pm)t} |\psi_b^\pm\rangle, \end{aligned} \quad (\text{C6})$$

where ϵ_0^\pm are the sector minima, Δ^\pm are the intra-sector gaps to the first excitations, and

$$c_{0,a}^\pm \equiv \langle\langle \pm \|\Omega_a^\pm \rangle\rangle, \quad c_{1,b}^\pm \equiv \langle\langle \pm \|\psi_b^\pm \rangle\rangle. \quad (\text{C7})$$

Since the true ground state is in the \mathcal{S}_2 -even sector, $\epsilon_0^+ \leq \epsilon_0^-$; we set $\epsilon_0^+ = 0$ and define the \mathcal{S}_2 sector gap

$$\delta_0 \equiv \epsilon_0^- \geq 0. \quad (\text{C8})$$

Then,

$$\langle\langle -\| - (t) \rangle\rangle \underset{t \rightarrow \infty}{\approx} \sum_a |c_{0,a}^-|^2 e^{-t\delta_0} + \sum_b |c_{1,b}^-|^2 e^{-(\delta_0 + \Delta^-)t}, \quad (\text{C9})$$

$$\langle\langle +\| + (t) \rangle\rangle \underset{t \rightarrow \infty}{\approx} \sum_a |c_{0,a}^+|^2 + \sum_b |c_{1,b}^+|^2 e^{-\Delta^+ t}. \quad (\text{C10})$$

To leading order in t , we can drop the subleading $e^{-(\delta_0 + \Delta^-)t}$ term in the numerator, obtaining

$$\Theta(t) \underset{t \rightarrow \infty}{\approx} \frac{\sum_a |c_{0,a}^-|^2}{\sum_a |c_{0,a}^+|^2} \frac{e^{-t\delta_0}}{1 + \frac{\sum_b |c_{1,b}^+|^2}{\sum_a |c_{0,a}^+|^2} e^{-t\Delta^+}}. \quad (\text{C11})$$

Finally, we define the (nonuniversal) constants

$$C_0 \equiv \frac{\sum_a |c_{0,a}^-|^2}{\sum_a |c_{0,a}^+|^2}, \quad C_\pi \equiv \frac{\sum_b |c_{1,b}^+|^2}{\sum_a |c_{0,a}^+|^2}, \quad (\text{C12})$$

to recover the late-time structure used in the main text,

$$\Theta(t) \underset{t \rightarrow \infty}{\approx} C_0 \frac{e^{-t\delta_0}}{1 + C_\pi e^{-t\Delta^+}}. \quad (\text{C13})$$

The prefactor, C_0 , only affects the overall normalization, so that the timescale can only be controlled by C_π and the gaps δ_0 and Δ^+ .

Symmetry of the boundary states. Although the states $\|\pm\>$ are not eigenstates of $\mathcal{H}^{(2)}$ once measurements are included, they retain symmetry-related overlaps with low-energy eigenstates. Let Π_x be a unitary that exchanges the \mathcal{S}_2 -even and -odd sectors,

$$\Pi_x \|\pm\> = \|\mp\>, \quad \Pi_x^2 = \mathbb{I}, \quad (\text{C14})$$

and assume that Π_x pairs eigenstates as

$$\Pi_x \|\Omega_a^+\rangle = \|\Omega_a^-\rangle, \quad \Pi_x \|\psi_b^+\rangle = \|\psi_b^-\rangle, \quad (\text{C15})$$

with identical eigenvalues in each pair. Then

$$\begin{aligned} c_{0,a}^+ &= \langle\langle +\|\Omega_a^+\rangle\rangle = \langle\langle +\|\Pi_x^2 \|\Omega_a^+\rangle\rangle = \langle\langle -\|\Omega_a^-\rangle\rangle = c_{0,a}^-, \\ c_{1,b}^+ &= \langle\langle +\|\psi_b^+\rangle\rangle = \langle\langle +\|\Pi_x^2 \|\psi_b^+\rangle\rangle = \langle\langle -\|\psi_b^-\rangle\rangle = c_{1,b}^-. \end{aligned} \quad (\text{C16})$$

Thus the overlaps entering are $C_0 = 1$ and C_π , which depends on the relative degeneracy of ground and excited states of $\mathcal{H}^{(2)}$ in each symmetry sector.

Relevant gaps and the purification scale. Recalling Eq. (C4) of the main text, the asymptotic form

$$\Theta(t) \sim \frac{e^{-t\delta_0}}{1 + C_\pi e^{-t\Delta^+}} \quad (\text{C17})$$

is defined by the two gaps, δ_0 , the gap between \mathcal{S}_2 sectors, and Δ^+ is the gap to the first excitation within the \mathcal{S}_2 -even sector, both evaluated at zero momentum. The purification timescale is governed by $t_\pi \sim \delta_0^{-1}$. To see this, note that if $\delta_0 > \Delta^+$, the denominator saturates quickly and $\Theta(t)$ decays as $e^{-t\delta_0}$ up to a constant prefactor. In contrast, if $\delta_0 < \Delta^+$, the denominator initially decreases as $e^{-t\Delta^+}$, so $\Theta(t)$ can exhibit a transient increase before ultimately decaying on the longer scale $t_\pi \sim \delta_0^{-1}$.

In all cases, Δ^+ only affects transient behavior and prefactors; the late-time decay, and hence the purification time, is set by the \mathcal{S}_2 -sector gap, δ_0 .

Appendix D: Charge Sharpening/Decohering Timescale

In the main text we argued that the charge-sharpening timescale is controlled by the smallest gap between sectors with nonzero \tilde{Q}_+ charge. In particular, from Eq. (49), we have

$$t_Q \sim \delta_Q^{-1} \log C_Q, \quad \delta_Q \equiv \min_{\tilde{n}_+ > 0} \delta_{\tilde{n}_+}, \quad (\text{D1})$$

where $\delta_{\tilde{n}_+}$ is the gap from the ground state to the lowest state in the sector with $\tilde{Q}_+ = \tilde{n}_+$, and C_Q encodes the (near) degeneracy of low-lying excitations. Here we derive this result more precisely.

We begin by decomposing the identity-boundary state into sectors with fixed \bar{Q}_+ and \tilde{Q}_+ :

$$\|\mathbb{I}^{\otimes 2}\rangle = \sum_{\bar{n}_+, \tilde{n}_+} \|\langle\langle \bar{n}_+, 0, \tilde{n}_+, 0 \rangle\rangle, \quad (\text{D2})$$

where $\|\langle\langle \bar{n}_+, \bar{n}_-, \tilde{n}_+, \tilde{n}_- \rangle\rangle$ projects onto the subspace with $\bar{Q}_\pm = \bar{n}_\pm$ and $\tilde{Q}_\pm = \tilde{n}_\pm$. To obtain a clean notion of a “sharpening time,” we fix the average physical charge sector $\bar{Q}_+ = \bar{n}_+$ (trajectories relax to this sector on a timescale that depends on \bar{n}_+).

Focusing on sharpening of \tilde{Q}_+ (the \tilde{Q}_- case is analogous with a different initial state) and suppressing the fixed indices $\bar{n}_- = \tilde{n}_- = 0$, the \tilde{Q}_+ -resolved variance can be written as

$$\begin{aligned} [\delta \tilde{Q}_+^2(t)]_{\text{id}, \bar{n}_+} &= \frac{\sum_{\tilde{n}_+} \langle\langle \tilde{n}_+ \|\tilde{Q}_+^2 \| \tilde{n}_+(t) \rangle\rangle}{\sum_{\tilde{n}_+} \langle\langle \tilde{n}_+ \|\tilde{n}_+(t) \rangle\rangle} \\ &= \frac{\sum_{\tilde{n}_+} \tilde{n}_+^2 \langle\langle \tilde{n}_+ \|\tilde{n}_+(t) \rangle\rangle}{\sum_{\tilde{n}_+} \langle\langle \tilde{n}_+ \|\tilde{n}_+(t) \rangle\rangle}, \end{aligned} \quad (\text{D3})$$

where $\|\tilde{n}_+(t)\rangle \equiv e^{-t\mathcal{H}^{(2)}} \|\tilde{n}_+\rangle$ and the sum runs over all allowed \tilde{n}_+ in the fixed \bar{n}_+ sector.

Sector decomposition and gaps. Expand each fixed- \tilde{n}_+ state in its eigenbasis:

$$\begin{aligned} e^{-t\mathcal{H}^{(2)}} \|\tilde{n}_+\rangle\rangle &\underset{t \rightarrow \infty}{\approx} c_0^{\tilde{n}+} e^{-\epsilon_0^{\tilde{n}+} t} \|\Omega_{\tilde{n}+}\rangle\rangle \\ &+ c_1^{\tilde{n}+} e^{-(\epsilon_0^{\tilde{n}+} + \Delta^{\tilde{n}+})t} \|e_{\tilde{n}+}^1\rangle\rangle + \dots, \end{aligned} \quad (\text{D4})$$

where $\epsilon_0^{\tilde{n}+}$ is the minimum in the $\tilde{Q}_+ = \tilde{n}_+$ sector, $\Delta^{\tilde{n}+}$ is the intra-sector gap to its first excitation, and $c_0^{\tilde{n}+}$ and

$c_1^{\tilde{n}+}$ are overlap amplitudes. Since the exact ground state lies in the $\tilde{Q}_+ = 0$ sector, we define the inter-sector gaps

$$\delta_{\tilde{n}+} \equiv \epsilon_0^{\tilde{n}+} - \epsilon_0^0, \quad \delta_Q \equiv \min_{\tilde{n}_+ > 0} \delta_{\tilde{n}+}. \quad (\text{D5})$$

Let \tilde{n}_+^* denote a sector attaining this minimum, $\delta_Q = \delta_{\tilde{n}_+^*}$. We now show that only $\delta_{\tilde{n}_+^*}$ and the symmetric-sector gap $\Delta_0 \equiv \Delta^{\tilde{n}_+^*=0}$ control the late-time behavior, and derive Eq. (49).

Using the above expansion, the resolved variance becomes

$$\begin{aligned} [\delta\tilde{Q}_+^2(t)]_{\tilde{n}+} &\underset{t \rightarrow \infty}{\approx} \frac{\sum_{\tilde{n}+} \tilde{n}_+^2 (|c_0^{\tilde{n}+}|^2 + |c_1^{\tilde{n}+}|^2 e^{-\Delta_{\tilde{n}+} t}) e^{-\epsilon_0^{\tilde{n}+} t}}{\sum_{\tilde{n}+} (|c_0^{\tilde{n}+}|^2 + |c_1^{\tilde{n}+}|^2 e^{-\Delta_{\tilde{n}+} t}) e^{-\epsilon_0^{\tilde{n}+} t}} \\ &= \frac{\sum_{\tilde{n}_+ > 0} \tilde{n}_+^2 (|c_0^{\tilde{n}+}|^2 + |c_1^{\tilde{n}+}|^2 e^{-\Delta_{\tilde{n}+} t}) e^{-\delta_{\tilde{n}+} t}}{|c_0^0|^2 + |c_1^0|^2 e^{-\Delta_0 t} + \sum_{\tilde{n}_+ > 0} (|c_0^{\tilde{n}+}|^2 + |c_1^{\tilde{n}+}|^2 e^{-\Delta_{\tilde{n}+} t}) e^{-\delta_{\tilde{n}+} t}}. \end{aligned} \quad (\text{D6})$$

At late times, the sum is dominated by the sector \tilde{n}_+^* with the smallest gap $\delta_{\tilde{n}_+^*}$. Neglecting sectors with larger $\delta_{\tilde{n}_+}$ and subleading excited states in other sectors, we obtain

$$[\delta\tilde{Q}_+^2(t)]_{\tilde{n}+} \approx \frac{(\tilde{n}_+^*)^2 |c_0^{\tilde{n}+*}|^2}{|c_0^0|^2} \frac{e^{-\delta_{\tilde{n}_+^*} t}}{1 + \frac{|c_0^0|^2}{|c_0^0|^2} e^{-\Delta_0 t} + \frac{|c_0^{\tilde{n}+*}|^2}{|c_0^0|^2} e^{-\delta_{\tilde{n}_+^*} t}}. \quad (\text{D7})$$

Thus only $\delta_{\tilde{n}_+^*}$ and Δ_0 remain at asymptotically relevant scales.

Case 1: $\Delta_0 \gg \delta_{\tilde{n}_+^}$.* This is typical of the SSB/QLRO regime, where $\delta_{\tilde{n}_+^*} \rightarrow 0$ as $L \rightarrow \infty$. The $e^{-\Delta_0 t}$ term dies off rapidly on the timescale set by $\delta_{\tilde{n}_+^*}^{-1}$, yielding

$$[\delta\tilde{Q}_+^2(t)]_{\tilde{n}+} \underset{t \rightarrow \infty}{\sim} (\tilde{n}_+^*)^2 C_\delta \frac{e^{-\delta_{\tilde{n}_+^*} t}}{1 + C_\delta e^{-\delta_{\tilde{n}_+^*} t}}, \quad (\text{D8})$$

which matches Eq. (49) with $C_Q = C_\delta$. A naive estimate is $C_\delta \approx |c_0^{\tilde{n}+*}|^2 / |c_0^0|^2$, but at times $t \sim \delta_{\tilde{n}_+^*}^{-1}$ one must also include excited states within the \tilde{n}_+^* sector whose splittings satisfy $\Delta_{\tilde{n}_+^*}^a \lesssim \delta_{\tilde{n}_+^*}$. Writing these excitations as

$$\|e_{\tilde{n}_+^*}^a\rangle\rangle, \quad \epsilon_{\tilde{n}_+^*}^a - \epsilon_0^0 \equiv \Delta_{\tilde{n}_+^*}^a, \quad (\text{D9})$$

we obtain

$$C_\delta \approx \frac{|c_0^{\tilde{n}+*}|^2}{|c_0^0|^2} + \sum_a \frac{|c_a^{\tilde{n}+*}|^2}{|c_0^0|^2} e^{-\Delta_{\tilde{n}_+^*}^a / \delta_{\tilde{n}_+^*}}. \quad (\text{D10})$$

In the SSB phase, $\delta_{\tilde{n}_+^*} \rightarrow 0$ while the number of tower-of-states levels within an $O(\delta_{\tilde{n}_+^*})$ window remains $O(1)$, so $C_Q \sim O(1)$.

In the symmetric phase of a translation-invariant system, $\delta_{\tilde{n}_+^*}$ remains $O(1)$ and there are typically $O(V)$ modes within an $O(1)$ window above the band minimum for a system of $V = L^D$. This makes C_Q polynomial in L . As a simple illustration, consider the 1D ground state $|\Omega_{\tilde{n}_+^*}\rangle$ in the \tilde{n}_+^* sector. One can form $O(L)$ orthogonal states with energies within a constant window by momentum superpositions

$$|\tilde{k}_{\tilde{n}_+^*}\rangle = \sum_x \tilde{q}_{+,x} e^{ikx} |\Omega_{\tilde{n}_+^*}\rangle. \quad (\text{D11})$$

For a translation-invariant ground state, the $k=0$ mode reduces to $|\Omega_{\tilde{n}_+^*}\rangle$, while small- k modes provide quasi-degenerate excitations within that window.

Case 2: $\Delta_0 \ll \delta_{\tilde{n}_+^}$.* Here the $e^{-\Delta_0 t}$ term remains approximately constant on the $t \sim \delta_{\tilde{n}_+^*}^{-1}$ timescale. Writing

$$C_\Delta \equiv \frac{|c_1^0|^2}{|c_0^0|^2} + \sum_a \frac{|c_a^0|^2}{|c_0^0|^2} e^{-\Delta_0^a / \delta_{\tilde{n}_+^*}}, \quad (\text{D12})$$

we obtain

$$\begin{aligned} [\delta\tilde{Q}_+^2]_{\tilde{n}+}(t) &\underset{t \rightarrow \infty}{\sim} (\tilde{n}_+^*)^2 C_\delta \frac{e^{-\delta_{\tilde{n}_+^*} t}}{1 + C_\Delta + C_\delta e^{-\delta_{\tilde{n}_+^*} t}} \\ &= (\tilde{n}_+^*)^2 \frac{C_\delta}{1 + C_\Delta} \frac{e^{-\delta_{\tilde{n}_+^*} t}}{1 + \frac{C_\delta}{1 + C_\Delta} e^{-\delta_{\tilde{n}_+^*} t}}. \end{aligned} \quad (\text{D13})$$

Absent additional SSB, there are no Goldstone modes in this sector and C_Δ remains finite, so $C_Q = C_\delta / (1 + C_\Delta)$ is again $O(1)$ or, at most, polynomial in L .

Combining both cases, we obtain the scaling quoted in

the main text:

$$t_Q \sim \delta_Q^{-1} \log C_Q \sim \begin{cases} \mathcal{O}(V), & \text{SSB/QLRO phase} \\ \mathcal{O}(\log V), & \text{symmetric phase,} \end{cases} \quad (\text{D14})$$

where $V = L^D$ for the spatial dimension, D , and we used $\delta_Q \sim V^{-1}$, $C_Q = \mathcal{O}(1)$ in the SSB/QLRO phase, and $\delta_Q = \mathcal{O}(1)$, $\log C_Q \sim \log V$ in the symmetric phase.

Dynamical upper bound at large measurement rate. A simple dynamical argument yields $t_Q \sim (\log L)/\Gamma_p$ at large measurement rate in 1D, consistent with the static gap analysis. In the limit of vanishing unitary evolution, charges are immobile; sharpening occurs once *all* sites have been measured at least once. If $N(t)$ sites have been measured by time t , then

$$\frac{dN}{dt} = \Gamma_p (L - N), \quad (\text{D15})$$

with solution $N(t) = L(1 - e^{-\Gamma_p t})$ for $N(0) = 0$. Requiring $N(t) \geq L-1$ gives $t_Q^* \sim \Gamma_p^{-1} \log L$.

An analogous estimate applies to discrete symmetries (e.g., a global parity): one learns the global charge once parities of a collection of disjoint subintervals covering the system have been measured. Since measuring all sites takes $\mathcal{O}(\log L)$ time, the same bound $t_Q \sim \Gamma_p^{-1} \log L$ follows.

Charge Decohering Timescale We now derive the charge-decoherence timescale from the charge variance element $[\delta \tilde{Q}_-^2]_{\text{sw}}$. This derivation follows directly from the charge-variance analysis above under the exchange $\tilde{Q}_+ \leftrightarrow \tilde{Q}_-$ and $\|\mathbb{I}^{\otimes 2}\rangle \leftrightarrow \|\text{SW}\rangle$. The SWAP boundary is convenient because

$$\|\text{SW}\rangle = \sum_{\bar{n}_+, \bar{n}_-} \|(\bar{n}_+, 0, 0, \bar{n}_-)\rangle, \quad (\text{D16})$$

which mirrors the decomposition of $\|\mathbb{I}^{\otimes 2}\rangle$ with $\tilde{n}_+ \leftrightarrow \tilde{n}_-$. The resulting decoherence timescale is identical in structure to the charge-sharpening time derived:

$$\overline{[\delta \Phi_Q^2(t)]} \underset{t \rightarrow \infty}{\approx} \frac{C_\Phi e^{-\delta_\Phi t}}{1 + C_\Phi e^{-\delta_\Phi t}}, \quad (\text{D17})$$

with the timescale depending on the degeneracy C_Φ in the same manner

$$t_\Phi \sim \delta_\Phi^{-1} \log C_\Phi \sim \begin{cases} \mathcal{O}(V), & \text{SSB/QLRO phase} \\ \mathcal{O}(\log V), & \text{symmetric phase,} \end{cases} \quad (\text{D18})$$

Appendix E: Steady-State Variance

We derive the steady-state, trajectory-resolved subsystem charge variance and charge coherence. After the dynamics have relaxed into a fixed global charge sector,

these quantities diagnose the residual diagonal and off-diagonal charge fluctuations inside a subregion A . In the replicated description used in the main text, both reduce to ground-state fluctuations of inter-replica charges, \tilde{Q}_\pm restricted to A in the zero charge sector.

1. Subsystem charge variance

In the main text, we describe how the subsystem variance is can be computed from the two-point correlation function of the \tilde{Q}_+ charge:

$$\begin{aligned} [\delta Q^2]_A &= [\tilde{Q}_{+,A}^2]_{\text{id}} = \sum_{i,j \in A} [\tilde{q}_{+,i} \tilde{q}_{+,j}]_{\text{id}} \quad (\text{E1}) \\ &= \sum_{i,j \in A} [c_{zz}^{(+)}(i-j)]_{\text{id}}, \end{aligned}$$

where $c_{zz}^{(+)}(|i-j|)$ is the connected ZZ correlation function. Moving forward, we will drop the $[\dots]_{\text{id}}$ notation (See Eq. (43)), implicitly assuming the correct matrix element is being calculated. We want to express this sum in a way that we can extract the scaling as a function of the system size, $|A|$ and/or its boundary, $|\partial A|$.

In the continuum, we can express this sum as:

$$[\delta Q^2]_A \approx \int_A d^D x \int_A d^D y c_{zz}^{(+)}(x-y) \quad (\text{E2})$$

$$= \int_V d^D u c_{zz}^{(+)}(u) V_{\cap}(u), \quad (\text{E3})$$

where we have defined the integral in terms of a separation, $u = x - y$, and defined the volume overlap as

$$V_{\cap}(u) \equiv \int_V d^D x \chi_A(x) \chi_A(x+u). \quad (\text{E4})$$

and we have introduced the indicator function: $\chi_A(x) = 1$ if $x \in A$, and $\chi_A(x) = 0$ otherwise. Now, we want to consider how this volume overlap behaves as a function of u . Because we expect $c_{zz}^{(+)}(u)$ to decay faster than $1/u$, we also focus on its behavior for u much smaller than the linear subsystem size, $L_A = |A|^{1/d}$. For regions A with smooth boundary, $V_{\cap}(u)$ admits a small-displacement expansion ($|u| \ll L_A$)

$$V_{\cap}(u) = |A| - \kappa_D |\partial A| |u| + \mathcal{O}\left(|\partial A| \frac{|u|^2}{L_A}\right), \quad (\text{E5})$$

where $\kappa_D = \mathcal{O}(1)$ is a geometric constant. This will produce one volume law and one area law component (plus subleading factors). The volume law component will vanish due to the charge constraint on the steady state ($\tilde{Q}_+ = 0$):

$$|A| \int_V d^D u c_{zz}^{(+)}(u) = |A| [\tilde{Q}_+]_{\text{id}} = 0. \quad (\text{E6})$$

Thus, we focus on the area law component,

$$[\delta Q^2]_A \approx -\kappa_D |\partial A| \int_V d^D u(u) c_{zz}^{(+)}(u), \quad (\text{E7})$$

plus subleading terms from $\mathcal{O}(|u|^2/L_A)$. To perform this integral, we first note that, for bounded A of linear size L_A , it follows that $V_\cap(u) = 0$ for $|u| \gtrsim L_A$, so even though the integral is being carried out over the whole system, it is only supported for $|u| \lesssim \mathcal{O}(L_A)$.

From here, we can derive the scaling of the subsystem charge variance directly from the long-distance forms of $c_{zz}^{(+)}(u)$ in the different phases. Since $V_\cap(u)$ is bounded as described above, we only need to perform the integral over the region where $|u| \lesssim \mathcal{O}(L_A)$.

In the sharp phase, the inter-replica \tilde{Q}_+ modes are gapped, $c_{zz}^{(+)}(u) \sim e^{-|u|/\xi_+}$ at large $|u|$, and the integral in Eq. (E7) converges, giving $[\delta Q^2]_A \sim |\partial A|$. One can quickly verify that including higher-order terms will only modify the $\mathcal{O}(1)$ coefficient of this area-law term.

In the fuzzy/coherent phases, the SSB structure of the replicated theory supports linearly dispersing modes for \tilde{Q}_+ , as seen in Refs. [13, 14]. As a consequence, the structure factor: $S_{zz}^{(+)}(k) \equiv \int dr e^{-ik \cdot u} c_{zz}^{(+)}(u) = [\tilde{q}_+(k)\tilde{q}_+(-k)]$ is non-analytic at small k : $S_{zz}^{(+)}(k) \sim |k|$ as $k \rightarrow 0$ [65]. In real space, for an isotropic system, this implies

$$c_{zz}^{(+)}(u) \sim \frac{1}{|u|^{D+1}}. \quad (\text{E8})$$

Inserting this into (E7) yields a logarithmic cut off at $|u| \sim L_A$:

$$[\delta Q^2]_A \sim |\partial A| \log L_A \sim |\partial A| \log |A|. \quad (\text{E9})$$

Including higher-order terms here will only produce sub-leading boundary terms $\mathcal{O}(L_A^{-n})$.

Thus, we arrive at the scalings seen in the main text:

$$[\delta Q^2]_A \sim \begin{cases} |\partial A| \log |A|, & (\text{fuzzy/coherent}), \\ |\partial A|, & (\text{sharp}). \end{cases} \quad (\text{E10})$$

For purely unitary U(1)-symmetric dynamics within a fixed charge sector, we can actually calculate the charge variance of a subregion directly. Random unitary dynamics have a steady state of the maximally mixed state.

This state is particularly nice because all states are exchangeable (i.e. the correlations between points x and y only depend on whether they are the same or different). Because of this, we can write out the sum for the charge variance in a charge sector, $Q = N$, and see it gives us a volume law. Let's assume a spin- $\frac{1}{2}$ system for convenience, or equivalently $q = \{0, 1\}$:

$$\begin{aligned} [\delta Q^2]_A &= \sum_{ij \in A} \langle q_i q_j \rangle - \langle q_i \rangle \langle q_j \rangle \\ &= |A| \langle q_i^2 \rangle + |A|(|A| - 1) \langle q_i q_{j \neq i} \rangle - |A| \langle q_i \rangle^2, \end{aligned} \quad (\text{E11})$$

where $\langle q_i q_{j \neq i} \rangle$ is the correlation between any distinct points. $\langle q_i \rangle = \frac{N}{V} = n$, trivially. And similarly $\langle q_i^2 \rangle = n$. Finally, $\langle q_i q_{j \neq i} \rangle$ is just given by the probability that both points are occupied, so $\langle q_i q_{j \neq i} \rangle = \frac{N(N-1)}{V(V-1)}$. Thus:

$$[\delta Q_A^2] = |A|n(1-n|A|) + |A|(|A|-1) \left(\frac{N(N-1)}{V(V-1)} \right) \quad (\text{E12})$$

$$\begin{aligned} &= |A|n \left(\frac{(V-|A|)(V-N)}{V(V-1)} \right) \\ &\underset{V, |A| \rightarrow \infty}{\approx} n(1-n)|A|(1-|A|/V) \underset{V \gg |A|}{\approx} n(1-n)|A|. \end{aligned} \quad (\text{E13})$$

Alternatively, we could have noted the form of the two point correlation from above:

$$[\tilde{q}_{+,i}\tilde{q}_{+,j}]_{\text{id}} = \langle q_i q_j \rangle_c = \begin{cases} -n(1-n) & (i=j) \\ n(1-n)/V & (\text{else}). \end{cases} \quad (\text{E14})$$

In other words, connected correlator is $c_{zz}^{(+)}(u) = n(1-n)(\frac{1}{V} - \delta(u))$, for some charge density, n . And if we plug this into Eq. (E3), we obtain

$$\begin{aligned} [\delta Q_A^2] &= [\delta \tilde{Q}_{+,A}^2] = n(1-n) \left(\frac{|A|^2}{V} - |A| \right) \\ &\underset{V \gg |A|}{\approx} n(1-n)|A| \end{aligned} \quad (\text{E15})$$

Note that we cannot plug this correlator into Eq. (E7), as the derivation for this relied on the correlator being analytic so that we could perform expansions for small u .

Additionally, we could have guessed this form by noting that the small- k structure factor is constant for the maximally mixed state: $S(k) = \chi$, and the $\tilde{Q}_+ = 0$ constraint simply removes the $k = 0$ mode. Translating this into a real-space correlation function just produces the same delta function minus a vanishing constant: $c_{zz}^{(+)}(u) = \chi(\delta(u) - \frac{1}{V})$

Importantly, for any finite measurement rate, the correlator will no longer be a delta function, and will analytically decay instead. And, as explained in the earlier derivation, with an analytically decaying correlator, the fixed charge constraint eliminates the volume law contribution present in the case of pure unitary dynamics.

2. Subsystem charge coherence

The trajectory-resolved “charge coherence” variance can be written as

$$[\delta \Phi_Q^2]_A = \sum_{i,j \in A} \frac{\langle \text{SW} \| \tilde{q}_{-,i} \tilde{q}_{-,j} \| \rho^{(2)} \rangle}{\langle \text{SW} \| \rho^{(2)} \rangle} = \sum_{i,j \in A} c_{zz}^{(-)}(i-j), \quad (\text{E16})$$

where $c_{zz}^{(-)}$ is the connected correlator of the inter-replica diagonal charge $\tilde{q}_{-,i}$. Repeating the steps above gives the same exact k -space form

$$[\delta\Phi_Q^2]_A = \frac{1}{V} \sum_k S_{zz}^{(-)}(k) |\chi_A(k)|^2, \quad (\text{E17})$$

with $S_{zz}^{(-)}(0) = 0$ in the corresponding zero charge sector, and thus, yielding the same scaling logic. In the coherent phase, \tilde{Q}_\pm are related by the \mathcal{S}_2 exchange symmetry and one expects $S_{zz}^{(-)}(k) \sim |k|$ and thus $c_{zz}^{(-)}(u) \sim |u|^{-(D+1)}$; whereas in the incoherent phase, $c_{zz}^{(-)}(u)$ decays exponentially and

$$[\delta Q^2]_A \sim \begin{cases} |\partial A| \log |A|, & (\text{fuzzy/coherent}), \\ |\partial A|, & (\text{sharp}). \end{cases} \quad (\text{E18})$$

Appendix F: n-copy Charges and Correlators

In the main text, we quoted the steady-state forms of the SW-SSB and SSB correlators evaluated with specific boundary conditions for $n = 2$. Here we derive these expressions for general n and discuss the replica limit ($n \rightarrow 1$).

Multi-copy operators. For n replicas (for even n), we define n -copy generalizations of the diagonal and (off)-diagonal, and inter-replica charges

$$\begin{aligned} \tilde{Q}_+^{(n)} &\equiv \sum_{a=1}^n (-1)^a (Q_{aL} + Q_{aR}), \\ \tilde{Q}_-^{(n)} &\equiv \sum_a (-1)^a (Q_{aL} - Q_{aR}). \end{aligned} \quad (\text{F1})$$

And the generalization of the off-diagonal and inter-replica fluctuations take the form

$$\begin{aligned} \mathcal{C}_{ij}^{(+),n} &\equiv \sum_{a=1}^n \left(S_{i,aL}^+ S_{j,aL}^- S_{i,aR}^+ S_{j,aR}^- + \text{h.c.} \right), \\ \mathcal{C}_{ij}^{(-),n} &\equiv \sum_{\substack{a \text{ even} \\ b \text{ odd}}} \left(S_{i,aL}^+ S_{j,aL}^- S_{i,bL}^- S_{j,bL}^+ + \text{h.c.} \right), \end{aligned} \quad (\text{F2})$$

where a, b label replicas, and L/R indicate the two legs of the Choi space. The operators $\mathcal{C}_{ij}^{(+),n}$ and $\mathcal{C}_{ij}^{(-),n}$ detect diagonal and inter-replica order,

Boundary conditions and trajectory representation. Using the same boundary conditions as in the main text generalized for $n > 1$ and evaluating similar

diagrams, the charge variance elements are

$$\begin{aligned} [(\delta\tilde{Q}_-^{(n)})^2]_\tau &= \frac{\langle\langle \mathcal{T}^{r,(n)} \| (\tilde{Q}_-^{(n)})^2 \| \rho^{(n)} \rangle\rangle}{\langle\langle \mathcal{T}^{r,(n)} \| \rho^{(n)} \rangle\rangle} \\ &= \frac{\mathbb{E}_{\mathbf{m}}^{(n)} [\text{Tr} ([\text{ad}_{\rho_{\mathbf{m}}}^{n/2} Q_A]^\dagger [\text{ad}_{\rho_{\mathbf{m}}}^{n/2} Q_A])]}{\mathbb{E}_{\mathbf{m}}^{(n)} [\text{Tr} [\rho_{\mathbf{m}}^n]]}, \quad (\text{F3}) \\ [(\delta\tilde{Q}_+^{(n)})^2]_{\text{id}} &= \frac{\langle\langle \mathbb{I}^{\otimes n} \| (\tilde{Q}_+^{(n)})^2 \| \rho^{(n)} \rangle\rangle}{\langle\langle \mathbb{I}^{\otimes n} \| \rho^{(n)} \rangle\rangle} \\ &= \mathbb{E}_{\mathbf{m}}^{(2)} \left[(\text{Tr} [\rho_{\mathbf{m}} Q^2] - \text{Tr} [\rho_{\mathbf{m}} Q]^2) \text{Tr} [\rho_{\mathbf{m}}]^{n-2} \right], \end{aligned}$$

where where $\mathcal{T}^{r,(n)}$ is the cyclic permutation operator defined in Eq. (30), and we have maintained factors of $\text{Tr}[\rho_{\mathbf{m}}]$ in the numerator, and $\text{ad}_x(y) = [x, y]$, so that $\text{ad}_x^2(y) = [x, [x, y]]$.

The steady-state correlators for a typical trajectory can be written as

$$\begin{aligned} [\mathcal{C}_{ij}^{(+)}]_{\mathcal{T}}^{(n)} &= \frac{\langle\langle \mathcal{T}^{r,(n)} \| \mathcal{C}_{ij}^{(+),n} \| \rho^{(n)} \rangle\rangle}{\langle\langle \mathcal{T}^{r,(n)} \| \rho^{(n)} \rangle\rangle} \\ &= \frac{\mathbb{E}_{\mathbf{m}}^{(2)} [\text{Tr} [\rho_{\mathbf{m}}^{n-1} S_i^+ S_j^- \rho_{\mathbf{m}} S_i^- S_j^+]]}{\mathbb{E}_{\mathbf{m}}^{(2)} [\text{Tr} [\rho_{\mathbf{m}}^n]]}, \quad (\text{F4}) \\ [\mathcal{C}_{ij}^{(-)}]_{\text{id}}^{(n)} &= \frac{\langle\langle \mathbb{I}^{\otimes n} \| \mathcal{C}_{ij}^{(-),n} \| \rho^{(n)} \rangle\rangle}{\langle\langle \mathbb{I}^{\otimes n} \| \rho^{(n)} \rangle\rangle} \\ &= \mathbb{E}_{\mathbf{m}}^{(2)} \left[\text{Tr} [\rho_{\mathbf{m}} S_i^+ S_j^-] \text{Tr} [\rho_{\mathbf{m}} S_i^- S_j^+] \text{Tr} [\rho_{\mathbf{m}}]^{n-2} \right], \end{aligned}$$

where the reduced operators $\mathcal{C}_{ij}^{(\pm)}$ are the $n = 2$ versions used in the main text.

Replica limit.

As is clear from the above formulas, the diagonal charge variance element (physical charge variance) and inter-replica correlator (EA correlation function) are the same for all replica indices. However, the off-diagonal charge variance element (charge coherence) and the diagonal correlators are more subtle. The latter likely has a limit resembling the fidelity correlator or the more recent Rényi-1 correlator [66].

Below, we discuss the limit for the charge coherence. In the main text, we quoted that

$$[\delta\Phi_Q^2] \equiv \lim_{n \rightarrow 1} [(\delta\tilde{Q}_-^{(n)})^2]_\tau = \text{Tr} \left[\left| [\rho, Q] \right| \right] \quad (\text{F5})$$

To see this, we note that we can treat the adjoint action $, \text{ad}_{\rho_{\mathbf{m}}}[\cdot]$ as a superoperator whose action performs the commutation with $\rho_{\mathbf{m}}$. This action on hermitian operators produces anti-hermitian operators and vice versa, so that the joint action $\text{ad}_{\rho}[\cdot](\text{ad}_{\rho}[\cdot])^\dagger$ will always produce a positive-semidefinite hermitian operator. Given this, we may confidently define $\sqrt{\text{ad}_{\rho}[\cdot](\text{ad}_{\rho}[\cdot])^\dagger}$ for a branch of the square root function.

Appendix G: Entanglement Transition: Mean-Field and Replica Limit

Here we derive the critical measurement rate for the entanglement transition within the mean-field (MF) variational model of the main text. We first treat $n = 2$ replicas, in direct parallel with the main discussion, and then take the full replica limit $n \rightarrow 1$. For simplicity, we focus on the all-charge-measurement regime ($r = 0$), so that $\beta = 0$.

We construct an MF state from two replica sectors at each site: a replica-symmetric sector and a minimally replica-asymmetric sector. For n replicas (so $2n$ spins in the doubled Hilbert space), define

$$|\theta_0, \phi_0\rangle = \cos \frac{\theta_0}{2} |\uparrow\rangle^{\otimes 2n} + \sin \frac{\theta_0}{2} |\downarrow\rangle^{\otimes 2n}, \quad (\text{G1})$$

$$|\theta_1, \phi_1\rangle = \cos \frac{\theta_1}{2} |\uparrow\rangle^{\otimes 2} |\downarrow\rangle^{\otimes 2(n-1)} + \sin \frac{\theta_1}{2} |\downarrow\rangle^{\otimes 2} |\uparrow\rangle^{\otimes 2(n-1)}. \quad (\text{G2})$$

A fully symmetric construction would sum over all $n!$ replica permutations, but to capture the entanglement transition it suffices to couple at least two permutation configurations. Our MF ansatz is the uniform product over sites of a two-component superposition,

$$\|\rho_{\text{MF}}^{\otimes n}\rangle = \bigotimes_{i=1}^L \left(\cos \alpha |\theta_0, \phi_0\rangle + \sin \alpha |\theta_1, \phi_1\rangle \right), \quad (\text{G3})$$

where we have taken $\alpha_i \equiv \alpha$ and $(\theta_{0,i}, \phi_{0,i}) \equiv (\theta_0, \phi_0), (\theta_{1,i}, \phi_{1,i}) \equiv (\theta_1, \phi_1)$ to be site-independent.

For $r = 0$, the measurement contribution to the effective Hamiltonian gives a simple MF term

$$E_M = -\Gamma_p L \cos^2 \alpha, \quad (\text{G4})$$

so that the replica-symmetric sector ($\alpha = 0$) is favored at large Γ_p . Local z -type unitary terms ($h_i^z = \sigma_i^z$, $h_i^{zz} = \sigma_i^z \sigma_{i+1}^z$) annihilate the ansatz. The hopping term $h_i^{+-} = \sigma_i^+ \sigma_{i+1}^- + \text{h.c.}$ produces (up to an additive constant)

$$\begin{aligned} E_U = & -4Jn (\cos^4 \alpha \cos^2 \theta_0 + \sin^4 \alpha \cos^2 \theta_1) \\ & - 2J \sin^2(2\alpha)(n-2) \cos^2 \left(\frac{\theta_0 + \theta_1}{2} \right) \\ & - 4J \sin^2(2\alpha) \left(1 + \sin \theta_0 \sin \theta_1 \cos(\phi_1 - \phi_0) \right), \end{aligned} \quad (\text{G5})$$

where the first two lines arise from the $2n$ quadratic pieces $(h_i^{+-})^2 = 2(\mathbb{I} - \sigma_i^z \sigma_{i+1}^z)$, and the last line from the single nontrivial cross term $-2 h_i^{+-} \otimes h_i^{+-}$.

Two-copy mean field: $n = 2$

For $n = 2$, the quadratic term proportional to $(n-2)$ vanishes, and the MF energy per site becomes

$$\begin{aligned} E_{\text{MF}} = & -\Gamma_p \cos^2 \alpha - 8J (\cos^4 \alpha \cos^2 \theta_0 + \sin^4 \alpha \cos^2 \theta_1) \\ & - 4J \sin^2(2\alpha) [1 + \sin \theta_0 \sin \theta_1 \cos(\phi_0 - \phi_1)]. \end{aligned} \quad (\text{G6})$$

We minimize at fixed charge density $\bar{n}_+ = \cos \theta_0$, and fixed ϕ_0 . At half filling ($\theta_0 = \pi/2$), the optimal MF parameters are

- for $\Gamma_p < \Gamma_\pi$,

$$\cos(2\alpha) = \frac{\Gamma_p}{32J}, \quad \theta_1 = \frac{\pi}{2}, \quad \phi_1 = \phi_0, \quad (\text{G7})$$

corresponding to a finite weight in the replica-asymmetric sector;

- for $\Gamma_p > \Gamma_\pi$, the minimum is the replica-symmetric state with $\alpha = 0$.

The transition occurs when $\cos(2\alpha) \rightarrow 1$, yielding

$$\Gamma_\pi = 32J \quad (n = 2, \theta_0 = \frac{\pi}{2}). \quad (\text{G8})$$

Replica limit: $n \rightarrow 1$

Taking the replica limit $n \rightarrow 1$ in E_U gives the MF energy per site

$$\begin{aligned} E_{\text{MF}} = & -\Gamma_p \cos^2 \alpha - 4J (\cos^4 \alpha \cos^2 \theta_0 + \sin^4 \alpha \cos^2 \theta_1) \\ & + 2J \sin^2(2\alpha) \cos^2 \left(\frac{\theta_0 + \theta_1}{2} \right) \\ & - 4J \sin^2(2\alpha) \left(1 + \sin \theta_0 \sin \theta_1 \cos(\phi_1 - \phi_0) \right). \end{aligned} \quad (\text{G9})$$

In the large-measurement regime $\Gamma_p \gg J$, the minimum is the replica-symmetric configuration

$$\alpha = 0, \quad E_{\text{MF}} = -\Gamma_p - 4J \cos^2 \theta_0. \quad (\text{G10})$$

In the opposite regime $\Gamma_p \ll J$, the energy is minimized by vanishing inter-replica charge, $\theta_1 = \pi/2$, and locked phases, $\phi_1 = \phi_0$, so that only the mixing angle α remains variational. The MF minimum then occurs at a finite replica-asymmetric weight satisfying

$$\cos(2\alpha_c) = \frac{\frac{\Gamma_p}{4J} + \cos^2 \theta_0}{2(1 + \sin \theta_0)^2 + \cos^2 \theta_0}. \quad (\text{G11})$$

This expression holds until $\cos(2\alpha_c) \rightarrow 1$, beyond which the minimum is pinned at $\alpha = 0$. The resulting mean-field critical measurement rate for the entanglement transition is

$$\Gamma_\pi = 8J(1 + \sin \theta_0)^2. \quad (\text{G12})$$

At half filling ($\theta_0 = \pi/2$) this reduces to $\Gamma_\pi = 32J$, in agreement with the $n = 2$ result above.

If one instead fixes $\theta_1 = \theta_0$ and only varies α , the MF minimization yields a critical scale

$$\Gamma_\pi = 32J \sin^2 \theta_0, \quad (\text{G13})$$

consistent with the charge-sharpening rate derived in Ref. [14]. However, this restricted ansatz produces an incorrect MF ground state in which the inter-replica charge acquires an unphysical finite expectation proportional to $\cos^2 \theta_0$. Allowing θ_1 to relax to $\pi/2$ both lowers the energy and correctly suppresses the inter-replica charge in the entangled phase.

Appendix H: Gutzwiller-Jastrow variational projection

In the main text, we discussed applying a Gutzwiller-Jastrow term to the mean field state that had a fixed XY order given by constant $\phi_{0,\pm 1}$ for the spin- $\frac{1}{2}$ states $|\theta_{0,\pm 1}, \phi_{0,\pm 1}\rangle_i$. Below, we discuss the term needed to alter the order in the \tilde{Q}_\pm charges represented by states with $|\pm 1\rangle$ in the spin-1 sector.

A standard Jastrow acting on the $|\pm 1\rangle$ sectors is $P_{GW} = \exp\left\{\left[-\sum_{r=1}^L g(r)(S_i^z S_{i+r}^z)^2 \otimes \sigma_i^z \sigma_{i+r}^z\right]\right\}$, which suppresses spin alignment in the spin- $\frac{1}{2}$ space for $|\pm 1\rangle$ configurations in the spin-1 space. Now, this can be expanded so that

$$P_{GW} = \prod_{r=1}^L \left[\mathbb{I} - (S_i^z S_{i+r}^z)^2 \otimes \left(\sinh g(r) \sigma_i^z \sigma_{i+r}^z + (1 - \cosh g(r)) \mathbb{I} \right) \right]. \quad (\text{H1})$$

This form poses an issue for our ansatz, however, as it will exponentially re-weight the $|\pm 1\rangle$ sectors relative to the $|0\rangle$ sector. To mitigate this, we alter the $\cosh g(r)$ term, adding a contribution to the $|0\rangle$ sector, $(\cosh g(r) - 1)(\mathbb{I} - (S_i^z S_{i+r}^z)^2)$ so that it also re-weights the $|0\rangle$ sector by a factor that scales in the same manner as the $|\pm 1\rangle$ sectors:

$$P'_{GW} = \prod_{r=1}^L \left[(\cosh g(r)) \mathbb{I} - (\sinh g(r)) (S_i^z S_{i+r}^z)^2 \otimes \sigma_i^z \sigma_{i+r}^z \right] \quad (\text{H2})$$

This manifestly does not change the action of the projector on the $|\pm 1\rangle$ sector. In this form, divide by the overall constant factor $\prod_{r=1}^L (\cosh g(r))$ to obtain the form in the main text.

$$P'_{GW} \propto \prod_{r=1}^L \left[\mathbb{I} - (\tanh g(r)) (S_i^z S_{i+r}^z)^2 \otimes \sigma_i^z \sigma_{i+r}^z \right] \quad (\text{H3})$$

With a special choice of initial state and coefficients, $g(r)$, we can ensure our ansatz includes states with the appropriate short-range correlations and gapped physics vs QLRO and TOS scalings in a computationally accessible manner. For the moment, let us focus on the effect in the $|+1\rangle$ sector, since the story will be identical for the $| -1\rangle$ sector. Here, the uniform ϕ_\pm spin- $\frac{1}{2}$ state $|\psi_0\rangle = |+\rangle^{\otimes L}$ is special because it is a uniform superposition of all z-configurations, $s_i = \pm \frac{1}{2}$, so that

$$\Psi(\{s_i\}) \equiv \langle \{s_i\} | P'_{GW}(g(r)) | \psi_0 \rangle \sim e^{-\sum_{i < j} g(|j-i|) s_i s_j}. \quad (\text{H4})$$

Expectation of the state with the Jastrow factor then become a classical partition function:

$$\mathcal{Z} = \sum_{\{s_i\}} |\Psi(\{s_i\})|^2 \sim \sum_{\{s_i\}} e^{-2 \sum_{i < j} g(|j-i|) s_i s_j}. \quad (\text{H5})$$

This is nothing more than a long-range 1D classical Ising model at $T = 1$ with coefficients $2g(r)$. If these couplings are short range (i.e. $g(r=1) \gg g(r \geq 2) \approx 0$), then this Ising model is disordered for all finite temperatures, so that $c_{zz}^{(\pm)}(r)$ and $\mathcal{C}^{(\pm)}(r)$ will decay exponentially. In contrast, the long range ising model with $g(r) \sim 1/r^2$ is known to support finite-temperature phase transition and admits a Coulomb-gas / KT-type description in terms of domain walls (kinks) interacting logarithmically, with $1/r^2$ two point charge correlations in the low-temperature phase. [67, 68] Consequently, we would expect $c_{zz}^{(\pm)}(r) \sim 1/r^2$ in our model for sufficiently large g_r . Thus, we split the form of $g(r)$ as in the main text:

$$g(r) = \begin{cases} g_1, & r = 1, \\ g_r/r^2, & r \geq 2. \end{cases}$$

These two terms produce the competition seen in KT physics. g_1 controls the core energy or fugacity (how easy it is to nucleate kink pairs), while g_r/r^2 controls the long-distance stiffness (the strength of the logarithmic interaction between kinks).

The $\langle \sigma_i^+ \sigma_i^- \rangle$ correlations should correspond to defect/string correlators in the classical ising model, which should display algebraic correlations, so that $\mathcal{C}^{(\pm)}(r) \sim x^{-\eta_\pm}$. [69, 70] In the main text, we showed that $\eta_\pm \approx -4$. This is anomalously large for XY and XXZ -type models where the maximum power is typically $-\frac{1}{4}$ or -1 respectively. We expect this departure comes in part from the inter-replica structure of our model. Specifically, $\eta_\pm \propto m^2$ where the vorticity index is $m \geq 2$ because the minimum excitation of inter-replica modes requires the pairing of a vortex and anti-vortex in different replicas. [14]

Appendix I: Discrete G Example: \mathbb{Z}_2 Ensemble SSB

We now explore ensemble SSB phases for *discrete* physical symmetries. In the absence of diffusive local charges, the warped probability distribution at finite replica index n does not induce unphysical charge configurations in the ground state of the effective Hamiltonian. We therefore study a \mathbb{Z}_2 -symmetric system and analyze the exact ground-state structure (without variational ansätze). The model below also appears in Ref. [16]; see that work for circuit realizations of the phases discussed here.

We take $G = \mathbb{Z}_2$ on a spin-1/2 chain with generator

$$\Pi^z \equiv \prod_i \sigma_i^z, \quad (\text{I1})$$

and unitary interactions $h_i^{zz} = \sigma_i^z \sigma_{i+1}^z$ and $h_i^{xx} = \sigma_i^x \sigma_{i+1}^x$ acting on the n -th moment. We include “phase” (XX) measurements via

$$H_{\mathcal{M}_\phi} = -\Gamma_p \sum_i \sum_{m=\pm 1} (P_{i,m}^{XX})^{\otimes 2n}, \quad (\text{I2})$$

with projectors $P_{\pm 1}^{XX} = \frac{1}{2}(\mathbb{I} \pm \sigma_i^x \sigma_{i+1}^x)$. The ensemble symmetry is

$$[(\mathbb{Z}_2^{\otimes n} \rtimes \mathcal{S}_n)_L \times (\mathbb{Z}_2^{\otimes n} \rtimes \mathcal{S}_n)_R] \rtimes \mathbb{Z}_2^{\mathbb{H}}. \quad (\text{I3})$$

This symmetry has no true local charges, only global parity sectors. However, to keep the analogy with the definitions for continuous G , we define inter-replica and replica-average “parity charges,”

$$\bar{Q}_+^\Pi = \frac{1}{4}(\Pi_{1L}^z + \Pi_{1R}^z + \Pi_{2L}^z + \Pi_{2R}^z), \quad (\text{I4})$$

$$\bar{Q}_-^\Pi = \frac{1}{4}(\Pi_{1L}^z - \Pi_{1R}^z + \Pi_{2L}^z - \Pi_{2R}^z), \quad (\text{I5})$$

$$\tilde{Q}_+^\Pi = \frac{1}{4}(\Pi_{1L}^z + \Pi_{1R}^z - \Pi_{2L}^z - \Pi_{2R}^z), \quad (\text{I6})$$

$$\tilde{Q}_-^\Pi = \frac{1}{4}(\Pi_{1L}^z - \Pi_{1R}^z - \Pi_{2L}^z + \Pi_{2R}^z), \quad (\text{I7})$$

where we remove a constant offset for \bar{Q}_+^Π .

Reduced Basis - As in the U(1) example, we work in a reduced basis by taking infinitely strong local $h_i = \sigma_i^z$ rotations. This identifies all symmetric two-site unitaries with either $\sigma_i^z \sigma_{i+1}^z$ or $\sigma_i^x \sigma_{i+1}^x$ and prevents an independent parity-sharpening transition.

As in the main text, the rapid σ_i^z rotations also act as symmetric dephasing in the $\sigma_i^x \sigma_{i+1}^x$ basis and preclude full purification there. Heuristically, the identification of the parity sharpening and purification transition comes from an effective Kramers–Wannier duality on the dual lattice, $\sigma_i^x \sigma_{i+1}^x \leftrightarrow \tilde{\sigma}_i^z$ and $\tilde{\sigma}_i^x \tilde{\sigma}_{i+1}^x \leftrightarrow \tilde{\sigma}_i^z$, so that the single, parity coherent phase maps to a single, parity sharp phase in the replicated theory. Since purification can occur in the σ^z basis, this phase is necessarily Area-law, and the full phase diagram only admits three phases in agreement with Refs. [16, 34, 48].

In this reduced basis, the unitary contribution reads

$$\begin{aligned} H_{\mathcal{L}}^{(2)} &= \sum_x J_z (P_{1,x} P_{-1,x+1} + P_{-1,x} P_{1,x+1}) \otimes \mathbb{I} \\ &+ \sum_x \left[((S^x)^2 - (S^y)^2)_x ((S^x)^2 - (S^y)^2)_{x+1} \right. \\ &\quad \left. - S_x^x S_{x+1}^x - \{S^x, S^z\}_x \{S^x, S^z\}_{x+1} \right] \quad (\text{I8}) \\ &\otimes (\mathbb{I}_4 + \sigma_x^x \sigma_{x+1}^x), \end{aligned}$$

with J_z the relative strength of $\sigma_i^z \sigma_{i+1}^z$ interactions. The $\sigma_i^x \sigma_{i+1}^x$ -measurement term becomes

$$\begin{aligned} H_{\mathcal{M}_\phi} &= \sum_x \left[\mathbb{I}_9 + \frac{1}{2}((S^+)^2 + (S^-)^2)_x ((S^+)^2 + (S^-)^2)_{x+1} \right. \\ &\quad \left. + S_x^x S_{x+1}^x + \{S^x, S^z\}_x \{S^x, S^z\}_{x+1} \right] \quad (\text{I9}) \\ &\otimes (\mathbb{I}_4 + \sigma_x^x \sigma_{x+1}^x), \end{aligned}$$

and the σ_i^z -measurement term matches the U(1) case $H_{\mathcal{M}_Q} = \sum_x (S_x^z)^2$.

Since the spin-1/2 sector always orders ferro- or antiferromagnetically for these couplings, we restrict attention to the spin-1 sector, where

$$H_{\mathcal{L},ZZ} = \sum_x (P_{1,x} P_{-1,x+1} + P_{-1,x} P_{1,x+1}), \quad (\text{I10})$$

$$H_{\mathcal{M}_Q} = \sum_x (S_x^z)^2, \quad (\text{I11})$$

$$\begin{aligned} H_{\mathcal{L},XX} &= \sum_x \left[\frac{1}{2}((S^+)^2 + (S^-)^2)_x ((S^+)^2 + (S^-)^2)_{x+1} \right. \\ &\quad \left. - S_x^x S_{x+1}^x - \{S^x, S^z\}_x \{S^x, S^z\}_{x+1} \right], \quad (\text{I12}) \end{aligned}$$

$$\begin{aligned} H_{\mathcal{M}_\phi} &= \sum_x \left[\frac{1}{2}((S^+)^2 + (S^-)^2)_x ((S^+)^2 + (S^-)^2)_{x+1} \right. \\ &\quad \left. + S_x^x S_{x+1}^x + \{S^x, S^z\}_x \{S^x, S^z\}_{x+1} \right]. \quad (\text{I13}) \end{aligned}$$

After this reduction, the on-site ensemble symmetry is the dihedral group

$$D_4 = \mathbb{Z}_2^{\otimes 2} \rtimes \mathcal{S}_2, \quad (\text{I14})$$

with the nontrivial permutation acting on spin-1 as

$$\mathcal{S}_2 : |m, s\rangle \mapsto |-m, s\rangle. \quad (\text{I15})$$

It is convenient to work with two independent global parities (replica-average and inter-replica), following Ref. [16]:

$$\Pi_1^z = \prod_i (\sigma_{1L}^z \otimes \sigma_{1R}^z)_i \mapsto \prod_i (\mathbb{I} - 2P_{-1})_i, \quad (\text{I16})$$

$$\Pi_L^z = \prod_i (\sigma_{1L}^z \otimes \sigma_{2L}^z)_i \mapsto \prod_i (\mathbb{I} - 2(S^z)^2)_i. \quad (\text{I17})$$

These relate to the diagonal and inter-replica ensemble charges as

$$\Pi_1^z = 2(\mathbb{I} - (\bar{Q}_-^\Pi + \tilde{Q}_-^\Pi)^2), \quad (\text{I18})$$

$$\Pi_L^z = 2(\mathbb{I} - (\tilde{Q}_+^\Pi + \tilde{Q}_-^\Pi)^2). \quad (\text{I19})$$

Thus Π_L^z detects SSB of the inter-replica charges \tilde{Q}_\pm^Π , while Π_1^z probes SSB of the off-diagonal charges \bar{Q}_-^Π and \bar{Q}_+^Π .

We define the associated parity variance (a parity-sharpening diagnostic)

$$\begin{aligned} [\Delta \Pi^2] &= \mathbb{E}_{\mathbf{m}}^{(2)} [\text{Tr}[(\Pi^z)^2 \rho_{\mathbf{m}}(t)] - \text{Tr}[\Pi^z \rho_{\mathbf{m}}(t)]^2] \\ &= \frac{\langle \text{id} \|(\mathbb{I} - \Pi_L^z)\| \rho^{(2)}(t) \rangle}{\langle \text{id} \| \rho^{(2)}(t) \rangle}, \quad (\text{I20}) \end{aligned}$$

and the Rényi-2 SW-SSB correlator in this basis is

$$\mathcal{C}_{ij}^{(+)} = \frac{1}{4}(S_i^x + \{S_i^x, S_i^z\})(S_j^x + \{S_j^x, S_j^z\}). \quad (\text{I21})$$

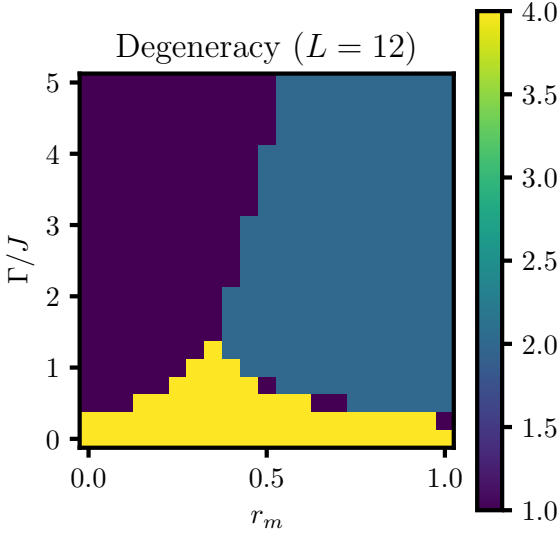


FIG. 13. **Ground-state degeneracy.** Three SSB regimes of the \mathbb{Z}_2 effective Hamiltonian as functions of Γ_p and r .

Similarly, we define the \mathbb{Z}_2 parity coherence

$$\begin{aligned} [\Delta\Phi_Q^2] &= \mathbb{E}_{\mathbf{m}}^{(2)} \left[\frac{\text{Tr}[(\Pi^z)^2 \rho_{\mathbf{m}}^2(t)] - \text{Tr}[\rho_{\mathbf{m}}(t)\Pi^z \rho_{\mathbf{m}}(t)\Pi^z]}{\text{Tr}[\rho_{\mathbf{m}}^2(t)]} \right] \\ &= \frac{\langle\langle \text{SW} | \Pi_1^z | \rho^{(2)}(t) \rangle\rangle}{\langle\langle \text{SW} | \rho^{(2)}(t) \rangle\rangle}, \end{aligned} \quad (\text{I22})$$

and the glassy SSB correlator is

$$\mathcal{C}_{ij}^{(-)} = \frac{1}{4} ((S_i^+)^2 + (S_i^-)^2)((S_j^+)^2 + (S_j^-)^2). \quad (\text{I23})$$

Low-Energy Structure - Diagonalizing the effective Hamiltonian in this reduced basis reveals three phases (Fig. 13):

- *Area-law, parity-sharp.* All parity excitations are gapped. A representative product ground state is

$$\langle\langle \rho_{\infty} \rangle\rangle \sim \bigotimes_i |0\rangle_i. \quad (\text{I24})$$

- *Volume-law, parity-fuzzy.* There is an exponentially small splitting between sectors related by \mathcal{T}^r and Π_L^z , exchanging $(|0\rangle \pm |\pm 1\rangle)$. A representative superposition is

$$\begin{aligned} \langle\langle \rho_{\infty} \rangle\rangle &\sim \bigotimes_i (|0\rangle_i + |1\rangle_i) + \bigotimes_i (|0\rangle_i - |1\rangle_i) \\ &+ \bigotimes_i (|0\rangle_i + |-1\rangle_i) + \bigotimes_i (|0\rangle_i - |-1\rangle_i). \end{aligned} \quad (\text{I25})$$

The associated tower-of-states splittings are $\delta_0 \sim \delta_{\Pi_L} \sim e^{-L}$. As in the main text, we must be careful about an apparent Π_1 splitting. If we only considered the $| - 1 \rangle$ configurations, there would be

a splitting between $\Pi_1 = \pm 1$ sectors. However, such states are no longer eigenstates of Q_{σ} . Instead, recall that decoherence would break \mathcal{S}_2 , and eliminate all terms with $| - 1 \rangle$ contributions, so that this phase has no robust Π_1 order.

- *Volume-law, parity-coherent.* There is a simultaneous exponential splitting among \mathcal{T}^r , Π_L^z , and Π_1^z sectors. A representative pair of nearly degenerate states is

$$\langle\langle \rho_{\infty}^{(\pm)} \rangle\rangle \sim \bigotimes_i (|1\rangle_i \pm (-1)^i | - 1 \rangle_i). \quad (\text{I26})$$

Because the reduced basis includes infinitely rapid z rotations, trajectories do not fully purify in the x basis: the ground-state subspace contains two states distinguished by Π_1^z and does not exhibit long-range order in $\mathcal{C}_{ij}^{(+)}$, though we expect this order to return if the spin- $\frac{1}{2}$ space is restored.

We diagnose these phases by the symmetry quantum numbers of the degenerate ground states as Γ_p and r are varied; see Fig. 14.

Although the reduced basis obscures some details, the charge-coherent phase is necessarily parity-fuzzy (even if the underlying entanglement is area-law). The three phases match those seen in \mathbb{Z}_2 -symmetric circuits with the same geometry [16, 34, 48]. Here, it was seen that, in the absence of decoherence, the parity-coherent phase appears only in the area-law regime; introducing infinitely rapid unitary z rotations (which act as symmetric decoherence) pushes the parity-coherent phase into the volume-law regime and suppresses the parity variance.

Appendix J: U(1) Ansatz Data

Further data for the charge and (SW)SSB correlators and TOS gaps for different phases described by our ansatz wavefunction are presented below in Fig. 15 and Fig. 16.

As noted above, and shown in Fig. 16, η_{\pm} are significantly larger than the expected maximum value of 1/4 or 1 for models with KT physics such as the XXZ or XX models; however, we expect this is due, in part, to the minimum vorticity, q , being doubled for interreplica modes, decreasing the critical stiffness parameter as K_0/q^2 . An additional source of bias likely comes from our choice of ansatz, which captures the physics of a different model, a quasi-long range classical Ising model.

We note that in Fig. 16 and Fig. 9, correlators are numerically calculated with expectation values, (i.e. $\langle\langle [\mathcal{C}^{(-)}]_{\text{id}}(x) \rangle\rangle$). Relative to that, the SW-SSB correlators defined in the main text, $[\mathcal{C}^{(-)}]_{\text{id}}(x)$ and \tilde{Q}_{-} correlator, $[c_{zz}^{(-)}]_{\text{sw}}(x)$ differ by the use of a boundary term, $\langle\langle \text{SW} |$ in the matrix element, which should not affect the power laws seen; however, the correlators in the main text also need to be normalized by a matrix element,

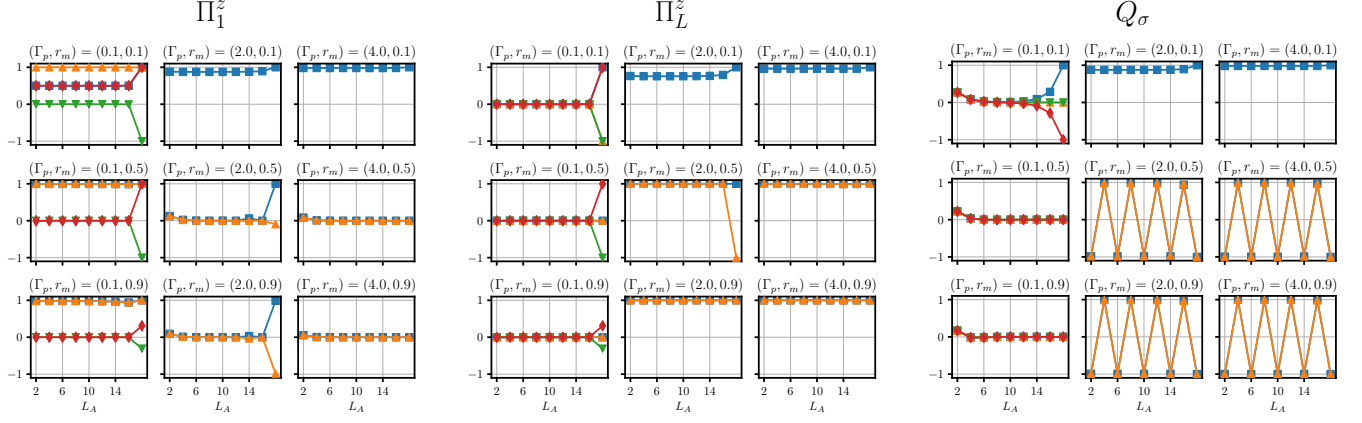


FIG. 14. \mathbb{Z}_2 subsystem indicators. - Plots of the \mathbb{Z}_2 parities and \mathcal{S}_2 sectors for nearly degenerate ground states of the effective Hamiltonian as a function of Γ_p and r . Note that the exact eigenstates should have parities of ± 1 , but mixing of exact eigenstates can produce 0 values. (Left) replica-average parity Π_1^z - Splitting between $\Pi_1^z = \pm 1$ for large Γ_p and r . Although there appears to be splitting for low Γ_p , this vanishes with infinitesimal decoherence (See Eq. (16)), just like the charge coherence in the fuzzy phase for continuous G , (Center) inter-replica parity Π_L^z - Splitting between $\Pi_L^z = \pm 1$ for small Γ_p ; (Right) permutation charge Q_σ - Splitting between $Q_\sigma = \pm 1$ for small Γ_p and for large Γ_p and r .

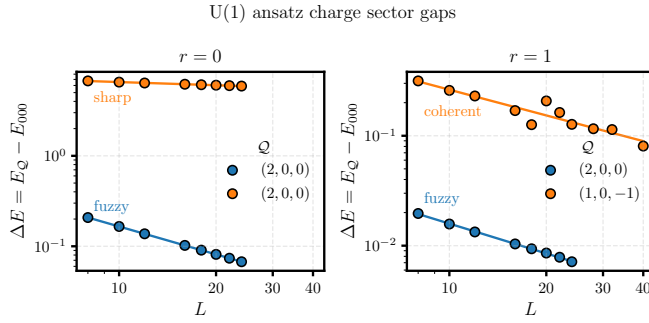


FIG. 15. $U(1)$ charge-sector gaps. The inter-sector charge gap extracted from the ansatz of Sec. V. The energy E_Q is evaluated with respect to the Gutzwiller-Jastrow ansatz projected onto the $\mathcal{Q} = (\tilde{Q}_+, \overline{Q}_+, \tilde{Q}_-)$ sector. Values of \mathcal{Q} were chosen based on their proximity to the $(0, 0, 0)$ sector—which contains the ground state—and the condition that $|\mathcal{Q}| = \tilde{Q}_+ + \overline{Q}_+ + \tilde{Q}_-$ is even for L even. (Right) Charge measurement and random unitary inter-sector charge gap exhibits $\Delta E \propto L^{-\gamma}$ scaling in the fuzzy phase and appears to remain gapped within the charge sharp phase. For the fuzzy phase, a linear fit found $\gamma = 1.025(6)$. (Left) Inter-sector charge gap with phase-measurements and random unitary dynamics. We find similar behavior for both the fuzzy and coherent phases with $\gamma = 0.90(9)$ and $0.8(1)$ respectively. For both $r = 0$ and 1, fuzzy data was taken from the optimized values of α, β, g_1 , and g_r at $\Gamma_p = 0.6$ and at $\Gamma_p = 4.8$ for the sharp and coherent phases.

$\langle\langle SW \|\rho^{(2)}\rangle\rangle$ that is exponentially small but constant in the fuzzy phase, and that increases with Γ_p in the coherent phase. We expect this to account for the seeming rise in η_+ and p_- near the coherent phase in Fig. 16 when this normalization is not included.

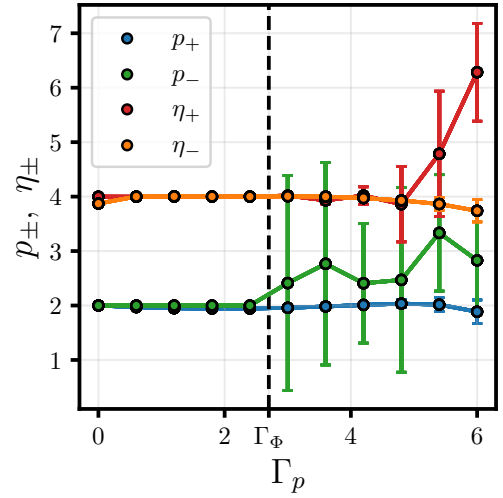


FIG. 16. Power-law exponents for phase measurements ($r = 1$) - Power law exponents for $\langle\langle c_{zz}^{(\pm)}(x)\rangle\rangle \sim x^{-p_\pm}$ and $\langle\langle \mathcal{C}^{(\pm)}(x)\rangle\rangle \sim x^{-\eta_\pm}$ as a function of the measurement strength, Γ_p . The transition into the charge coherent phase occurs near $\Gamma_p \approx 2.7$, where the error in extracting p_- becomes large.

Appendix K: Explicit Phase Measurements

To begin, we construct an explicit “phase state” on a bond of a spin- S chain with a fixed total $S_{\text{tot}}^z = Q$. To do so, we shift from a basis of local charges on both sites $|m_1, m_2\rangle$ to one of total charge, Q , and charge difference, $m \equiv (m_1 - m_2)/2$, $|Q, m\rangle$, so that $m_1 = \frac{Q}{2} + m$ and $m_2 = \frac{Q}{2} - m$. This allows us to define a discrete fourier

transform within a total charge sector:

$$|\phi, Q\rangle = \frac{1}{\sqrt{d_Q}} \sum_{m=-l_Q}^{l_Q} e^{im\phi} |Q, m\rangle, \quad (\text{K1})$$

where we have defined a degeneracy, $d_Q = \sqrt{2S + 1 - M}$, a maximum difference $l_Q = 2S - |Q|$. We can now define the projectors on these states:

$$P_Q(\phi) = \frac{1}{d_Q} \sum_{m,m'=-l_Q}^{l_Q} e^{i(m-m')\phi} |Q, m\rangle \langle Q, m'| \quad (\text{K2})$$

To make measurement operators for the phase, we sum over all charge sectors, weighted by d_Q :

$$P(\phi) = \sum_Q \sqrt{d_Q} P_Q(\phi). \quad (\text{K3})$$

Since these are constructed from projectors to phase configurations, these are positive-semidefinite measures. Further, we can check that they constitute a good probability measure since they produce a resolution of identity:

$$\begin{aligned} \int \frac{d\phi}{2\pi} P(\phi)^2 &= \sum_Q d_Q \int \frac{d\phi}{2\pi} P_Q(\phi) \\ &= \sum_Q \sum_{m=-l_Q}^{l_Q} |Q, m\rangle \langle Q, m| = \mathbb{I}. \end{aligned} \quad (\text{K4})$$

Note that different phases are not strictly orthogonal in this basis, so that $\langle \phi, Q | \phi', Q' \rangle \neq \delta_{\phi,\phi'} \delta_{Q,Q'}$. However, in the large- S limit ($Q, S \rightarrow \infty$), this equality is satisfied, and we approximately recover projectors to orthogonal phase states. Although we have defined the POVM for continuous ϕ , one can easily redefine these measures for a discrete set of N_ϕ different ϕ_n by adjusting normalizations and replacing the integral above with a discrete sum: $\int \frac{d\phi}{2\pi} \rightarrow \sum_{\phi_n} \Delta\phi$.

Appendix L: Measurement-Only Circuit Data

Here, we present additional data supporting the presence of the charge coherent phase for the phase measurement only circuit described in the main text.

We expect the profile of the steady state to resemble that of the 1D Quantum XY model, that is, a Luttinger Liquid (LL), with log-sine profile

$$S_{ss}[x, t; L] = \frac{c}{6} \ln \left[\frac{2L}{\pi a} \sin \left(\frac{\pi x}{L} \right) f(x, t; L) \right] + s_b \quad (\text{L1})$$

where a is a UV cutoff (lattice scale) and s_b is a nonuniversal additive constant that may include boundary contributions. For the LL/XY universality class, $c = 1$.

As explained in the main text, we expect our state to share the same log-sine profile; however, because our

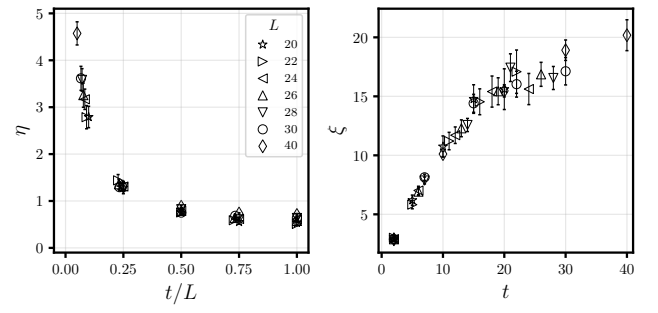


FIG. 17. Scaling exponent and correlation length: Power-law exponent and correlation lengths for Edwards-Anderson correlation functions presented in Fig. 10 of the main text. (Left) Exponent η assuming $[\mathcal{C}_-(x)]_{\text{sw}} \propto x^{-\eta}$ extracted from a linear fit to data for various L and times $\tau = t/L$. We see good agreement among different system sizes at the same fractional time, suggesting convergence to critical behavior at times extensive in the system size. (Right) Correlation length for the same data extracted by a linear fit to the data assuming $[\mathcal{C}_-(x)]_{\text{sw}} \propto e^{-x/\xi}$. Note that the horizontal axis is the time in units of circuit depth, not scaled by system size. Here we see approximately linear behavior at short times with a tapering off and increase in fit-error as t becomes of $O(L)$.

purity is calculated as a boundary insertion rather than with the bulk twist operators used for standard CFT's, the coefficient of the logarithm may not match the central charge of any underlying CFT. Specifically, we expect both (i) the steady state entanglement profile and (ii) real-space correlators should admit robust conformal scaling forms with a growing length scale, $\xi(t) \sim vt$, where v is the LL velocity.

Here, we choose a product initial state to be in a Néel configuration with odd sites in $|z = +\frac{1}{2}\rangle$, and even sites $|z = -\frac{1}{2}\rangle$. In practice, the Néel state is not an exact conformal boundary state, so an extrapolation time t_0 is introduced to absorb UV/boundary-state mismatch, and we introduce the dimensionless parameter:

$$u(t) = \frac{2\pi(t + t_0)}{L}, \quad (\text{L2})$$

which compares the projection depth $v(t + t_0)$ to the system size L .

We rely on an estimated compact interpolating fit form that (i) reduces to the steady state profile as $t \rightarrow \infty$ and (ii) depends on time only through $u(t)$:

$$S(x, t; L) = S_{ss}[x, t; L] + \frac{c}{6} \log \left[\frac{\sinh u(t)}{\cosh u(t) - \cos(2\pi x/L)} \right] \quad (\text{L3})$$

for $u = O(1)$, the second log is nontrivial and encodes the dependence on t/L . Because of the first term, $S_{ss}[x, t; L]$, the profile will show an approximate collapse when plotting $S / \log L$ for different intermediate values of L .

Hopping Measurements - In addition, we present data for a circuit of hopping measurements in place of phase measurements. Starting from the same initial Néel state, the system is evolved with measurements of the hopping operator, $h_{ij} = \sigma_i^+ \sigma_j^- + \sigma_i^- \sigma_j^+$, on every odd(even) bond at every odd(even) timestep with probability p . Similar to the main text, we investigate the steady-state entanglement entropy profile and EA correlation function, $[\mathcal{C}^{(-)}(x)]_{\text{sw}} \sim \mathbb{E}_{\mathbf{m}}[|\langle \sigma_0^+ \sigma_x^- \rangle_{\mathbf{m}}|^2]$. In Fig. 18 below, we show data taken at times, $T = L = 20$.

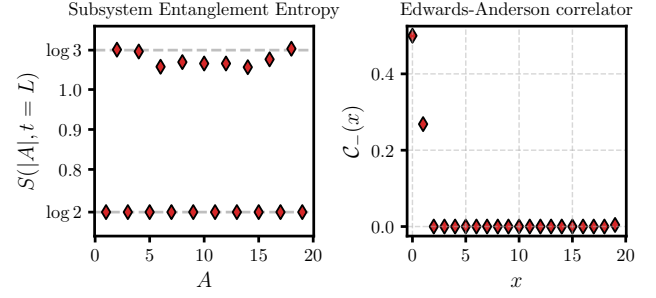


FIG. 18. **Projective hopping measurements data** - Entanglement entropy profile and Edwards-Anderson correlation function evaluated at $t = L = 20$ for a hopping measurement only circuit. (*Left*) Entanglement entropy profile showing an Area-law, alternating structure. (*Right*) Edwards-Anderson correlator, $[\mathcal{C}^{(-)}(x)]_{\text{sw}} \sim \mathbb{E}_{\mathbf{m}}[|\langle S_0^+ S_x^- \rangle_{\mathbf{m}}|^2]$ demonstrates only nearest-neighbor correlations with $[\mathcal{C}^{(-)}(x)]_{\text{sw}} = 0$ for $x > 1$.